Measurement of the Fluorine, Sodium, and Aluminum Fluxes in Cosmic Rays with the AMS Experiment on the International Space Station

by

Xiaoting Qin

B.S., Shandong University (2014)

Submitted to the Department of Physics
in partial fulfillment of the requirements for the degree of

Doctor of Philosophy

at the

MASSACHUSETTS INSTITUTE OF TECHNOLOGY

February 2022

Author .....
Department of Physics
January 8, 2022

Certified by .....
Samuel C.C. Ting
Thomas Dudley Cabot Professor of Physics
Thesis Supervisor

Accepted by .....
Deepto Chakrabarty
Associate Department Head, Department of Physics

Measurement of the Fluorine, Sodium, and Aluminum Fluxes in Cosmic Rays with the AMS Experiment on the International Space Station

by

Xiaoting Qin

Submitted to the Department of Physics
on January 8, 2022, in partial fulfillment of the
requirements for the degree of
Doctor of Philosophy

Abstract

Primary nuclei (He, C, O, Ne, Mg, Si, ...) are thought to be mainly produced and accelerated in astrophysical sources such as the supernova. Secondary nuclei (Li, Be, B, ...) are mostly produced by interactions of primary nuclei with the interstellar medium. Precise knowledge of the secondary-to-primary flux ratio, like B/C, is essential in the understanding of cosmic ray propagation. This thesis presents the first precision measurements of the heavy cosmic ray fluorine (F), sodium (Na), and aluminum (Al) fluxes in the rigidity range from 2.15 GV to 3.0 TV, based on data collected by the Alpha Magnetic Spectrometer (AMS) during the first 8.5 years of operation. The F flux is believed to be the only pure secondary flux between oxygen and silicon, and Na and Al fluxes are thought to be produced both in astrophysical sources and by the collisions of heavier nuclei with the interstellar medium.

The measurements show that the F flux deviates from a single power law above 200 GV. The heavier secondary-to-primary F/Si flux ratio rigidity dependence is distinctly different from the lighter B/O (or B/C) rigidity dependence. In particular, above 10 GV, the [(F/Si)/(B/O)] ratio can be described by a power law R^{δ} with $\delta = 0.052 \pm 0.007$. This shows that the propagation properties of heavy cosmic rays, from F to Si, are different from those of light cosmic rays, from He to O, and that the secondary cosmic rays have two classes. The Na and Al fluxes are well described by the sums of a primary cosmic ray component (proportional to the Si flux) and a secondary cosmic ray component (proportional to the F flux), similar to the nitrogen (N) flux. The fraction of the primary component increases with rigidity for the N, Na, and Al fluxes and becomes dominant at the highest rigidities. The Na/Si and Al/Si abundance ratios at the source, 0.036 ± 0.003 for Na/Si and 0.103 ± 0.004 for Al/Si, are determined independent of cosmic ray propagation.

Thesis Supervisor: Samuel C.C. Ting
Title: Thomas Dudley Cabot Professor of Physics

Acknowledgments

I would like to take this opportunity to express my sincere gratitude to everyone who has helped me greatly through this journey.

First of all, I would like to thank my supervisor Professor Samuel Ting, from whom I have learned so much, not only physics knowledge, but also the rigorous attitude towards science.

I want to thank in particular, Dr. Vitaly Choutko, Dr. Qi Yan, Dr. Mike Capell, and Dr. Tatiana Medvedeva, for their discussions and advices in preparing this thesis.

I would also like to thank Professor Jacqueline Hewitt for constructive suggestions on this thesis.

In addition, my gratitude goes to all the collaborators of AMS-02. I am very fortunate to work in such a great collaboration. I have learned many things in research and analysis from Dr. Valerio Formato, Professor Bruna Bertucci, Dr. Alberto Oliva, and Dr. Matteo Duranti. And I have received great support from Dr. Xudong Cai, Mr. Andrey Rozhkov, Dr. Joseph Burger, and Dr. Giovanni Ambrosi for taking shifts in POCC. I would also like to thank Ms. Laurence Barrin, Ms. Tsai-Hsiu Hsieh, Professor Paolo Zuccon, Ms. Christine Titus, Dr. Susan Ting, and Ms. Naomi Benchaya for their kind support both at MIT and CERN. And I thank my colleagues and friends at CERN: Professor Baosong Shan, Dr. Zhang Zhan, Dr. Zhili Weng, Professor Weiwei Xu, Dr. Zhaoyi Qu, Dr. Senquan Lu, Dr. Hu Liu, and Dr. Youmin Yu.

I would like to thank my academic advisor Professor Janet Conrad for helping me with course selections, and thank Ms. Cathrine Modica and Ms. Sydney Miller from the academic office for their support.

I am fortunate to have many friends by my side during my Ph.D. study. I will not forget the time at MIT with Yiwen Huang, Jianhao Fu, Tongtong Liu, Jeff Krupa, and many other friends. And I would like to thank Dr. Yi Jia, Dr. Huy Phan, Dr. Matthew Behlmann, Dr. Yunjie Yang, and many others in the Laboratory for Nuclear Science for their help with my preparation for the oral exam. And I thank my good friend

Rongchen Dong.

Finally, I can never be grateful enough for the unconditional love and support from my family. To my parents, Shijun Cui and Liandong Qin, thank you for always being my biggest supporters and my sanctuary. And to my brother, Chuan Qin, thanks for always looking after me.

Contents

1 Introduction **23**

1.1 Cosmic Rays . . . 24

1.1.1 Energy Spectrum . . . 24

1.1.2 Chemical Composition . . . 27

1.1.3 Sources and Acceleration of Cosmic Rays . . . 28

1.1.4 Cosmic-ray Propagation . . . 29

1.1.4.1 The Slab Model . . . 30

1.1.4.2 The Leaky-box Model . . . 30

1.1.4.3 Diffusion Theory . . . 31

1.1.5 Cosmic-ray Measurements . . . 33

1.1.5.1 Ground-based experiments . . . 33

1.1.5.2 Balloon-borne experiments . . . 35

1.1.5.3 Space-borne experiments . . . 36

1.2 Previous Measurements on Fluorine, Sodium, and Aluminum Cosmic Rays . . . 37

1.3 Motivation for Measuring Fluorine, Sodium, and Aluminum Cosmic Rays . . . 41

2 The Alpha Magnetic Spectrometer **43**

2.1 AMS Detector . . . 43

2.1.1 Permanent Magnet . . . 45

2.1.2 Transition Radiation Detector (TRD) . . . 47

2.1.3 Time of Flight (TOF) . . . 51

2.1.4 Silicon Tracker . . . 54
2.1.5 Anti-Coincidence Counter(ACC) . . . 59
2.1.6 Ring Imaging Cherenkov Detector (RICH) . . . 60
2.1.7 Electromagnetic Calorimeter (ECAL) . . . 64
2.2 Trigger and Monte Carlo Simulation . . . 66

3 Measurements of the Fluorine, Sodium, and Aluminum Fluxes 69
3.1 Exposure time . . . 70
3.2 Event Selection . . . 71
3.3 Effective Acceptance . . . 74
3.3.1 Corrections to the Effective Acceptance . . . 74
3.3.1.1 Velocity Vector Determination Efficiency . . . 74
3.3.1.2 Track Finding Efficiency . . . 75
3.3.1.3 Charge Determination Efficiency . . . 79
3.3.2 Total Correction . . . 80
3.4 Nuclear Interaction Cross Section . . . 81
3.4.1 Nuclear Survival Probabilities . . . 82
3.4.2 Nuclear Interaction Cross Sections on Carbon Target . . . 90
3.5 Background Estimation . . . 92
3.6 Trigger Efficiency . . . 100
3.7 Tracker Resolution Function and Unfolding of the Flux . . . 102
3.7.1 Tracker Resolution Function . . . 106
3.7.2 Forward Unfolding Method . . . 109
3.8 Systematic Error . . . 111
3.8.1 Geomagnetic Cutoff . . . 111
3.8.2 Absolute Rigidity Scale . . . 111
3.9 Total Error . . . 112

4 Results 115
4.1 The Fluorine Flux and the Fluorine to Silicon Ratio . . . 115
4.2 The Sodium and Aluminum Fluxes . . . 125

5 Conclusion **137**

List of Figures

1-1 Overview of energy spectra of cosmic rays before AMS. The red cross markers below 10^{11} eV represent the measured spectrum of protons. All other data represent all-particle cosmic ray energy spectrum. Figure is from Ref. [1]. 26

1-2 Comparison of the elemental abundances in cosmic rays (solid dots) and in the solar system (open symbols), all relative to carbon = 100. Figure is from Ref. [10]. 27

1-3 Energy spectrum of high-energy cosmic rays obtained from various ground-based measurements [26–31, 35, 36]. Figure is from Ref. [37]. . 35

1-4 Previous measurements of fluorine fluxes. 38

1-5 Previous measurements of sodium fluxes. 39

1-6 Previous measurements of aluminum fluxes. 40

2-1 Schematic view of the AMS. The sub-detectors are labelled. 44

2-2 AMS permanent magnet. 45

2-3 Magnetic field orientation of the AMS Permanent Magnet. 46

2-4 The AMS magnetic field intensity over the Z axis measured in 1997 and 2010. Z = 0 corresponds to the magnet center. 47

2-5 The TR X-rays produced by electrons in the fleece are efficiently absorbed in the straw tubes, producing a signal significantly larger than that from the ionization of protons. 48

2-6 The Transition Radiation Detector. 49

2-7 One of the 328 TRD modules. 49

2-8 The TRD proton rejection power, defined as the number of protons which are rejected before a proton is misidentified as an electron or positron, as a function of rigidity at 90% selection efficiency for $e^{\pm}$. At 1 TV, the proton rejection factors at 70%, 80%, and 90% $e^{\pm}$ efficiency are indicated by the arrows. 50

2-9 TRD Gas schematic (not to scale). Figure is from Ref. [68]. 51

2-10 (a) The upper TOF plane. (b) The lower TOF plane. Figure is from Ref. [60]. 52

2-11 The design of a TOF counter. Figure is from Ref. [69]. 53

2-12 For the TOF, anode (dots, dashed line) and dynode (squares, solid line) charge resolution in charge units (c.u.) as a function of Z; the error bars represent the standard deviation of the distribution of resolution for all TOF counters. Figure is from Ref. [69]. 54

2-13 Schematic view of the AMS silicon tracker with a charged particle traversing the detector, presented in the bending (Y-Z) plane of the magnetic field. Figure is from Ref. [72]. 55

2-14 (a) Charge resolution ΔZ and (b) $\Delta Z/Z$ of the inner tracker (circles) and a single layer (squares) as functions of nuclei charge Z with $R >$ 7 GV. Figure is from Ref. [77]. 58

2-15 Illustration of the ACC working principle for particles with $Z > 1$. Left: A particle entering the detector sideways may give a signal on ACC and not in TOF. These kinds of events are rejected. Center: when a high-Z particle traverses matter, it is accompanied by electron production. These electrons can easily fire the ACC. In order to keep these events, the ACC veto is disabled. Right: when an electron or positron passes through the ECAL, backsplash particles are produced. These particles may exit from the calorimeter surface and hit the ACC. In this case, the trigger condition should be TOF and not more than 4 ACC paddles fired. Figure is from Ref. [78]. 59

2-16 AMS ACC mounted inside the magnet. 60

2-17 Schematic of the RICH. It is composed by three parts: the radiator layer, the expansion volume with conical reflector, and the photon-detection plane. 62

2-18 RICH velocity resolution as a function of charge Z for the aerogel radiator. Figure is from Ref. [60]. 63

2-19 RICH charge resolution as a function of charge Z for the aerogel radiator. Figure is from Ref. [60]. 64

2-20 A photo of the completed ECAL before installation in AMS. 65

2-21 Comparison of the measured proton rejection for 90% (blue data points) and 65% (red data points) $e^{\pm}$ selection efficiencies. The tighter cut further reduces the proton background by a factor of ~ 3. This is independent of the rejection power of the TRD shown in Figure 2-8. Figure is from Ref. [60]. 66

3-1 The AMS exposure time as a function of rigidity using data from the beginning of operation in May 2011 until Oct 2019. 71

3-2 Schematic of the AMS detector. The solid blue line is the reconstructed track using the TOF and TRD clusters. The dashed green line indicates the TOF and TRD track extrapolation. 76

3-3 The inner track reconstruction efficiency for sodium data (filled dots) and MC simulation (open circles) as a function of estimated rigidity. The bottom panel shows the ratio of the efficiency in data to simulation, along with the spline fit to the ratio (curve) and the 68% CL interval (band). The fit above 20 GV is obtained from constant extrapolation. 78

3-4 Charge distribution measured by the inner tracker for nuclei from Z=9 to Z=16 selected by charge measured with L1, the upper TOF, and the lower TOF. The vertical dashed lines indicate the charge selection for fluorine (cyan), sodium (red), and aluminum (magenta). 79

3-5 The inner tracker charge determination efficiency for sodium data (filled dots) and MC simulation (open circles) as a function of rigidity. The bottom panel shows the ratio of the efficiency in data to simulation, along with the spline fit to the ratio (curve) and the 68% CL interval (band not visible). 80

3-6 The sodium nuclei total data to MC correction factor (red curve) as a function of rigidity. The red band represents the systematic uncertainty of the correction factor at 68% CL. 81

3-7 (a) Schematic of AMS flying horizontally. (b) Illustration of the L2 to L1 nuclei survival probability measurement in the AMS materials of upper TOF and TRD. (c) Illustration of the L8 to L9 nuclei survival probability measurement in the AMS materials of lower TOF and RICH. Note, that both in (b) and (c) we use L2–L8, located inside the magnet and marked "Define beam" in the figures, to identify particles and to measure their rigidities. Figure is from Ref. [60]. 83

3-8 The He interaction cross section on carbon target (σ_{He+C}) as a function of rigidity measured by AMS (solid curve) in the rigidity range from 2 GV to 1 TV, together with earlier measurements (open circle [93], open squares [94] and open triangles [95]) and the GEANT4 Glauber-Gribov model [83,89] (dashed curve). The grey band indicates the systematic error (68% CL) of the AMS result. Figure is from Ref. [84]. 84

3-9 The inner tracker charge distribution for data (points) and MC (histogram) events selected with L1 charge Z = 12 (Mg) in the rigidity range from 20 to 21 GV. Both distributions have been normalized to their total number of events for comparison. Figure is from Ref. [84]. 86

3-10 The estimated relative contamination from Ne ($f^{Z=12}_{Z'=10}$, open circles), Na ($f^{Z=12}_{Z'=11}$, open squares), Al ($f^{Z=12}_{Z'=13}$, solid squares), and Si ($f^{Z=12}_{Z'=14}$, solid circles) as functions of rigidity for a sample selected by charge Z = 12 (Mg) measured on L1. The contamination from $Z' < 10$ and $Z' >$ 14 is negligible. Figure is from Ref. [84]. 87

3-11 The nuclear break-up probabilities between L1 and L2 for the channels Mg to Na ($P_{Z'=11}^{Z=12}$) and Mg to F ($P_{Z'=9}^{Z=12}$) as functions of rigidity for data (solid circles and solid squares) and MC (open circles and open squares). Figure is from Ref. [84]. 88

3-12 The MC/Data ratio of survival probabilities between L1 and L2 for Mg nuclei. The solid line shows the constant fit to the ratio and the dashed lines indicate the systematic error range (68% CL). Figure is from Ref. [84]. 89

3-13 The square root of the interaction cross section on carbon target at rigidity 15 GV ($\sqrt{\sigma_{N+C}^{15GV}}$) as a function of projectile charge radius (r_c^p) [97]. The line shows the fit with Eq. (3.9). The isotopic compositions used are ^{4}He (He), 30%^{10}B+70%^{11}B (B), ^{12}C (C), 50%^{14}N+50%^{15}N (N), ^{16}O (O), ^{20}Ne (Ne), ^{24}Mg (Mg), ^{28}Si (Si), ^{32}S (S) and ^{56}Fe (Fe). As seen, the linear function describes the data well. Accordingly, the light blue markers show the extrapolation of the nuclear interaction cross sections on carbon target for ^{19}F, ^{23}Na, and ^{27}Al. Figure is updated from [84, 98]. 91

3-14 Charge distributions measured by tracker L1 for fluorine events selected by the inner tracker L2-L8 in the rigidity range between 18 and 22 GV (black dots). The solid red curve shows the fit to the data of the sum of the O, F, Ne, and Na charge distribution templates. The templates are obtained from non-interacting samples at L2 by using combined L1, upper TOF, L3-L8, and lower TOF charge selections. The charge selection for F applied on tracker L1 is shown as vertical dashed lines. 93

3-15 Charge distributions measured by tracker L1 for sodium events selected by the inner tracker L2-L8 in the rigidity range between 18 and 22 GV (black dots). The solid red curve shows the fit to the data of the sum of the Ne, Na, Mg, and Al charge distribution templates. The templates are obtained from non-interacting samples at L2 by using combined L1, upper TOF, L3-L8, and lower TOF charge selections. The charge selection for Na applied on tracker L1 is shown as vertical dashed lines. 94

3-16 Charge distributions measured by tracker L1 for aluminum events selected by the inner tracker L2-L8 in the rigidity range between 18 and 22 GV (black dots). The solid red curve shows the fit to the data of the sum of the Mg, Al, Si, P, and S charge distribution templates. The templates are obtained from non-interacting samples at L2 by using combined L1, upper TOF, L3-L8, and lower TOF charge selections. The charge selection for Al applied on tracker L1 is shown as vertical dashed lines. 95

3-17 Comparison of the simulated (MC) and measured (Data) Ne, Mg, Si $\rightarrow$F break-up probabilities between L1 and L2. 96

3-18 F background from heavier nuclei interactions above L1 together with its uncertainty at 68% CL (blue shaded area) as a function of rigidity. The amount of background as a function of rigidity is determined by nuclei interaction cross sections, by the relative abundance of heavier nuclei to F and by L1, upper TOF and lower TOF charge selection criteria, which were chosen to minimize the background uncertainty. . 97

3-19 Na background from heavier nuclei interactions above L1 together with its uncertainty at 68% CL (blue shaded area) as a function of rigidity. The amount of background as a function of rigidity is determined by nuclei interaction cross sections, by the relative abundance of heavier nuclei to Na and by L1, upper TOF and lower TOF charge selection criteria, which were chosen to minimize the background uncertainty. . 98

3-20 Al background from heavier nuclei interactions above L1 together with its uncertainty at 68% CL (blue shaded area) as a function of rigidity. The amount of background as a function of rigidity is determined by nuclei interaction cross sections, by the relative abundance of heavier nuclei to Al and by L1, upper TOF and lower TOF charge selection criteria, which were chosen to minimize the background uncertainty. . 99

3-21 The trigger efficiency as a function of charge at 20 GV (left) and 40 GV (right). The blue points are the measured trigger efficiencies of oxygen, neon, magnesium, and silicon. The red points are the trigger efficiencies of fluorine, sodium, and aluminum, obtained by the interpolation of the neighbouring nuclei. Black lines are the linear fits of the blue points. 101

3-22 The trigger efficiency of sodium as a function of rigidity, evaluated by the interpolation of measured trigger efficiencies of neon and magnesium. 102

3-23 Carbon nuclei ionization energy loss in a single tracker layer as a function of $\beta\gamma$. The open black circles correspond to the peak values resulting from fits to the energy deposition in each slice of $\beta\gamma$. The peak profile is then fitted to obtain the final parameterization (blue curve) of the energy dependence. Figure is from Ref. [99]. 104

3-24 The differences Δy of the bending plane y coordinates measured in L3 or L5 to those obtained from the track fit using the measurements from L1, L2, L4, L6, L7, L8, and L9 for data and simulation for fluorine, sodium and aluminum. The measured bending coordinate accuracy is 8 μm for fluorine, 6 μm for sodium, and 7 μm for aluminum. 105

3-25 Examples of rigidity resolution parameterizations, using sodium sample in different rigidity ranges for the tracker L1- L8 configuration. 107

3-26 The AMS rigidity resolution smearing matrices for the tracker a) L1-L8 and b) L1-L9 configurations. 108

3-27 The rigidity dependence of the unfolding factor for fluorine (red), sodium (green), and aluminum (blue). 110

3-28 Total flux error as a function of rigidity for fluorine flux measurement, along with the breakdown of its components. All the constituent uncertainties are added in quadrature to arrive at the total error. . . . 112

3-29 Total flux error as a function of rigidity for sodium flux measurement, along with the breakdown of its components. All the constituent uncertainties are added in quadrature to arrive at the total error. . . . 113

3-30 Total flux error as a function of rigidity for aluminum flux measurement, along with the breakdown of its components. All the constituent uncertainties are added in quadrature to arrive at the total error. . . 114

4-1 The AMS F flux multiplied by $\tilde{R}^{2.7}$ with total errors as a function of rigidity (red points and left axis) together with the AMS B flux [60] (blue points and right axis). 116

4-2 The AMS F spectral index (red points) together with the B spectral index (blue points) as a function of rigidity. 117

4-3 The AMS F/B flux ratio with total errors as a function of rigidity. The brown curve shows the fit results with Eq. (4.2). 118

4-4 The AMS F/B flux ratio from 5 to 20 GV for two different time periods, May 19, 2011 to March 3, 2016 (blue dots) and March 3, 2016 to October 30, 2019 (magenta dots). For clarity, the data points are displaced horizontally. 119

4-5 The AMS fluorine flux as a function of kinetic energy per nucleon E_k multiplied by $E_k^{2.7}$ together with earlier measurements [50, 54–57]. . . 120

4-6 The AMS F/Si flux ratio (red dots) and AMS B/O flux ratio (blue dots) multiplied by $\tilde{R}^{0.3}$ with total errors as a function of rigidity. For display purposes, the B/O flux ratio is rescaled as indicated. The solid brown and blue curves show the F/Si and B/O fit results respectively with Eq. (4.4). The dotted and dashed red curves show the predictions of the F/Si ratio by the GALPROP model [104] and the GALPROP-HELMOD [23] model, respectively. 122

4-7 The AMS [(F/Si)/(B/O)] ratio as a function of rigidity with total errors. The solid blue curve shows the fit results of Eq. (4.6). 123

4-8 The AMS [(F/Si)/(B/O)] ratio below 20 GV for two different time periods, May 19, 2011 to March B/O 3, 2016 (blue dots) and March 3, 2016 to October 30, 2019 (magenta dots). For clarity, the data points are displaced horizontally. 124

4-9 The AMS a) Na (magenta points) and b) Al (blue points) fluxes together with the rescaled AMS N (green points) flux [60] multiplied by $\tilde{R}^{2.7}$ with total errors as functions of rigidity. 126

4-10 The AMS a) Na (magenta points) and b) Al (blue points) flux spectral indices together with N (green points) flux spectral index [60] as functions of rigidity. 127

4-11 The AMS a) Na flux and b) Al flux as functions of kinetic energy per nucleon E_K multiplied by $E_K^{2.7}$ together with earlier measurements [42, 50, 54–57]. The dashed blue lines show predictions of the latest GALPROP-HELMOD model [23]. 128

4-12 a) The AMS Na flux $\Phi_{\rm Na}$ fit to the weighted sum of the Si flux $\Phi_{\rm Si}$ and the F flux $\Phi_{\rm F}$ above 6 GV. b) The AMS Al flux $\Phi_{\rm Al}$ fit to the weighted sum of the Si flux $\Phi_{\rm Si}$ and the F flux $\Phi_{\rm F}$ above 6 GV, i.e. $\Phi_{\rm Al} = \Phi_{\rm Al}^{\rm P} + \Phi_{\rm Al}^{\rm S}$. In both a) and b), the contributions of the primary and secondary components are indicated by the shading (yellow and green, respectively). 130

4-13 a) $\Phi_{\rm N}/\Phi_{\rm O}$ and b) $\Phi_{\rm Na}/\Phi_{\rm Si}$ and c) $\Phi_{\rm Al}/\Phi_{\rm Si}$ as functions of rigidity. The contributions of the primary and secondary components are indicated by the shading (yellow and green, respectively). As seen, the contribution of the secondary component in all three fluxes decreases, and the contribution of the primary component correspondingly increases with rigidity. Note that for nitrogen, the fit starts from 2.15 GV and for Na and Al from 6 GV. 131

4-14 a) Φ_{Na}/Φ_{Si} and b) Φ_{Al}/Φ_{Si} as functions of rigidity. The contributions of the primary and secondary components obtained by fits with the slab model are indicated by the shading (yellow and green, respectively). The dashed vertical lines at 6 GV show the lower boundary of the fit range. 134

4-15 The fluxes of cosmic nuclei measured by AMS as a function of rigidity from $Z = 2$ to $Z = 14$ above 30 GV [60, 61, 63, 109]. For clarity, data points above 400 GV are displaced horizontally. Fluxes are rescaled as indicated for display purposes. The shaded bands are to guide the eye. 135

List of Tables

1.1 Summary of recent examples of balloon-borne experiments [38–46]. Note that the quoted date indicates the first flight of the experiment if several flights were made. 36

4.1 The N [60], Na, and Al cosmic ray nuclei primary Φ^{P}_{N}, Φ^{P}_{Na}, and Φ^{P}_{Al} and secondary Φ^{S}_{N}, Φ^{S}_{Na}, and Φ^{S}_{Al} flux components, and their corresponding primary fractions Φ^{P}_{N}/Φ_{N}, Φ^{P}_{Na}/Φ_{Na}, and Φ^{P}_{Al}/Φ_{Al} at 6 GV, 100 GV, and 2 TV. 129

Chapter 1

Introduction

The Alpha Magnetic Spectrometer (AMS) is a precision particle physics detector on the International Space Station (ISS) conducting a unique, long-duration mission of fundamental physics research in space. The physics objectives include precise studies of the origins of dark matter, antimatter, and cosmic rays as well as the exploration of new physics phenomena.

Over the last decade, the energy spectrum of individual cosmic ray species has been measured by AMS with unprecedented precision, revealing many new and unexpected properties of cosmic rays and challenging the current theoretical understanding of cosmic ray physics.

This thesis focuses on the precision measurement of fluorine, sodium, and aluminum fluxes in cosmic rays, and is organized as follows:

Chapter 1 is an introduction to cosmic ray physics, reviewing the previous experimental observations of cosmic rays, and describing the theory of galactic cosmic ray acceleration and propagation mechanisms.

Chapter 2 describes the setup and performance of the AMS detector, which will focus on the sub-detectors used in this analysis, namely the silicon tracker and the time of flight detectors.

Chapter 3 discusses in detail my work on the measurements of the fluorine, sodium, and aluminum fluxes. The factors entering the flux measurements include the event selection, the exposure time evaluation, the acceptance calculation, the trigger effi-

ciency, the estimate of the background, and the unfolding of the flux. The systematic uncertainty studies are also presented.

Chapter 4 presents the results: the measured fluorine, sodium, and aluminum fluxes as well as physics interpretations.

Chapter 5 presents the conclusion.

1.1 Cosmic Rays

Cosmic rays are mainly ionized nuclei, about 90% protons, 9% helium, and 1% heavier nuclei plus a small amount of electrons [1]. The first observation of cosmic rays dates back to 1912 when Victor Hess made a series of measurements of radiation in the atmosphere in balloon flights [2]. Ever since this discovery, cosmic rays are powerful tools to study new physics. Many new particles were discovered, including the positron [3], the muon [4], and pions [5].

Over the decades, an enormous number of experiments have been performed on the ground, on balloons, and on satellites. The principal data about cosmic rays are the relative abundances of the different nuclei (composition), the distribution in energy (energy spectrum) of all-particle and each component, and the distribution of arrival directions. These data contain information on the origin, acceleration, and propagation mechanisms of the cosmic rays.

1.1.1 Energy Spectrum

Figure 1-1 is an overview of the energy spectra of cosmic rays as a function of total energy per particle. Other ways to describe the spectra include: 1) by particles per unit rigidity R, where R is defined as momentum divided by the charge of the particle:

$$R = \frac{pc}{Ze}; \tag{1.1}$$

2) by particles per energy-per-nucleon. A remarkable feature of the cosmic ray spectrum is that it can be approximately described by power laws over large intervals of

energy:

$$\frac{dN}{dE} \propto E^{\gamma}, \tag{1.2}$$

where the parameter γ is the differential spectral index of the cosmic ray spectrum [1].

The spectral index changes with energy. From 10^{10} eV to 10^{15} eV the differential spectral index is $\gamma \approx -2.7$. From 10^{15} eV to 10^{18} eV the differential spectral index is $\gamma \approx -3.1$. Above 10^{18} eV the differential spectral index is $\gamma \approx -2.6$, and then it apparently cuts off around 10^{20} eV. The transition regions are known as the "knee" ($\sim 3 \times 10^{15}$ eV), and the "ankle" ($\sim 3 \times 10^{18}$ eV). This change of the spectral index indicates the change of the physics processes in the region. Cosmic rays up to the knee are thought to be of galactic origin and accelerated by the shock waves produced in supernovae explosions. Cosmic rays then propagate through the Galaxy, being deflected many times by randomly oriented magnetic fields before eventually reaching the solar system [1]. Two main effects cause the knee: 1) most cosmic accelerators in the Galaxy have reached their maximum energy; 2) at the same energy the propagation volume reaches the galactic magnetic field confinement and cosmic rays are more likely to escape our Galaxy [6]. Since these two effects depend on the magnetic rigidity R of the particles, the energy spectra for individual elements should exhibit different cutoffs for different total energies [7]. The ankle is associated with the emergence of particles of extragalactic origin [1]. One possibility is that it is the result of a higher energy population of particles overtaking a lower energy population, for example, an extragalactic flux beginning to dominate over the galactic flux [8]. Then the galactic cosmic rays do not contribute significantly to the flux above 10^{18} eV, consistent with the maximum expected range of acceleration by supernova remnants [6]. The cutoff at around 10^{20} eV is due to the GZK effect [9], i.e., the interaction of ultra-high-energy cosmic ray protons and nuclei with the cosmic microwave background which results in a drastic reduction of the observed flux above 5×10^{19} eV.

The origin of spectral structures in the cosmic-ray flux, where the spectrum deviates from a single power law, has been a topic under study for decades. These

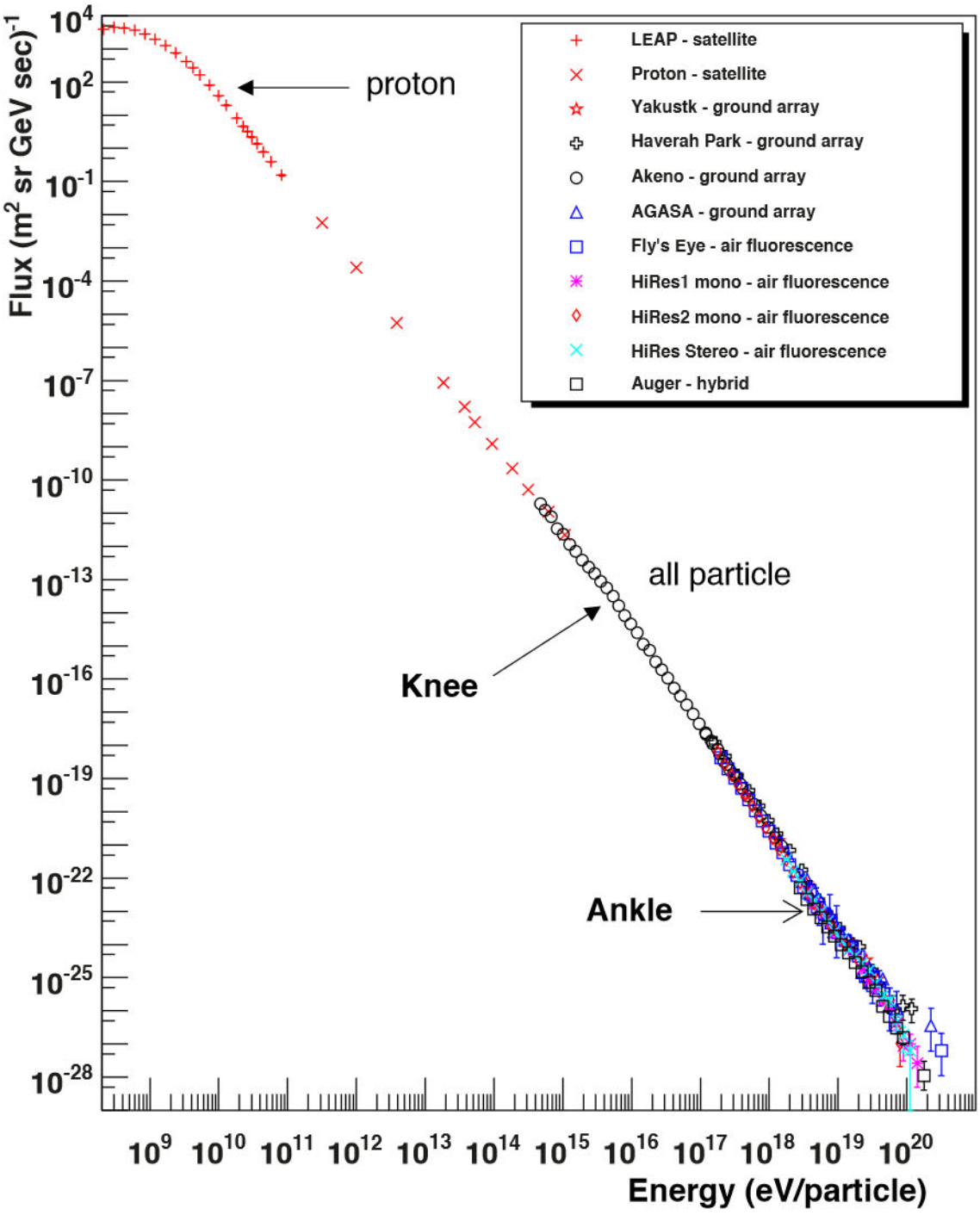

Figure 1-1: Overview of energy spectra of cosmic rays before AMS. The red cross markers below 10^{11} eV represent the measured spectrum of protons. All other data represent all-particle cosmic ray energy spectrum. Figure is from Ref. [1].

longstanding questions challenge the current cosmic-ray theories and indicate the existence of new physics.

1.1.2 Chemical Composition

Precise knowledge of the chemical composition of cosmic rays provides essential information about the origin and propagation history of cosmic-ray particles. One particular way is to compare the relative abundances of nuclear species in cosmic rays with those in the solar system, as shown in Figure 1-2.

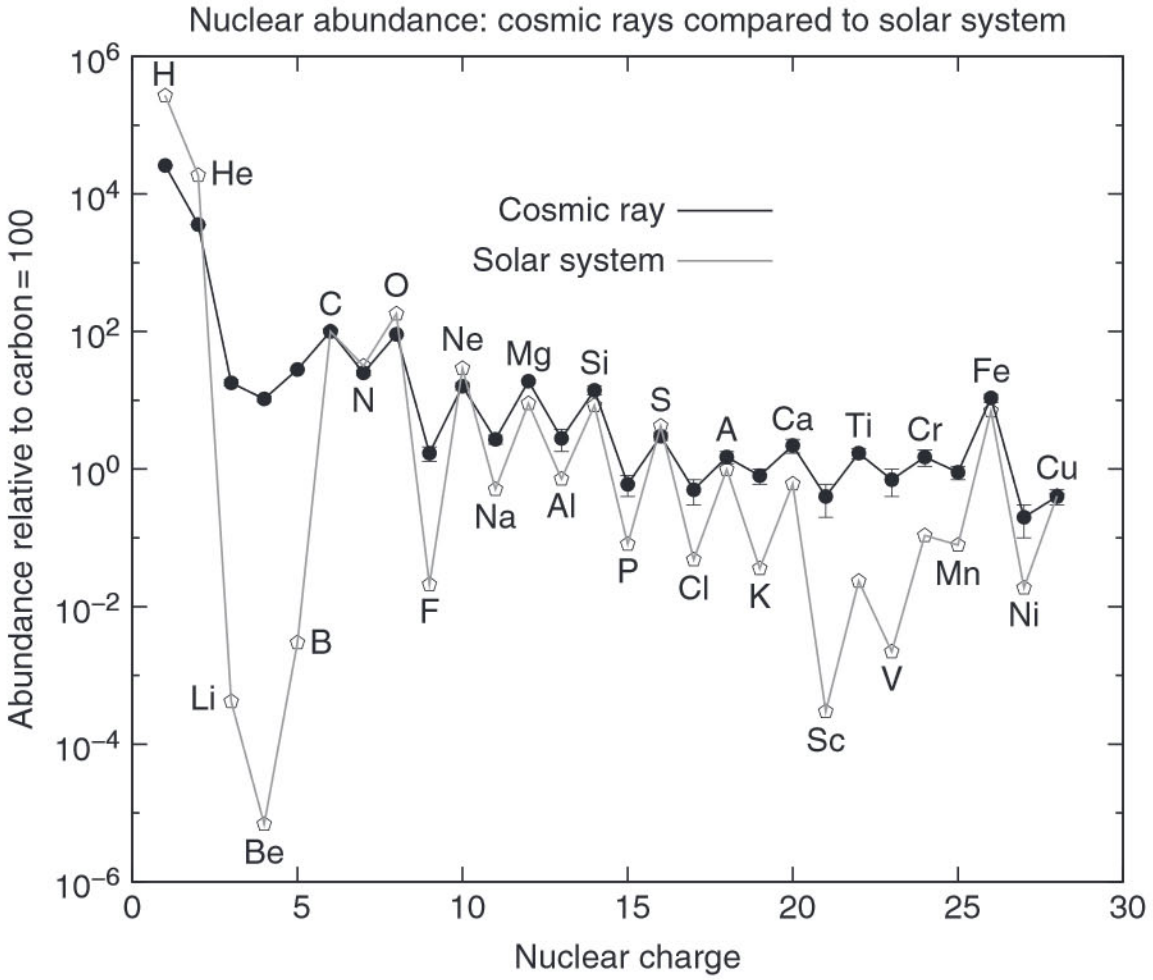

Figure 1-2: Comparison of the elemental abundances in cosmic rays (solid dots) and in the solar system (open symbols), all relative to carbon = 100. Figure is from Ref. [10].

The chemical composition of the cosmic rays is similar to the abundances of the elements in the solar system with some important exceptions, particularly for the elements like Li, Be, B, F, and Sc, Ti, V, Cr, Mn which are many orders of magnitude more abundant in cosmic rays than in the solar system. These observations indicate that these elements are mainly produced during the propagation instead of in the source. Traditionally, according to their astrophysical origin, cosmic rays fall into two categories, primary cosmic rays and secondary cosmic rays. Primary cosmic rays are thought to be mostly produced during the lifetime of stars and accelerated in supernovae shocks in our Galaxy. Secondary cosmic rays are produced by collisions of heavier elements with the interstellar medium (ISM). The secondary-to-primary ratios of cosmic rays can be used as a probe to study cosmic-ray propagation.

1.1.3 Sources and Acceleration of Cosmic Rays

The origin of cosmic rays is one of the most debated fields in astrophysics. Nevertheless, the common idea is that galactic cosmic particles are mostly produced during stellar nucleosynthesis and are accelerated by shock waves produced by supernovae explosions in our Galaxy. From the energetic point of view, supernovae can explain the energy density of cosmic rays. Considering the galactic disc with a thickness of $d \approx 200$ pc and radius of $R_G \approx 15$ kpc, and taking into account that the estimate of the energy density in cosmic rays is $\rho \sim 0.5$ eV/cm^3 [1], and the confinement time of the cosmic rays in the galactic disk is $\tau_{esc} \sim 15 \times 10^6$ yrs [11], the source power is estimated to be

$$P_S = \frac{\rho V}{\tau_{esc}} = \frac{\rho \pi R^2 d}{\tau_{esc}} \sim 8 \times 10^{40} \text{ erg/s}. \tag{1.3}$$

The average energy released by a supernova explosion is about $1.6{\times}10^{51}$ erg, ejected with a mean velocity of $v \sim 5 \times 10^8$ cm/s. The supernova rate for the Galaxy has been estimated to be about 3 supernovae per century [12], so the total output power is $P_{SN} \sim 3 \times 10^{42}$ erg/s. In order to explain the measured cosmic-ray power in the Galaxy, a conversion factor for the supernova energy to the cosmic ray energy in the range of 1% to 10% is needed, and it is well compatible with current supernova

models.

Fermi acceleration, proposed by Enrico Fermi in 1949 [13], is widely used to describe the acceleration mechanism of cosmic rays. There are two types of Fermi acceleration.

First-order Fermi acceleration is used to describe the acceleration that takes place directly at the source. Charged particles gain energy interacting with the shock waves produced by supernovae explosions: this happens when the particle crosses the shock front and, after diffusing in the nearby turbulent magnetic field, returns to the shock itself. A particle can be accelerated to higher energies after accumulating many interactions of this kind, with a probability decreasing at each shock front crossing. The energy increases with the first order in v/c, where v is the shock front velocity. The resulting energy spectrum of many particles undergoing this process turns out to be a power law

$$N(E)dE \propto E^{\gamma}dE \tag{1.4}$$

with $\gamma \sim -2$ independent of the properties of the shock wave and magnetic fields [14], and its spectral index is not too different from the observed value of ~ -2.7 for galactic cosmic rays.

Second-order Fermi acceleration takes place during propagation (see Section 1.1.4), when a charged particle enters slowly moving magnetized clouds. Since the magnetic irregularities of the field are random, the multiple scattering process inside the cloud can be considered as a random walk. The global effect is a gain of energy proportional to β^2, where $\beta = v/c$ and v is the cloud velocity [1], thus this acceleration is less effective than the first-order Fermi acceleration.

1.1.4 Cosmic-ray Propagation

After escaping the source, cosmic rays are injected into the Galaxy, and they interact with the ISM. Cosmic-ray propagation in the Galaxy is therefore a complex subject that requires taking into account many different physical processes.

1.1.4.1 The Slab Model

The slab model is a simplified model [1] using the path length to characterize cosmic-ray propagation. In the framework of this model, the amount of material traversed by a particle is expressed by the grammage, $\xi = \rho x = \rho v t$, where v is the velocity of the particle and ρ is the matter density. The slab model assumes that all the particles traverse the same amount of material between 0 and ξ.

The differential equation that describes the abundance of primary nuclei is

$$\frac{dN_{\mathrm{P}}(\xi)}{d\xi} = -\frac{N_{\mathrm{P}}(\xi)}{\xi_{\mathrm{P}}} \tag{1.5}$$

where ξ_{P} is the mean free path for inelastic collisions, and $\xi = 0$ means at source. By integrating the equation above,

$$N_{\mathrm{P}}(\xi) = N_{\mathrm{P}}(0) exp(-\xi/\xi_{\mathrm{P}}). \tag{1.6}$$

1.1.4.2 The Leaky-box Model

The leaky-box model describes the propagation of primary cosmic ray nuclei based on simplifying assumptions. The leaky-box model [1] assumes that high-energy particles diffuse freely inside the confinement volume in which particles are injected by q uniformly distributed sources, and the volume is filled with a uniform distribution of matter and radiation fields. Cosmic rays can escape from this volume with a characteristic escape time τ_{esc}.

Considering number density $\psi(E)$ of only one cosmic-ray species and neglecting energy losses, the basic leaky box model equation can be written as

$$\frac{\partial \psi(E)}{\partial t} = q(E) - \frac{\psi(E)}{\tau_{esc}}. \tag{1.7}$$

In the steady state, Eq. (1.7) becomes $\psi(E) = \tau_{esc} q(E)$.

1.1.4.3 Diffusion Theory

The diffusion model with inclusion of convection provoked by the galactic wind provides an adequate description of cosmic-ray propagation in the Galaxy at energies below 10^{17} eV [15]. In this model, cosmic-ray propagation can be described by the transport equation, for a single species labelled by i:

$$\begin{aligned}\frac{\partial \psi_i(\vec{r},p,t)}{\partial t} = q_i(\vec{r},p,t) + \vec{\nabla}\cdot(D_{xx}\vec{\nabla}\psi_i - \vec{V}\psi_i) + \frac{\partial}{\partial p}p^2 D_{pp}\frac{\partial}{\partial p}\frac{1}{p^2}\psi_i \\ -\frac{\partial}{\partial p}[\dot{p}\psi_i - \frac{p}{3}(\vec{\nabla}\cdot\vec{V})\psi_i] - \frac{1}{\tau_f}\psi_i - \frac{1}{\tau_r}\psi_i,\end{aligned} \tag{1.8}$$

where $\psi_i(\vec{r},p,t)$ is the cosmic-ray density per unit of total particle momentum p at position $\vec{r}$; $q(\vec{r},p,t)$ is the source term including primary, spallation, and decay contributions.

The evolution of the cosmic-ray density depends on several parameters:

1. Cosmic rays propagate through the Galaxy under the influence of the galactic magnetic fields, which tangle their trajectories. The bending of the charged particle direction in the magnetic field is determined by the particle rigidity R, defined in Eq. (1.1). Different particles with the same rigidity are equally affected by the magnetic fields. D_{xx} describes the diffusion in position space. D_{xx} is proportional to $\beta D_0(\frac{R}{R_0})^\delta$ due to the turbulent nature of the perturbations in the galactic magnetic field [16], where D_0 is the diffusion coefficient at some reference rigidity R_0, and δ reflects the rigidity dependence of diffusion. In the Kolmogorov model $\delta = 1/3$ [17] and in the Kraichnan model $\delta = 1/2$ [18]. The slope of the rigidity dependence of the secondary-to-primary ratio is used to infer limits on the value of the spectral index δ for the diffusive propagation in the turbulent galactic magnetic fields [19, 20].

   In addition to the spatial diffusion, the interaction with the turbulent galactic fields induces a re-acceleration (second-order Fermi acceleration). This process is modeled by a diffusion in momentum space with a coefficient $D_{pp} \propto |\vec{V}_A|^2/D_{xx}$, where the Alfvén velocity V_A is the characteristic velocity

of the fluctuation propagation in the magnetic field. This term has a very large effect on the secondary-to-primary ratios, especially at low energies [19, 20].

2. $\vec{V}$ is the convection velocity, and relevant terms describe the density change due to convection.

3. Nuclear processes: Unstable nuclei can decay into other nuclear products, thus decreasing their density by the factor $\frac{1}{\tau_r}\psi_i$. τ_r is the timescale for radioactive decay, which is proportional to the half-life of the particle. Spallation processes of cosmic nuclei with the ISM also contribute to the evolution of the density. τ_f is the timescale for loss by fragmentation, which depends on the total spallation cross section and the density of the ISM.

4. Energy losses: During the propagation in the ISM, cosmic rays suffer energy losses due to interactions with the environment. Nuclei mainly lose energy by ionization. $\dot{p} = dp/dt$ is the momentum gain or loss rate.

The solution of Eq. (1.8) in the steady-state assumption $\frac{\partial \psi_i(\vec{r},p,t)}{\partial t} = 0$ completely describes the Local Interstellar Spectrum (LIS) for each species before entering the solar system. The equation can be solved numerically using dedicated packages like DRAGON [21] or GALPROP [22].

The GALPROP model [22] uses astronomical information and cosmic-ray measurements as inputs to numerically solve the cosmic-ray transport equation Eq. (1.8) for a given source distribution and boundary conditions for all cosmic-ray species. The propagation parameters that characterize the model of cosmic-ray propagation are inferred by the solution of the equation with constraints from experimental data. The GALPROP-HELMOD model [23] is a further development accounting for the cosmic-ray transport within the heliosphere, which is referred to the solar modulation. Solar modulation is significant for particles with low rigidity (less than $\sim$ 20 GV); particles with rigidity larger than 20 GV are less affected.

1.1.5 Cosmic-ray Measurements

The presence of the Earth's atmosphere prevents the direct measurements of cosmic rays at ground level. Experiments dedicated to the direct measurements of cosmic rays have to be operated above the atmosphere. However, the technological constraints limit the instrument acceptance to the detection of cosmic rays up to the TeV range. In order to detect cosmic rays above this energy, experiments have to be sited on the ground, where the effective sensitive area can be increased to hundreds of km^2.

In the following sections, examples of different types of cosmic-ray experiments are reviewed.

1.1.5.1 Ground-based experiments

Ground-based experiments do not measure cosmic rays directly, since cosmic-ray particles that enter the Earth's atmosphere interact with the medium, leading to the production of a particle shower.

During the shower development from incident protons and nuclei, the chain of decays of short-lived hadrons produces different types of particles. At the end of the decay chain, apart from the hadronic components, γ and $e^{\pm}$ constitute the so-called electromagnetic components; $\mu^{\pm}$ and ν constitute the penetrating component. All components travel approximately along the same direction of the incoming cosmic-ray particle, with different spreads around the axis depending on the components. On the ground, Extensive Air Shower (EAS) arrays measure the development of such showers in order to infer the properties of the incident cosmic-ray particle.

Usually, EAS arrays are constituted by a set of detectors spread over a large area to collect large enough statistics at high energy, where the cosmic-ray flux is very low. Scintillator detectors, water Cherenkov tanks, and muon detectors are used to measure the radiation at the EAS array altitude. The amount of muonic and electromagnetic components, the difference in the arrival time, and the reconstruction of the shower front are used to infer the properties of the cosmic-ray particle. In addition, Cherenkov light telescopes can be incorporated to measure the light emitted by the relativistic

components to provide further information. Finally, the fluorescence light emitted from the de-excitation of nitrogen can be detected to measure the shower profile for cosmic-ray particles above 10^{18} eV.

The ground-based cosmic-ray measurements are subject to large uncertainties, dominated by the limited knowledge of the atmospheric parameters and high-energy shower development. The properties of the cosmic-ray particle are inferred through simulation of shower developments in the atmosphere [24]. The uncertainties in the hadronic interactions of cosmic rays with air nuclei represent another unavoidable uncertainty of the ground-based measurements [25]. On the other hand, EAS array measurements are, together with ultra-high-energy neutrino detectors, the only possibility so far to investigate the physics of the most energetic phenomena of the Universe.

The main features of the present experiments can be categorized depending on the energy range. For $10^{13} - 10^{15}$ eV, experiments are usually located at mountain levels (TIBET AirShower Array [26], HAWC [27], GRAPES [28], ..), the surface covered is at the order of $\sim 10^4$ m^2. For $10^{14} - 10^{18}$ eV, the experiments in this energy range span from sea level (KASCADE [29], Tunka [30], ..) to mountain level (IceTop [31], GAMMA [32], ..). The surface covered by these arrays spans from 10^4 to 10^6 m^2. For energies above 10^{18} eV, the main feature of the experiments is the huge surface covered by the arrays, represented by the Telescope Array experiment [33] covering an area of 7×10^8 m^2 and by the Pierre Auger Observatory [34] covering an area of 3×10^9 m^2 (3000 km^2).

Figure 1-3 shows examples of the high-energy cosmic-ray energy spectrums obtained from various ground-based measurements. Ground array experimental results have had a significant impact on the study of cosmic rays with the highest measured particle energies.

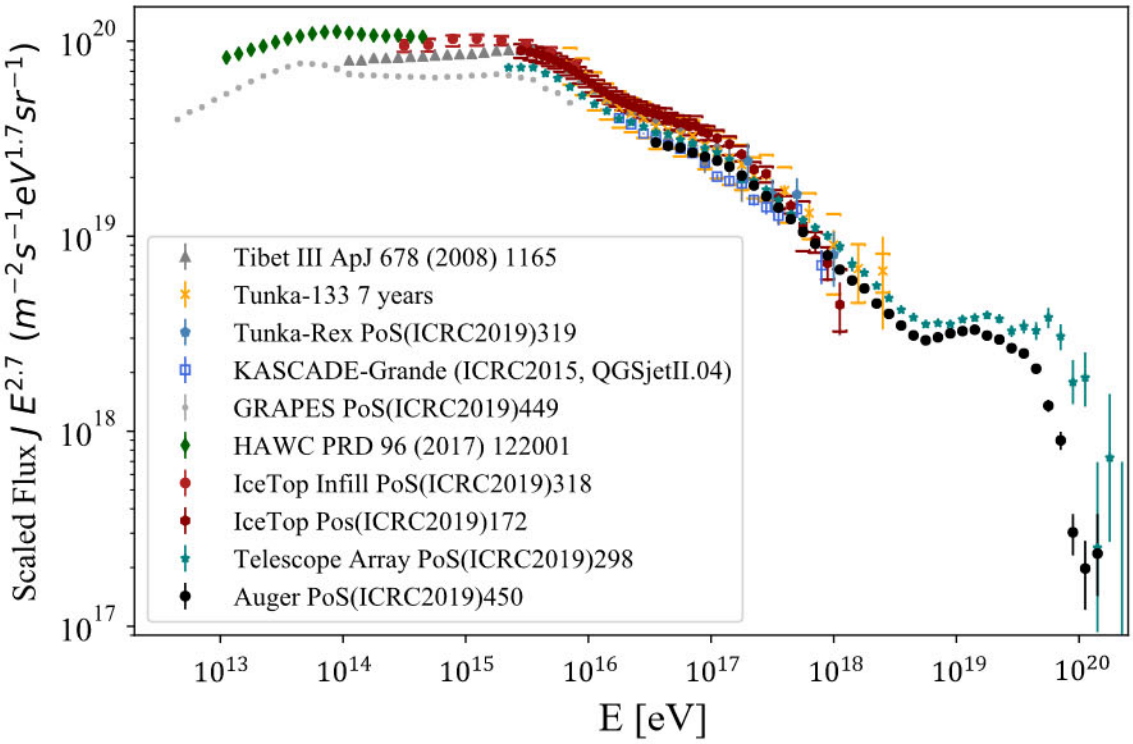

Figure 1-3: Energy spectrum of high-energy cosmic rays obtained from various ground-based measurements [26–31, 35, 36]. Figure is from Ref. [37].

1.1.5.2 Balloon-borne experiments

Ballon-borne experiments are cosmic-ray detectors carried by a large volume balloon that goes up to the stratosphere. These experiments are usually short-duration flights from a few hours to several days.

Balloon-borne experiments have played a major role in the cosmic-ray field since the 1930s. They were the only solution to almost directly explore cosmic radiation before space-borne technology was achieved. Balloon missions are both less expensive and often more convenient to conduct than space experiments, but the collected statistics are limited by flight time.

Roughly, balloon experiments can be categorized by their principle energy measurement techniques. Calorimetric techniques based on emulsion stacks were used by JACEE [38] and RUNJOB [39]. Modern calorimetric techniques are used by ATIC [40] and CREAM [41]. There are also Cherenkov experiments like CRISIS [42] and TIGER [43]. A quite different experimental approach is used in the TRACER [44]

experiment, where the measurement at high energy is based on the transition radiation detection. Spectrometers, like BESS [45] and CAPRICE [46], can measure the charge sign and are dedicated to antimatter and dark matter searches. Their acceptance is limited by the magnet size and their energy reach by the maximum spectrometer resolution.

A summary of recent examples of balloon-borne experiments is shown in Table 1.1.

Experiment	Energy Measurement Technique	Charge Range	Energy Range	Date
CRISIS	Cherenkov	$10 \leq Z \leq 28$	0.4 GeV - 0.9 GeV/n	1977
JACEE	Emulsion	$1 \leq Z \leq 26$	10 - 1000 TeV/n	1979
BESS	Magnetic Spectrometer	$\|Z\| = 1, 2$	0.2 GeV - 1 TeV/n	1993
CAPRICE	Magnetic Spectrometer	$\|Z\| = 1, 2$	0.2 - 200 GeV/n	1994
RUNJOB	Emulsions	$1 \leq Z \leq 26$	10 - 1000 TeV/n	1995
TIGER	Cherenkov	$26 \leq Z \leq 40$	0.4 GeV - 0.9 GeV/n	1997
TRACER	TRD	$8 \leq Z \leq 28$	0.01 - 200 TeV/n	1999
ATIC	Calorimeter	$1 \leq Z \leq 26$	0.1 - 100 TeV/n	2002
CREAM	Calorimeter	$1 \leq Z \leq 28$	0.1 - 1000 TeV/n	2004

Table 1.1: Summary of recent examples of balloon-borne experiments [38–46]. Note that the quoted date indicates the first flight of the experiment if several flights were made.

1.1.5.3 Space-borne experiments

The measurement of cosmic rays in space began in the 1970s with the measurement of nuclear isotopes in the energy range less than 1 GeV with the IMP satellites [47]. The isotopic composition measurement has also been carried out by the High Energy Telescopes (HET) flying with the Voyager 1, Voyager 2 [48] and the CRIS instrument on the ACE satellite [49]. All these instruments are characterized by solid-state silicon detectors to distinguish a wide number of isotopes.

In the 1980s, the cosmic-ray chemical composition up to $Z = 28$ has been measured with high statistics by two experiments: the C2 experiment, an ensemble of Cherenkov counters aboard the NASA HEAO-3 satellite [50] and the CRN experiment, an instrument based on a transition radiation detector onboard of the Shuttle Challenger in the mission Spacelab-2 [51]. The cosmic-ray chemical composition has also been measured by the Ulysses HET [52] from 1990 to 2009.

The PAMELA experiment on the Russian satellite Resurs-DK1 [53] was launched in 2006 and terminated in 2016. The instrument combines several particle physics detection techniques, such as a Magnetic Spectrometer, an imaging Calorimeter, a Time of Flight System, scintillation counters, and a dedicated neutron counter.

1.2 Previous Measurements on Fluorine, Sodium, and Aluminum Cosmic Rays

In the past few decades, most of the measurements were performed by experiments with balloons and satellites with limited statistics. The results of the fluorine [50,54–57], sodium [42,50,54–57], and aluminum [42,50,54–57] measurements before AMS are presented in Figure 1-4, Figure 1-5, and Figure 1-6 respectively. Data points are extracted using Ref. [58]. There have been no measurements of the fluorine (F), sodium (Na), and aluminum (Al) fluxes as functions of rigidity. The previous measurements, show errors larger than 50% at $\sim$ 50 GeV/n. For fluorine, the measurement errors exceed 100% at $\sim$ 50 GeV/n.

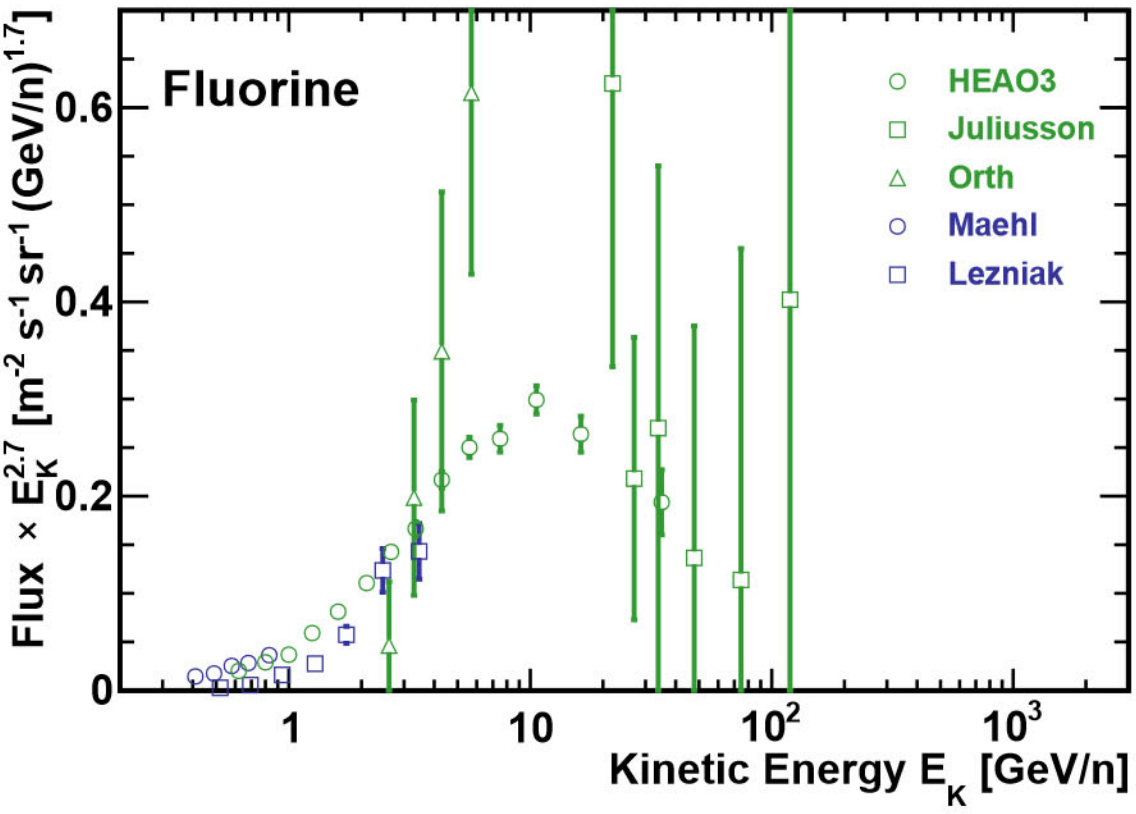

Figure 1-4: Previous measurements of fluorine fluxes.

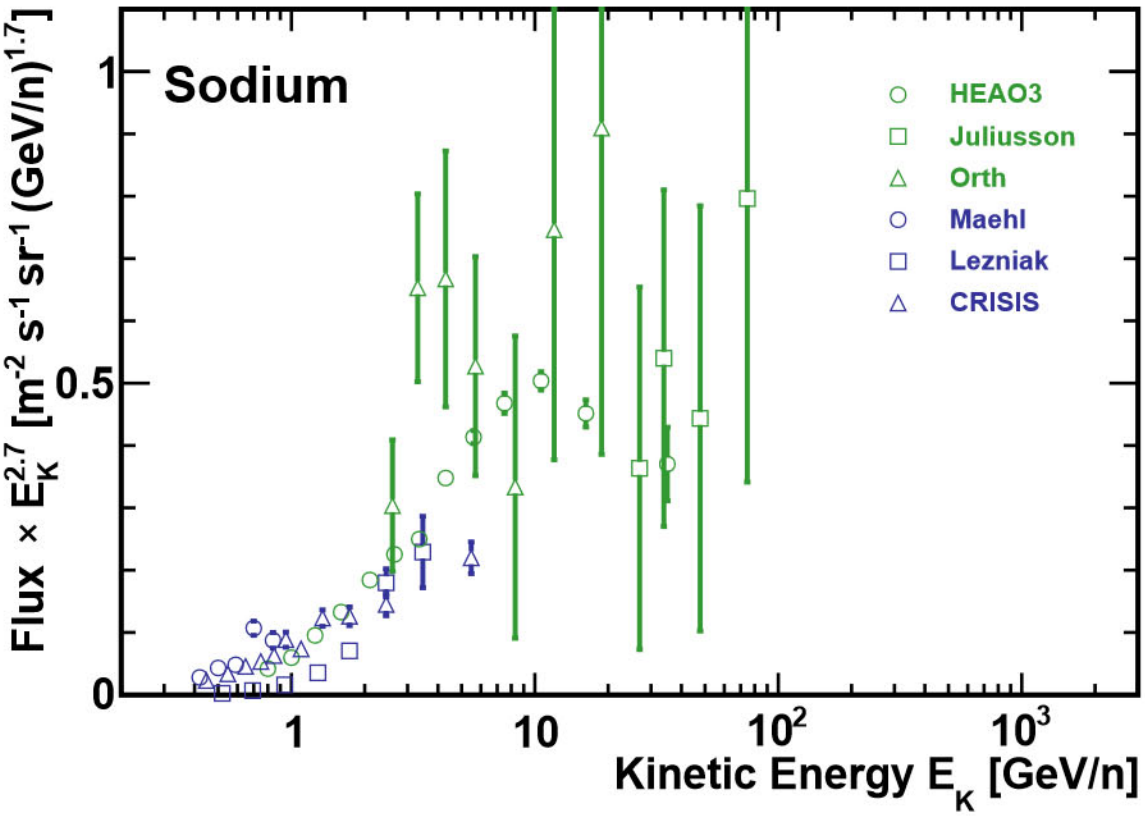

Figure 1-5: Previous measurements of sodium fluxes.

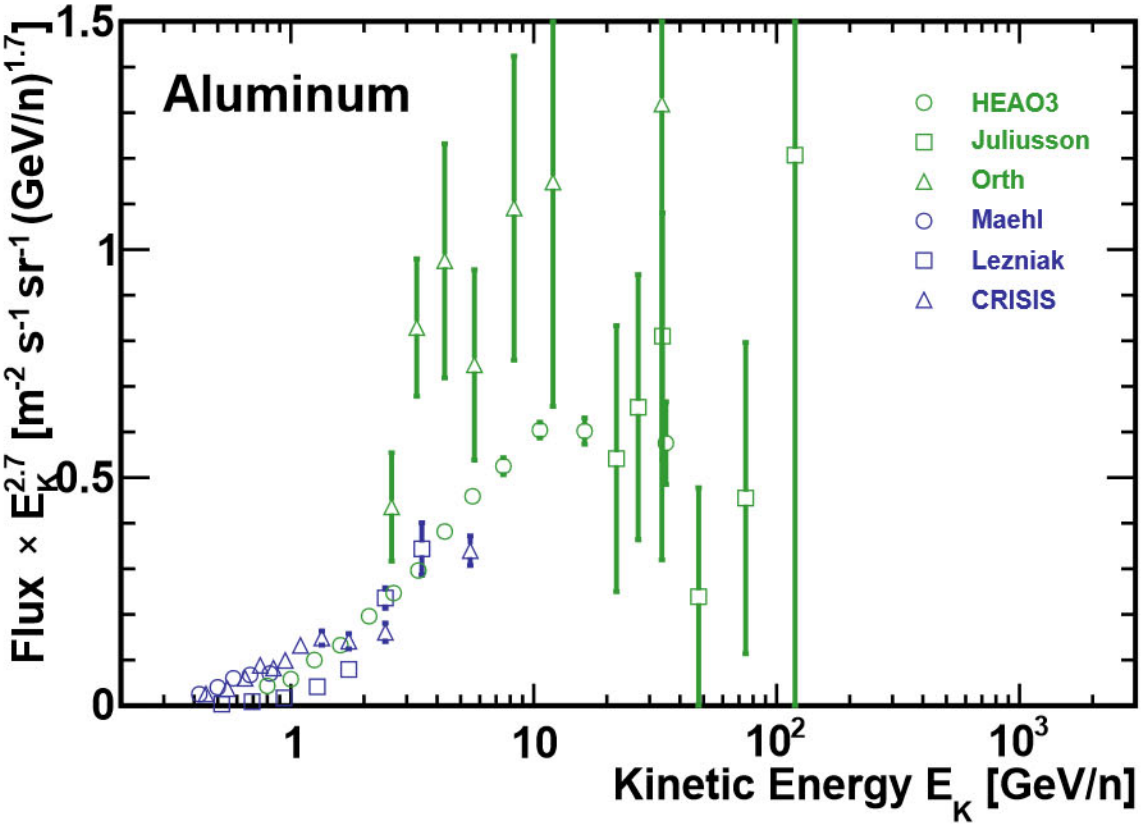

Figure 1-6: Previous measurements of aluminum fluxes.

1.3 Motivation for Measuring Fluorine, Sodium, and Aluminum Cosmic Rays

As presented in Section 1.2, measurements on fluorine, sodium, and aluminum cosmic rays before AMS could not reveal possible spectral structures due to limited statistics. AMS has the capability to measure the fluxes of cosmic-ray fluorine, sodium, and aluminum nuclei up to 3 TV with an unprecedented level of precision.

The secondary-to-primary flux ratios of light nuclei in cosmic rays, in particular, B/C or the more direct B/O, have been traditionally used to study the propagation of cosmic rays in the Galaxy [59]. Examples for using the B/C ratio to constrain the diffusion coefficient D_{xx}^0 and V_A (in Eq. (1.8)) with the GALPROP model can be found in [19, 20]. In previous publications, AMS has shown that all light secondary-to-primary ratios, Li/C, Li/O, Be/C, Be/O, B/C, and B/O, deviate from a single power law (harden[1]) above 200 GV [60, 61]. This strongly favors the hypothesis that the hardening of all light cosmic rays is due to propagation effects [62].

Recently, AMS has also studied the properties of the heavy primary Ne, Mg, and Si fluxes [63] and found that they form a separate class of primary cosmic rays. Then it is particularly interesting to study the properties of heavy secondary fluxes, comparing to light secondary nuclei like B, and whether heavy secondary-to-primary flux ratio behaves similar to the light secondary-to-primary flux ratio like B/O.

Fluorine is the only purely secondary cosmic ray between oxygen and silicon [23, 64]. Differences in the rigidity dependence of the F flux and light secondary cosmic ray Li, Be, and B fluxes, as well as differences in the rigidity dependence of light (B/O) and heavy (F/Si) secondary-to-primary flux ratios, provide new important insights on cosmic ray propagation.

Previously, AMS found that the nitrogen spectral index is situated between the primary He-C-O and secondary Li–Be–B cosmic ray spectral indices. In particular, the nitrogen flux is well described over the entire rigidity range by the sum of the primary flux equal to 9.2% of the oxygen flux and the secondary flux equal to 61%

[1]The hardening of the flux means the spectral index becomes larger.

of the boron flux. Precise knowledge of the primary component of cosmic nitrogen provides important insights into the details of nitrogen production in astrophysical sources, while precise knowledge of the secondary component of the cosmic nitrogen provides insights into the details of propagation processes of cosmic rays in the Galaxy.

Following the study of nitrogen, it is of great interest to study the heavy sodium and aluminum cosmic rays, which are also thought to be produced both in astrophysical sources and by the collisions of heavier nuclei with the interstellar medium [23,64]. Making use of the AMS measured heavy primary silicon flux and heavy secondary fluorine flux, the precise knowledge of the primary contribution of the sodium and aluminum fluxes sheds light on the production of sodium and aluminum nuclei at source, and the precise knowledge of the secondary contribution of the sodium and aluminum fluxes reveal the details of production of secondary sodium and aluminum nuclei during the propagation processes of cosmic rays in the Galaxy.

AMS measurements have generated new developments in cosmic-ray theoretical models [59, 65]. In particular, the AMS nuclei flux measurements from He to Si are used in the newest cosmic-ray propagation model GALPROP-HELMOD [23,62]. But it should be noted that the theoretical models have their limitations, as so far none of them predicted the AMS observed spectral behavior of the cosmic rays. Thus, new results from AMS will provide important data to further understand cosmic-ray physics and develop cosmic-ray theoretical models.

Chapter 2

The Alpha Magnetic Spectrometer

The Alpha Magnetic Spectrometer (AMS) is a large acceptance particle physics detector operating on the International Space Station (ISS) since May 2011 to conduct a unique long-duration mission (∼20 years) of fundamental physics research in space. During the first 8.5 years of operations, 150 billion events have been collected by the instrument .

In this chapter, a general overview of the AMS instrument and its operation in space is presented.

2.1 AMS Detector

Figure 2-1 shows a schematic view of AMS. It consists of a transition radiation detector (TRD), four planes of time of flight counters (TOF), 9 layers of silicon tracker, a permanent magnet, a ring imaging Cherenkov detector (RICH), an electromagnetic calorimeter (ECAL) and an array of 16 anti-coincidence counters (ACC).

The status of the subdetectors is continuously monitored by the AMS Payload Operations Control Center (POCC) located at CERN, Geneva.

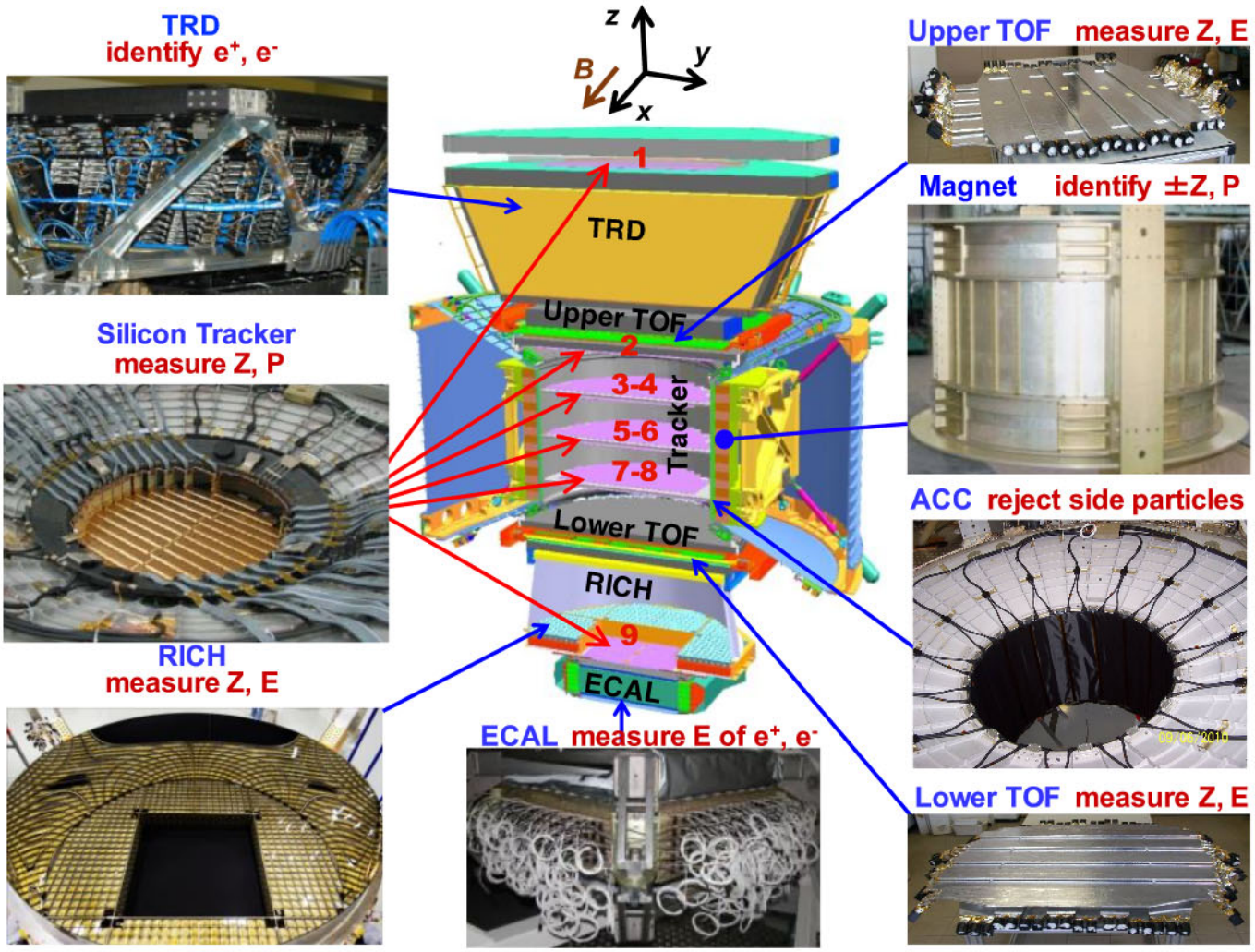

Figure 2-1: Schematic view of the AMS. The sub-detectors are labelled.

2.1.1 Permanent Magnet

Figure 2-2 shows a photograph of the magnet. The magnet is made of 64 sectors arranged in a cylindrical shape with an inner diameter of 115 cm, an outer diameter of 129.9 cm, and a height of 80 cm. Each sector is composed of 100 high-grade Neodymium-Iron-Boron blocks glued together with epoxy [66].

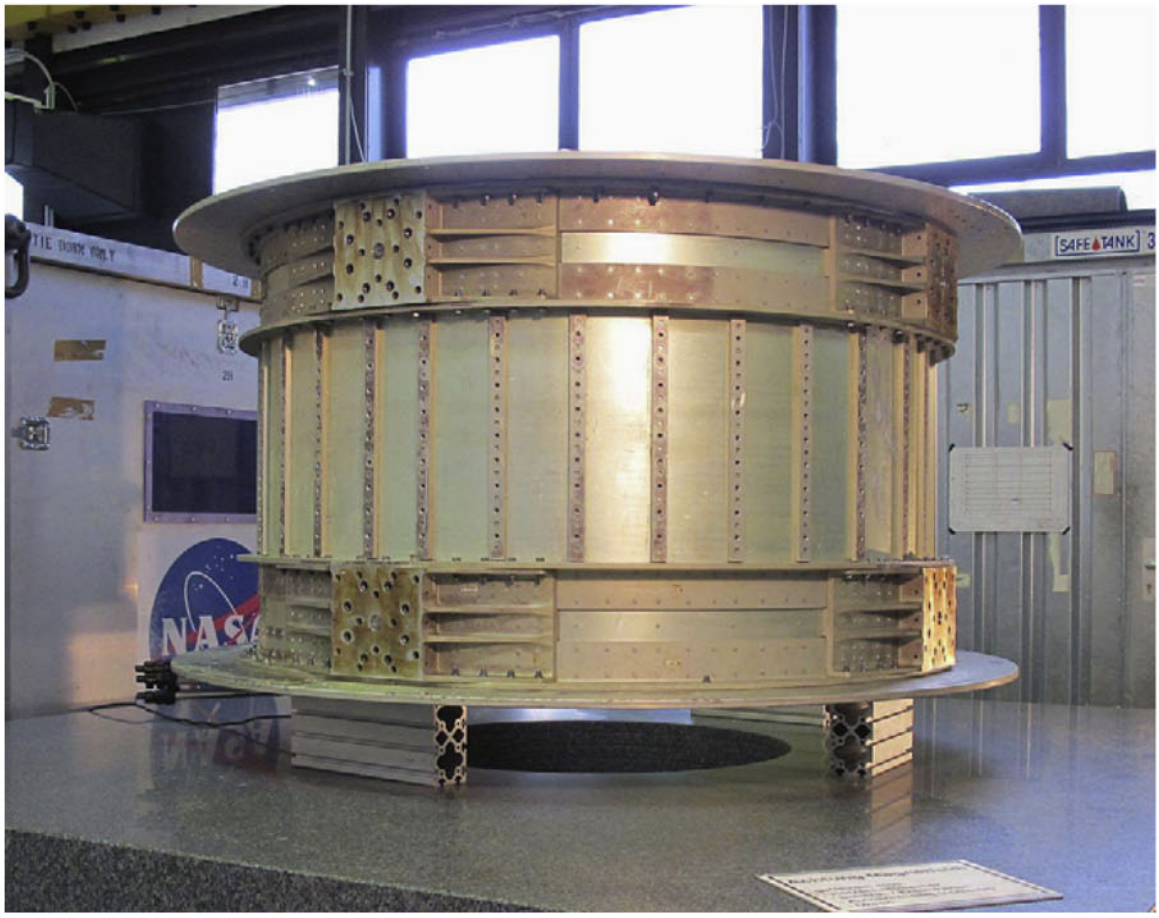

Figure 2-2: AMS permanent magnet.

The magnet defines the reference frame for AMS with its origin at the center of the magnet, as can be observed in Figure 2-3. The Z-axis runs along the cylinder's axis of symmetry, with positive values in the direction of the top of the instrument. The X-axis is aligned to the magnetic field lines, while the Y coordinate describes the bending direction. With this choice of the reference system, the bent trajectories of all charged particles traversing the magnet are contained in the Y-Z plane.

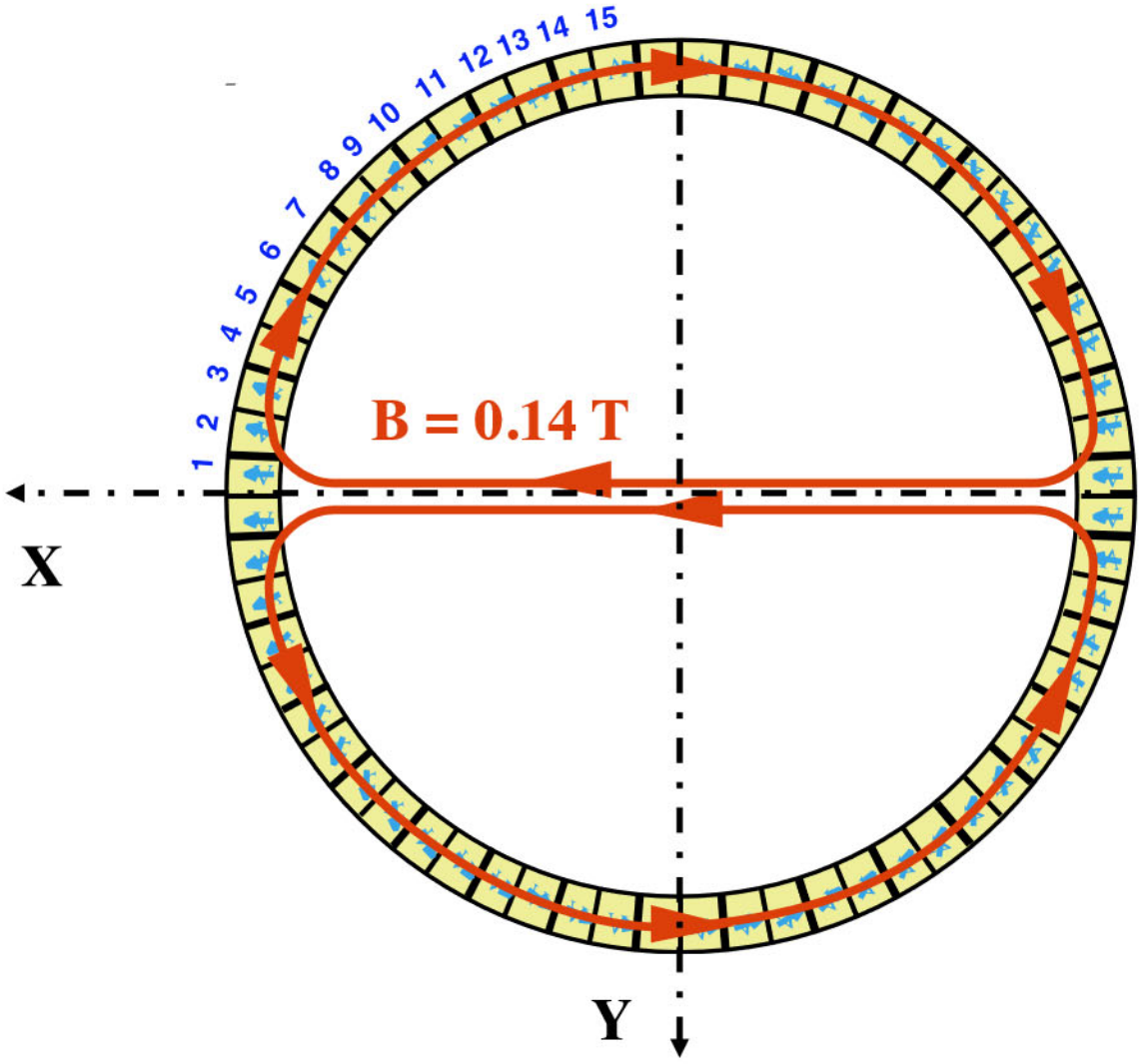

Figure 2-3: Magnetic field orientation of the AMS Permanent Magnet.

The magnetic field is 0.14 T at the center of the magnet, with a negligible dipole moment outside the magnet. Detailed measurements of the magnetic field were made in both 1997 and 2010. As shown in Figure 2-4, the change of the field intensity was within 1%.

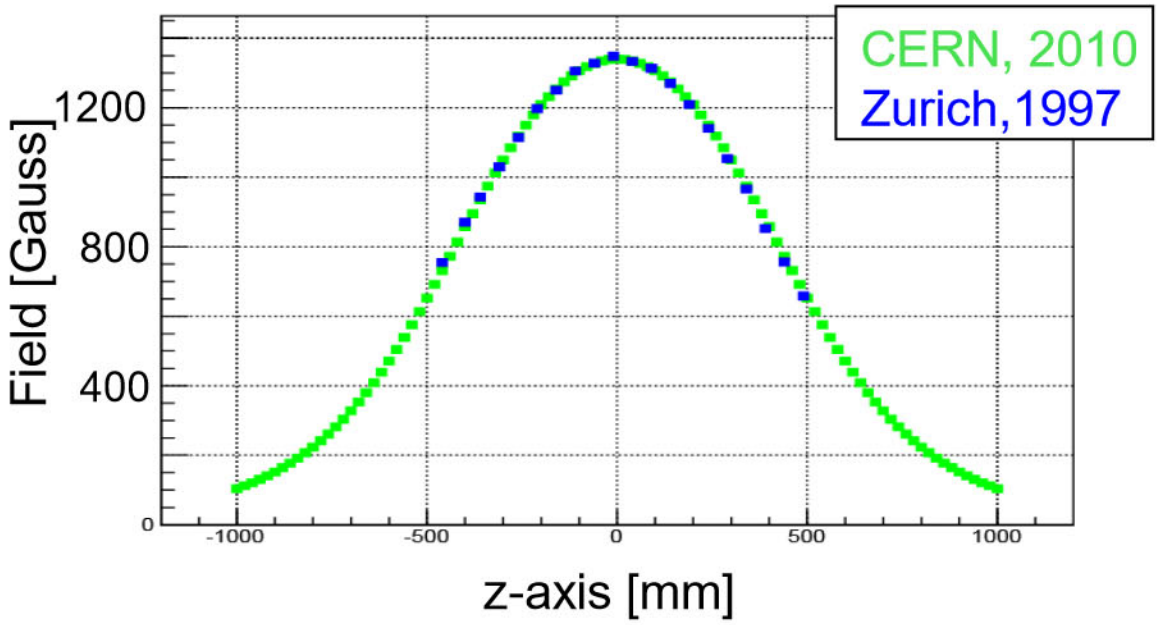

Figure 2-4: The AMS magnetic field intensity over the Z axis measured in 1997 and 2010. Z = 0 corresponds to the magnet center.

2.1.2 Transition Radiation Detector (TRD)

The Transition Radiation Detector (TRD) is placed on top of AMS. It is designed to distinguish $e^{\pm}$ from the overwhelming background of protons and measure nuclei charge using the Z^2 dependence of the ionization. The identification principle is based on the electromagnetic transition radiation (TR) emitted when a high speed charged particle traverses the boundary between two media with different dielectric constants, as illustrated in Figure 2-5.

The TRD (Figure 2-6) consists of 328 modules (Figure 2-7). These modules are arranged into 20 layers supported by a conical octagon made of aluminum-honeycomb walls with carbon-fibre skins and bulkheads. To provide 3D tracking capabilities, the lower and upper four layers are oriented parallel to the magnetic field while the

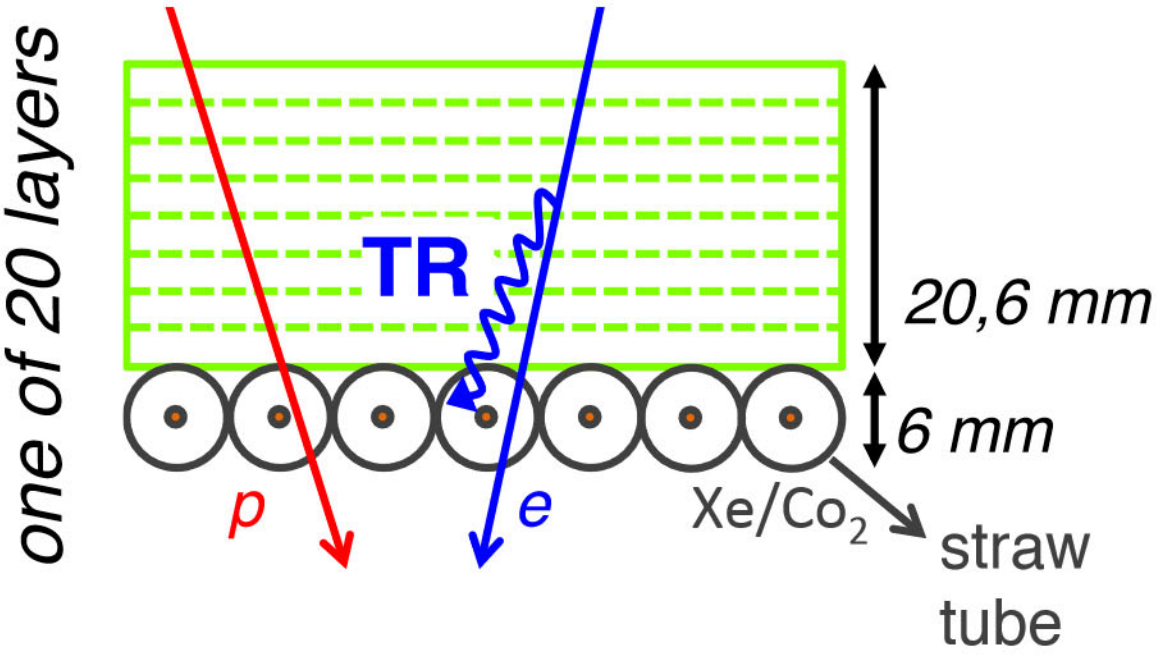

Figure 2-5: The TR X-rays produced by electrons in the fleece are efficiently absorbed in the straw tubes, producing a signal significantly larger than that from the ionization of protons.

middle 12 layers run perpendicular. Each module consists of 20 mm thick fleece radiators and 16 drift tubes, filled with a Xe:CO_2 (90%:10%) gas mixture working in the proportional mode.

Highly relativistic particles crossing the TRD may produce TR X-rays in the radiators. Such photons are efficiently absorbed and detected in the proportional chambers using Xe as the absorber. The quenching gas (CO_2) can absorb the photons without ionization and ensure stable operation. In order to differentiate between $e^{\pm}$ and protons, measurements of the energy deposit in the 20 layers are combined to calculate a TRD estimator based on the maximum likelihood estimation [67]. The electron/proton separation capabilities of the TRD are summarized in Figure 2-8.

Gas continuously diffuses out of the straw tubes. The average leak rate is 4.5 mbar/day. In order to operate the detector at stable parameters, the TRD is coupled to a gas supply system, shown in Figure 2-9. At launch, the onboard gas supply system was equipped with 49 kg Xe and 5 kg CO_2. It is composed of two supply boxes, a mixing vessel, and a circulation box. The latter is responsible for transferring the

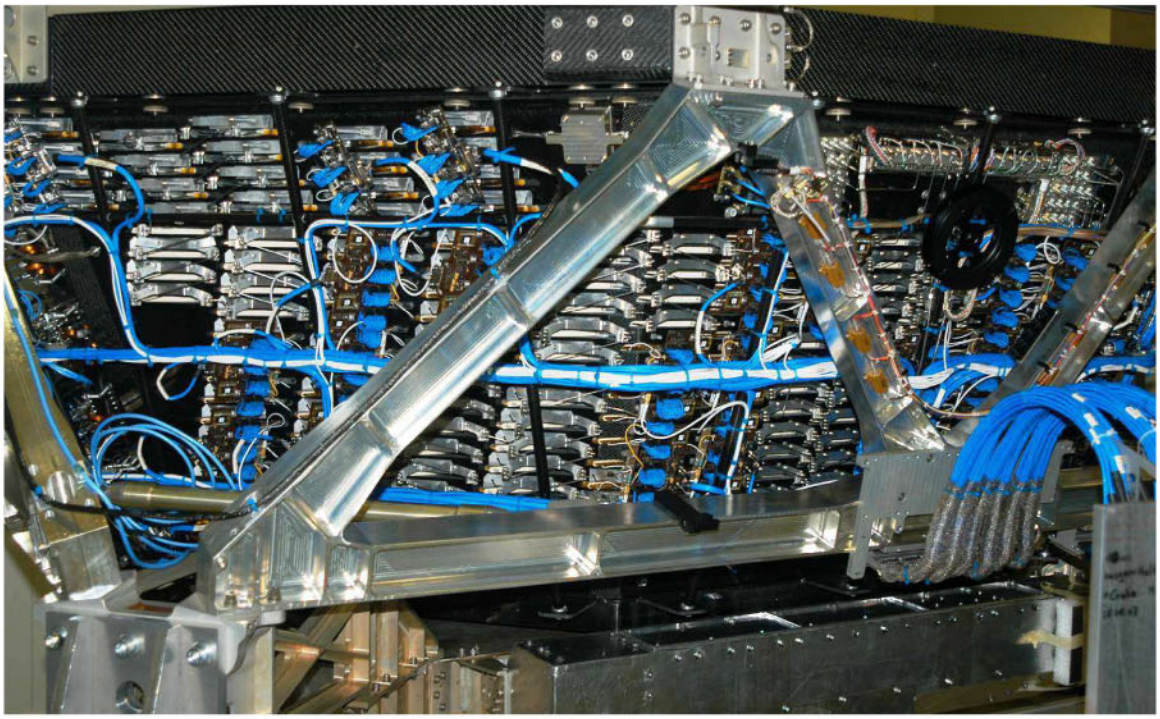

Figure 2-6: The Transition Radiation Detector.

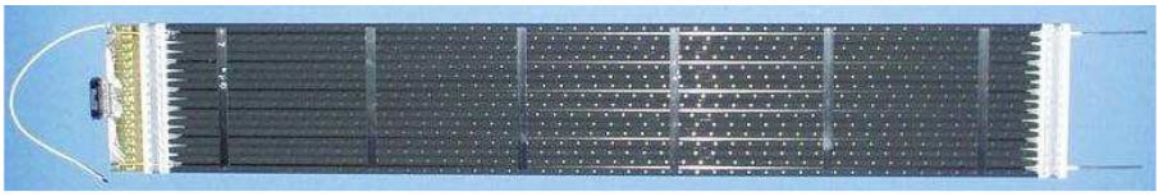

Figure 2-7: One of the 328 TRD modules.

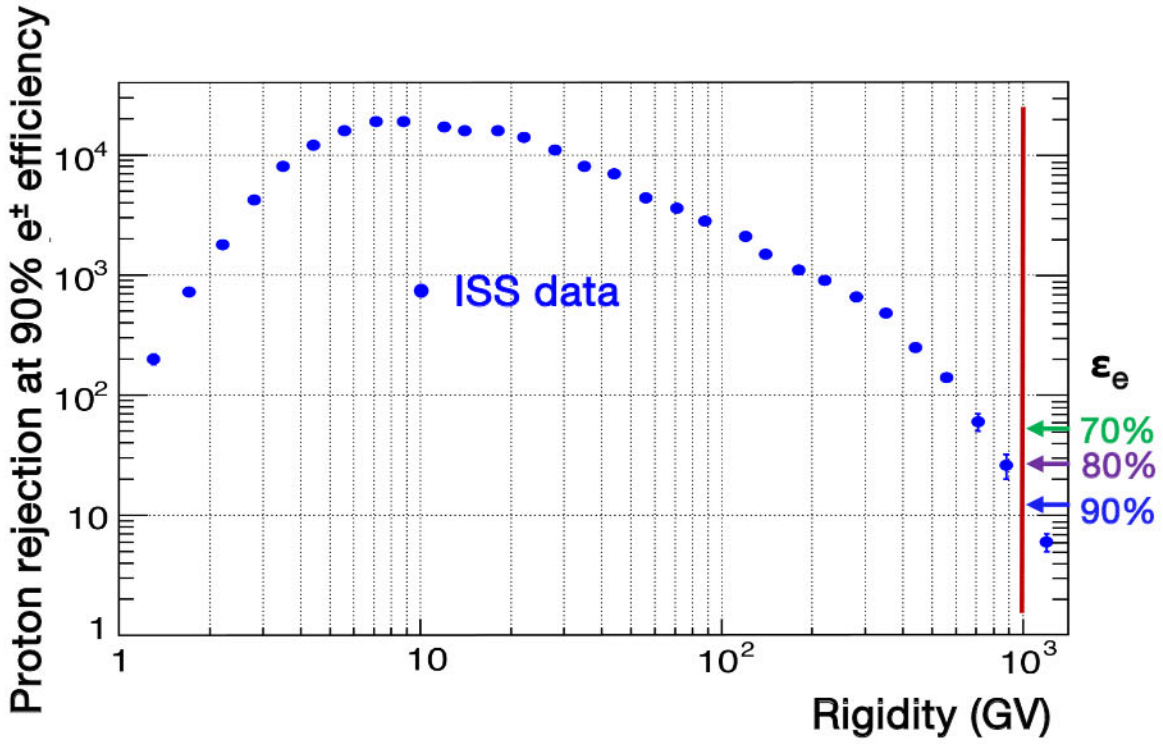

Figure 2-8: The TRD proton rejection power, defined as the number of protons which are rejected before a proton is misidentified as an electron or positron, as a function of rigidity at 90% selection efficiency for $e^{\pm}$. At 1 TV, the proton rejection factors at 70%, 80%, and 90% $e^{\pm}$ efficiency are indicated by the arrows.

mixed gas to the gas network system with the help of a pump. Monthly gas refills have been regularly performed since the start of the data acquisition in order to maintain an optimal gas composition for the detector performance. Moreover, daily HV adjustment is applied to correct the straw tubes' gas gain change due to the continuously changing gas composition [68].

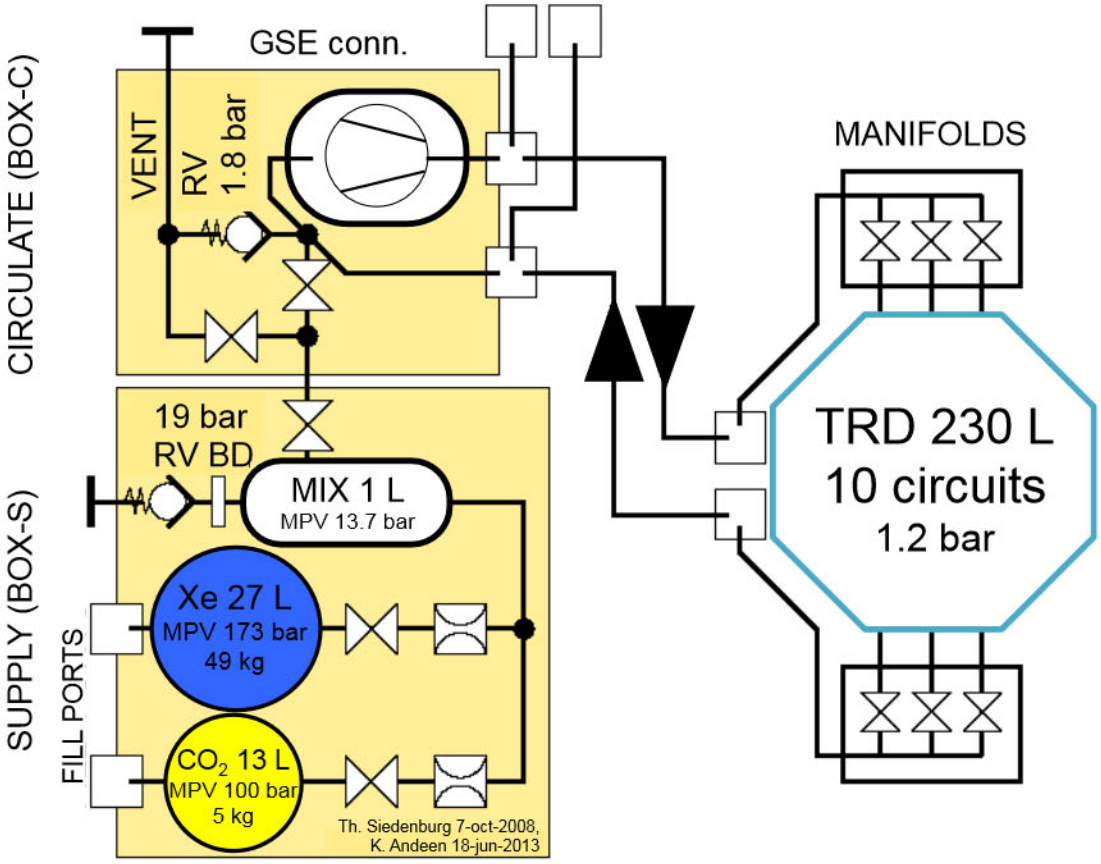

Figure 2-9: TRD Gas schematic (not to scale). Figure is from Ref. [68].

2.1.3 Time of Flight (TOF)

The Time of Flight (TOF) is composed by 4 planes of scintillation counters, 2 above (Upper TOF) and 2 below (Lower TOF) the magnet (Figure 2-10). The vertical distance between Upper TOF and Lower TOF is about 120 cm.

The four planes contain, from top to bottom, 8, 8, 10, and 8 scintillator paddles. Each counter (Figure 2-11) is made of a scintillator paddle, equipped with two or

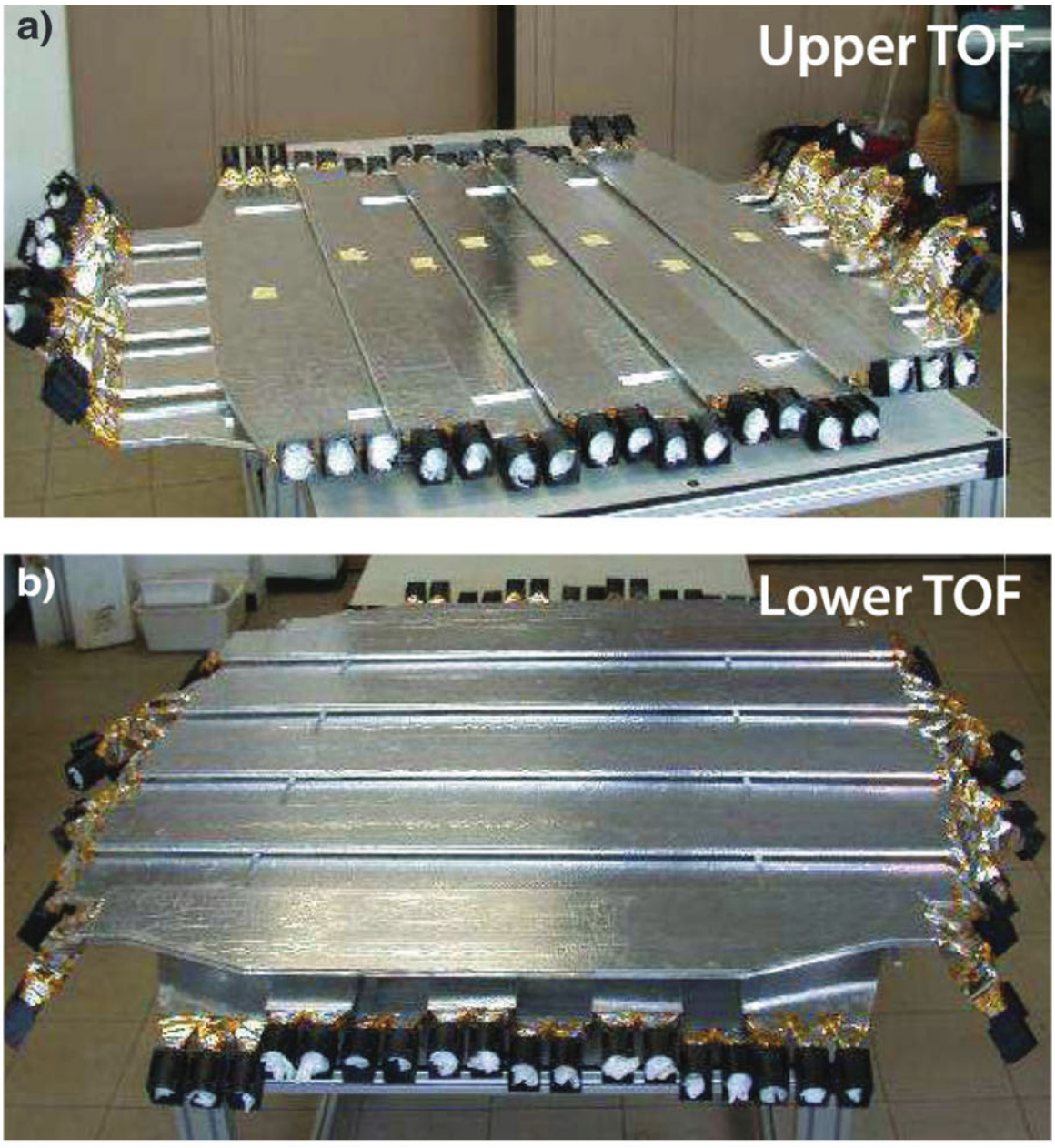

Figure 2-10: (a) The upper TOF plane. (b) The lower TOF plane. Figure is from Ref. [60].

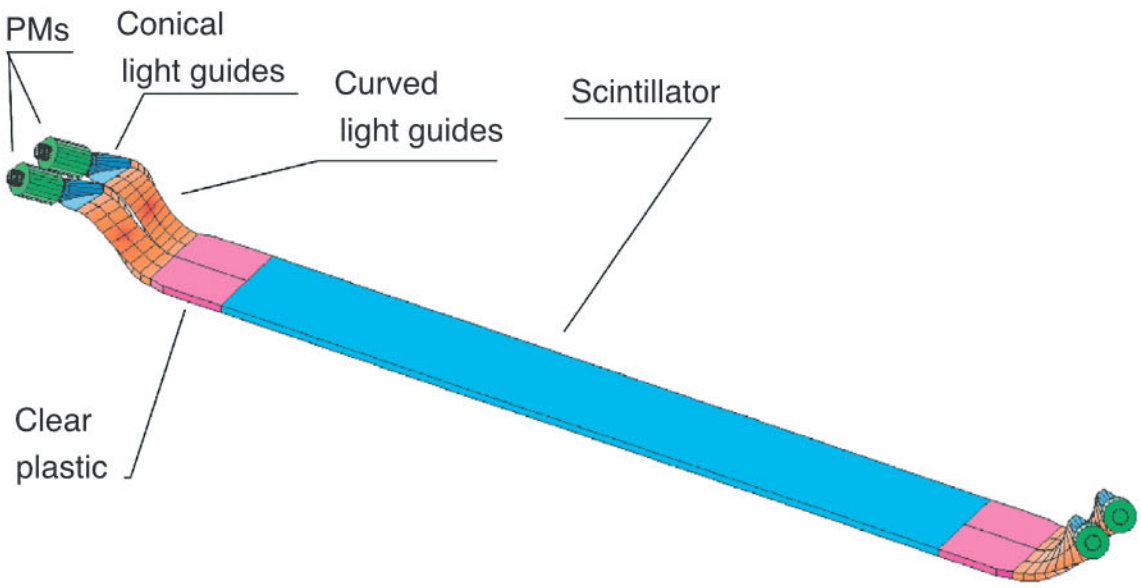

Figure 2-11: The design of a TOF counter. Figure is from Ref. [69].

three photomultiplier tubes (PMTs) through plexiglass light guides on each end for efficient detection of traversing particles. The internal paddles have a rectangular shape, 1 cm thick, 12 cm width, and 110-135 cm length, while the external counters have a trapezoidal shape with 18-26 cm width and 110 cm length. Tilted and bent light guides have been used to optimize the angle between the PMTs and the magnetic field [70].

The anode sum signals from each end of a counter are used to measure the total light released in the counter by the traversing charged particle, and to produce one digital signal for time measurement as well as two digital signals for trigger purposes. There are three thresholds for the anode signals: (1) the low threshold, set at ∼20% of the minimum ionizing proton (MIP) signal for time measurement; (2) the high threshold, set at ∼60% of the MIP signal for $Z = 1$ trigger; (3) the super high threshold, set at ∼400% of the MIP signal for $Z > 1$ trigger [71].

The particle velocity ($\beta = v/c$) is measured using the time of flight between the Upper TOF and Lower TOF. The velocity resolution is $\sigma(1/\beta) = 0.01$ for $Z \geq 3$ nuclei. The TOF is also capable of measuring the charge of cosmic rays up to $Z = 30$. The pulse heights of the two upper planes are combined to provide an independent measurement of the charge with an accuracy σ_Z/Z =2%. The two lower planes

are combined to provide another independent charge measurement with the same accuracy.

The charge resolution of a single TOF counter with respect to particle charge Z is shown in Figure 2-12.

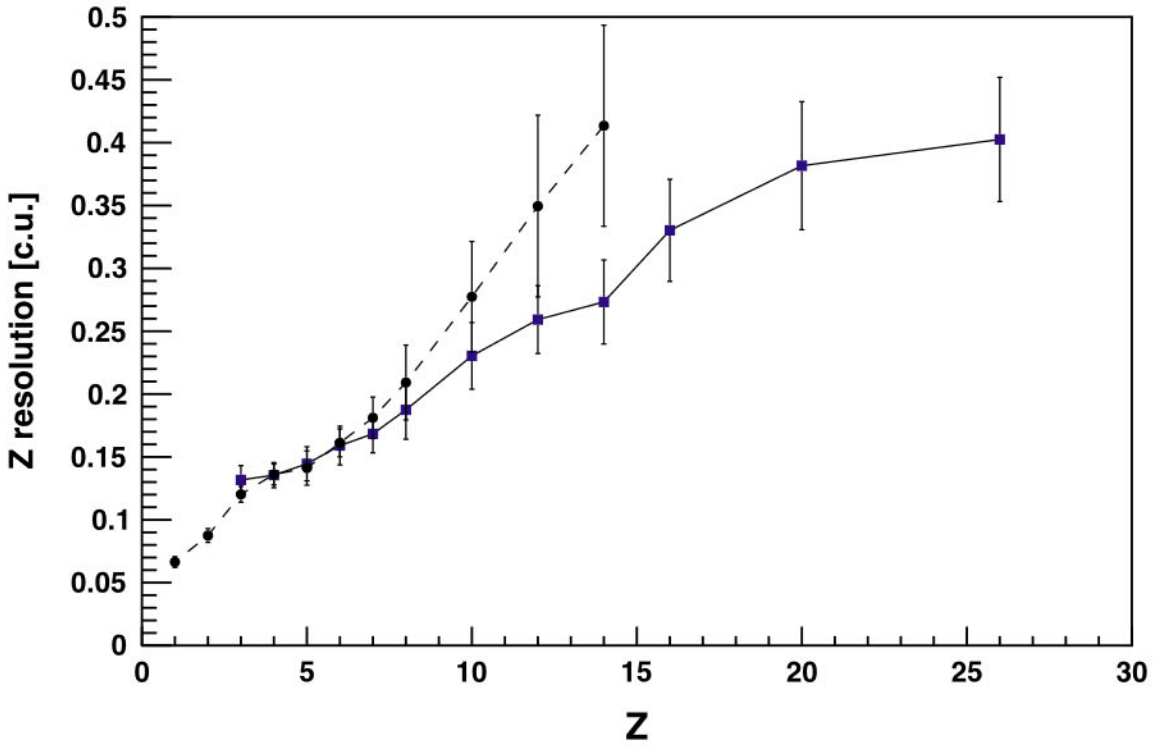

Figure 2-12: For the TOF, anode (dots, dashed line) and dynode (squares, solid line) charge resolution in charge units (c.u.) as a function of Z; the error bars represent the standard deviation of the distribution of resolution for all TOF counters. Figure is from Ref. [69].

2.1.4 Silicon Tracker

The silicon tracker contains 2264 double-sided silicon microstrip sensors. These sensors, each with an area of 72×40 mm^2 and thickness of 300 μm, are grouped together to form independent mechanical and functional units (ladders). The number of sensors in one ladder varies between 7 and 15. The different ladder lengths ($37-62$ cm) are required to match the cylindrical shape of the magnet.

192 ladders are arranged in nine layers. As shown in Figure 2-13, the inner tracker, composed of seven layers (L2-L8), is placed inside the magnet bore on four support

planes, while two external layers are installed on both sides of the detector, one (L1) above the TRD, the other (L9) between RICH and ECAL. The level arm from L1 to L9 is about 3 m.

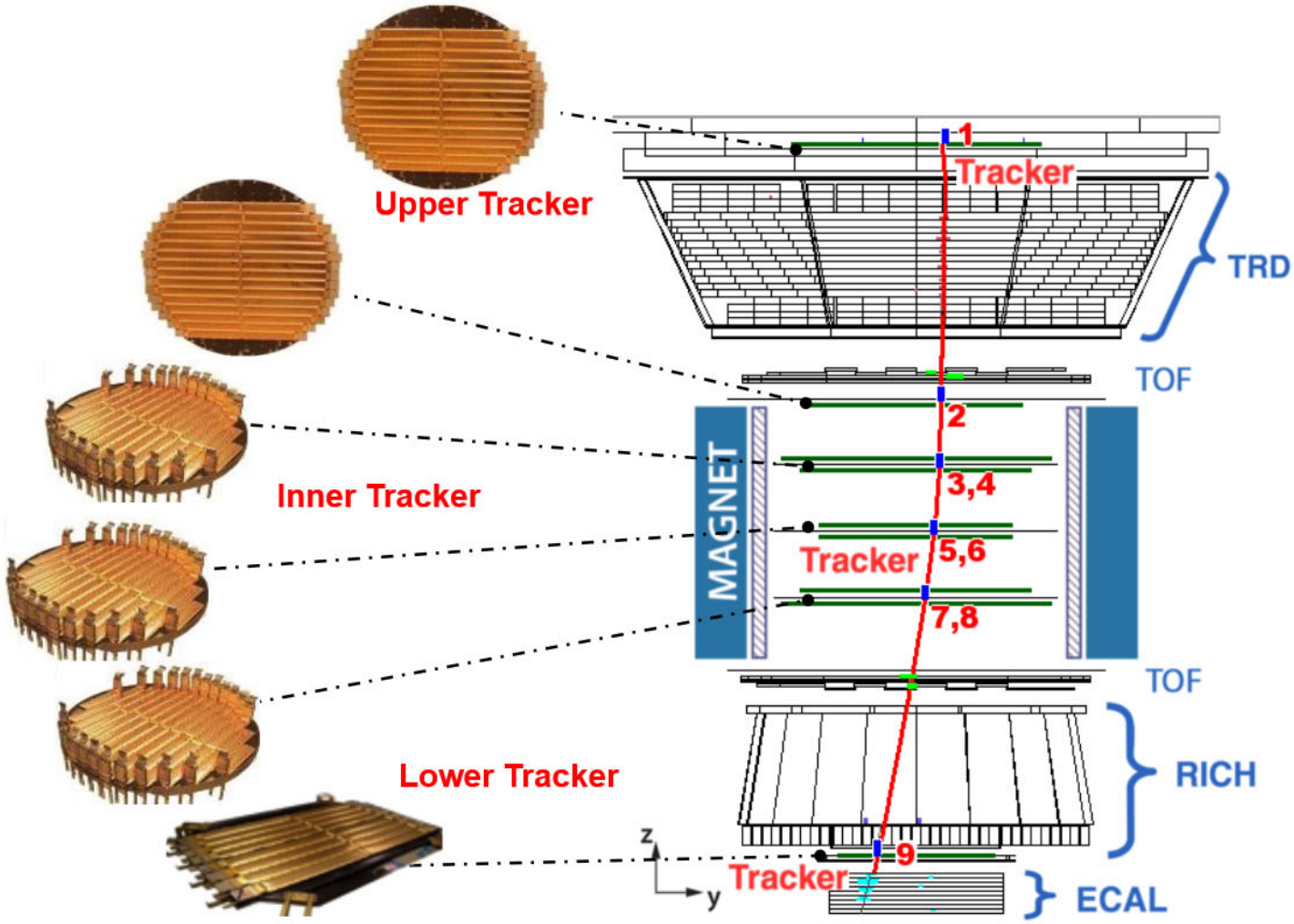

Figure 2-13: Schematic view of the AMS silicon tracker with a charged particle traversing the detector, presented in the bending (Y-Z) plane of the magnetic field. Figure is from Ref. [72].

The ladder is the minimum readout unit of the tracker. The bending and non-bending side strips are separately connected in daisy chains or via an Upilex cable to the ladder end and connected to a hybrid which provides bias voltage and contains front-end readout chips [73]. Each ladder is readout by 16 low noise high dynamic range readout chips (64 channels each). Thus each ladder has a total of 1024 readout channels, 640 on the bending side and 384 on the non-bending side.

The analog signals are transmitted to the tracker data reduction board (TDR) for

calibration and data reduction. The calibration results, including strip pedestal and noise values, are then used to find signals, combined with clusterization algorithms. A threshold is applied to the signal-to-noise ratio (SN) for each readout strip (after pedestal and common noise subtraction). A strip with SN above a value SN_{seed} is considered as a seed for a potential cluster. Neighbouring strips are added to the cluster if their SN exceeds $SN_{neighbour}$. The detailed values are discussed in Ref. [73]. The set of clusters is the basis for reconstructing the associated particle track in the detector.

In order to reconstruct a particle track, the hits on the tracker layers have to be reconstructed and distinguished from noise hits. The first step consists of using raw data (clusters) to get the geometrical coordinates of the signal. Then the coordinates are combined to obtain a three-dimensional hit. The track-finding algorithm [74] was developed to scan all these hits and provide track quality estimation to identify any combinations of hits that are compatible with a track, then the combination of the hits to the track candidates with the best track quality is selected. Track candidates are accepted if the track contains at least four three-dimensional hits located in 3 out of 4 inner supporting planes of L2, L3-4, L5-6, L7-8. If the track extrapolation to the external layers falls close enough to a reconstructed hit, the track is extended to include this hit.

Accurate knowledge of the sensor and ladder geometries, to the level of a few μm, is necessary to optimize the tracker performances in terms of the rigidity resolution. To obtain a few microns precision, two types of tracker alignment are introduced. First, static alignment of all the sensors has been done both on ground using proton test beam at the CERN SPS and in space using cosmic ray events to correct for residual shifts after the launch. Then a dynamic alignment procedure is done in space, for L1 and L9, to account for the thermal deformation of the AMS support structures [75]. However, small systematic shifts may still be present after these three steps. This could lead to a shift of inner tracker rigidity scale, and consequently to a potential rigidity scale shift of the full tracker. The in-flight rigidity scale shift of the AMS tracker was measured by comparing the tracker measured $1/R$ distributions

from cosmic electron and positron events with the same ECAL measured energy [76].

The tracker accurately determines the trajectory of cosmic rays by multiple measurements of the coordinates with a resolution in each layer of 8 μm for fluorine nuclei, 6 μm for sodium nuclei, and 7 μm for aluminum nuclei in the bending (Y) direction. Together, the tracker and the magnet measure the rigidity R of charged cosmic rays, with a maximum detectable rigidity (MDR) of 2.9 TV for fluorine nuclei, 3.3 TV for sodium nuclei, and 3 TV for aluminum nuclei over the 3 m lever arm from L1 to L9. Each layer of the tracker provides an independent measurement of the charge Z using the Z^2 dependence of the ionization, with an estimated resolution of σ_Z/Z= 3.0% for fluorine nuclei and σ_Z/Z= 2.9% for sodium and aluminum nuclei. Overall, the inner tracker has a resolution of σ_Z/Z= 1.3% for fluorine nuclei and σ_Z/Z= 1.1% for sodium and aluminum nuclei.

Figure 2-14 summarizes the tracker charge resolution for $1 \leq Z \leq 28$ particles.

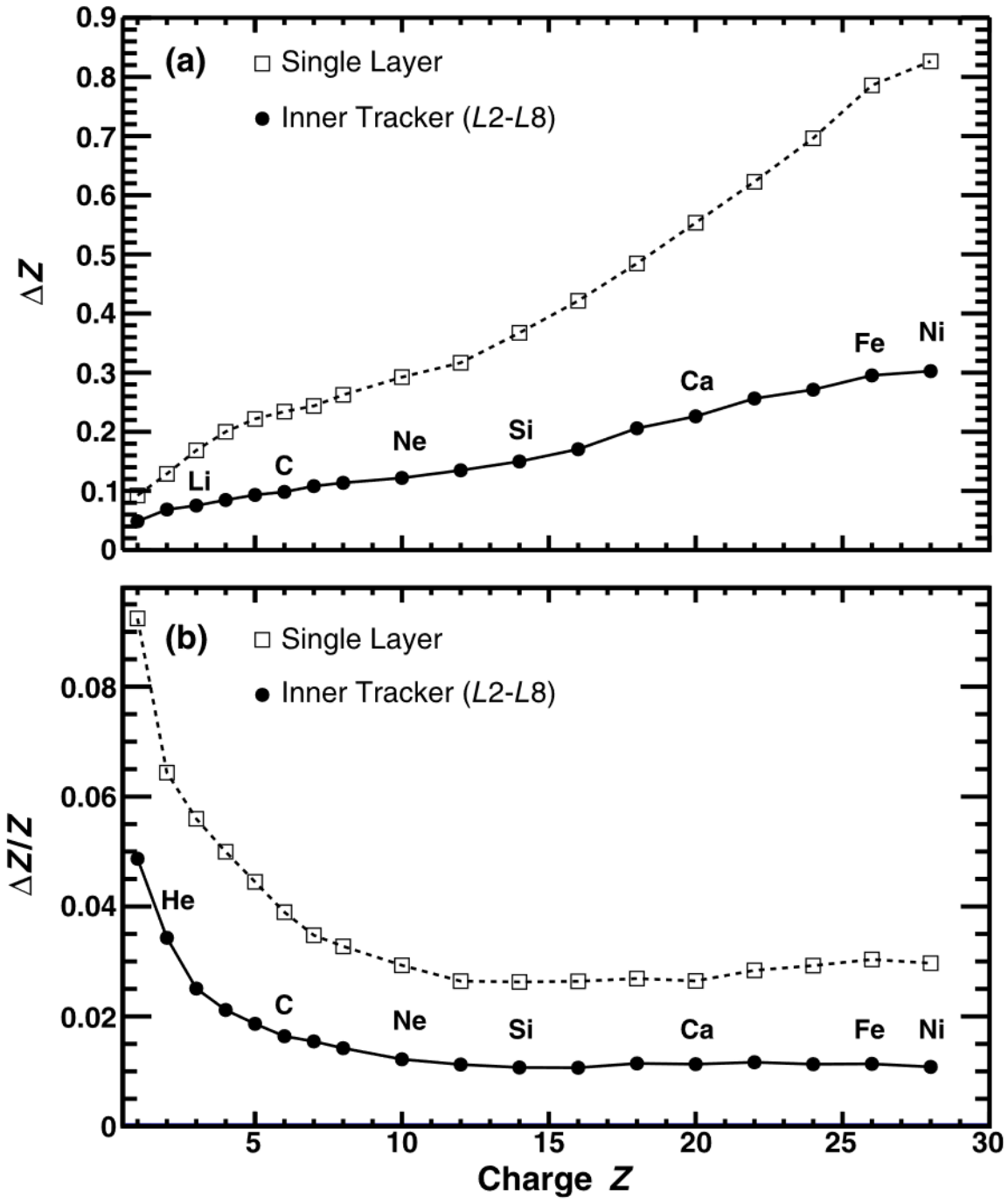

Figure 2-14: (a) Charge resolution ΔZ and (b) $\Delta Z/Z$ of the inner tracker (circles) and a single layer (squares) as functions of nuclei charge Z with $R > 7$ GV. Figure is from Ref. [77].

2.1.5 Anti-Coincidence Counter(ACC)

The best analyzing power is reached for particles traversing the detector from top to bottom, with redundant measurements of the particle properties along the trajectory. To achieve this, it is important to identify and reject the particles entering the detector sideways. Such particles do not contribute to physical measurements but can cause spurious triggers by interacting with the detector material. Figure 2-15 illustrates different situations where events are accepted and rejected based on the ACC information.

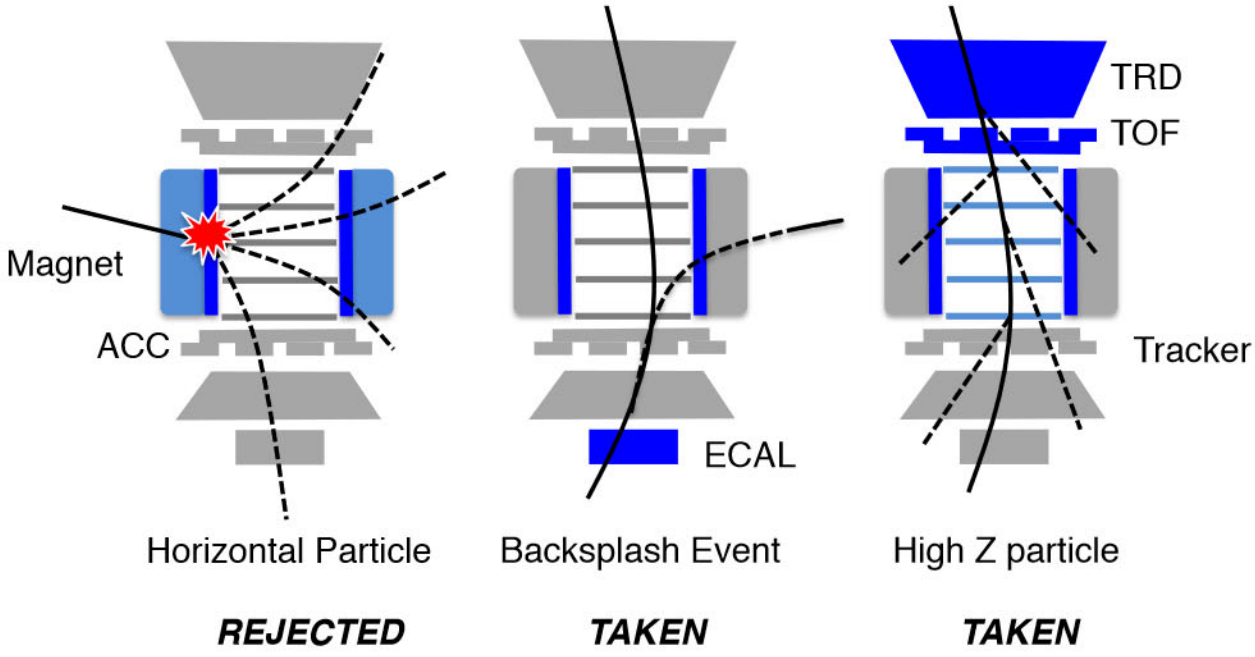

Figure 2-15: Illustration of the ACC working principle for particles with $Z > 1$. Left: A particle entering the detector sideways may give a signal on ACC and not in TOF. These kinds of events are rejected. Center: when a high-Z particle traverses matter, it is accompanied by electron production. These electrons can easily fire the ACC. In order to keep these events, the ACC veto is disabled. Right: when an electron or positron passes through the ECAL, backsplash particles are produced. These particles may exit from the calorimeter surface and hit the ACC. In this case, the trigger condition should be TOF and not more than 4 ACC paddles fired. Figure is from Ref. [78].

The ACC is made of 16 scintillating paddles arranged on a cylinder inserted into the inner bore of the magnet (Figure 2-16). The light coming from the scintillating panels is collected with wavelength-shifting fibres (WLS) of 1 mm diameter, then is

guided (LG) to 16 PMTs, 8 on top of the magnet bore and 8 at the bottom. The very high efficiency and the high degree of homogeneity of the scintillating fibers will ensure a reliable and fast ACC veto trigger signal for the high inclination particles [79]. The ACC information is mainly used in different trigger decisions (see Section 2.2).

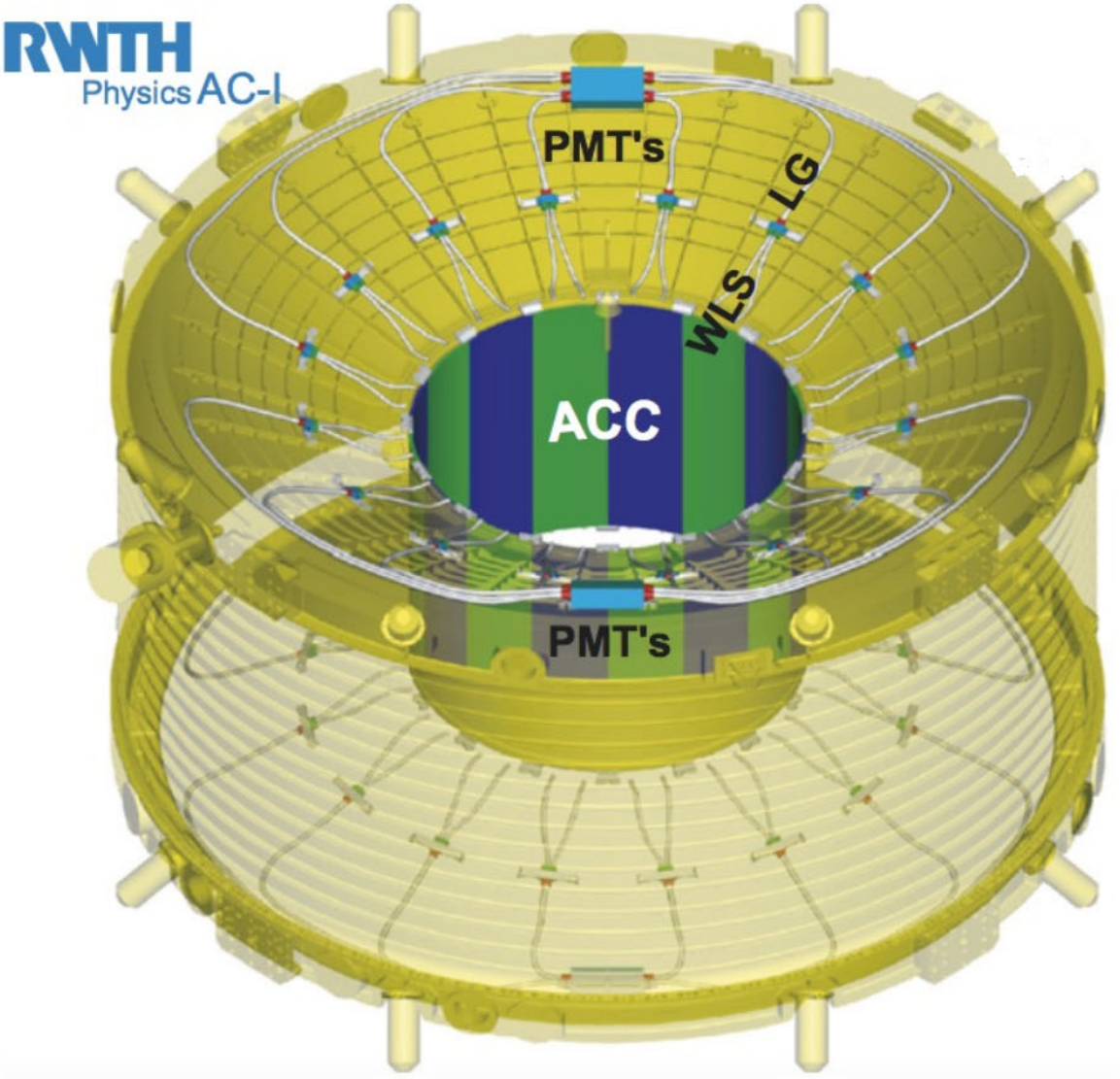

Figure 2-16: AMS ACC mounted inside the magnet.

2.1.6 Ring Imaging Cherenkov Detector (RICH)

The AMS Ring Imaging Cherenkov detector (RICH) is placed below the lower TOF plane. The RICH detector measures the velocity and charge of a passing particle.

The detection principle is based on the Cherenkov electromagnetic emission produced by a charged particle with velocity larger than the phase velocity of light in the material. A cone of light is emitted along the particle trajectory. The opening angle of this cone θ is related to the particle velocity β through $\beta = \frac{1}{n \times \cos\theta}$, where n is the refractive index of the material. The RICH also provides an independent measurement of the particle charge. For a particle of charge Ze, the number of radiated photons produced per unit path length and per unit energy interval of the photons is given by $d^2N/dEdx = \alpha Z^2 \sin^2\theta/\hbar c$ [6], where α is the fine-structure constant.

The RICH detector consists of a radiator plane, a conical reflector, and a photon-detection plane (Figure 2-17). The radiator consists of an array of 2.7 cm thick aerogel tiles with a refractive index of 1.05, which surrounds a central 35×35 cm^2 region equipped with 5 mm thick sodium fluoride (NaF) radiator ($n_{\mathrm{NaF}} = 1.335$). This combination optimizes the overall detector acceptance (0.4 m^{2}sr) since the Cherenkov photons radiated by the NaF in large cones will fall within the detection area. The detector plane has an empty 64×64 cm^2 area in its center, matching the active area of the electromagnetic calorimeter located below. Outside the ECAL hole, 680 sixteen-pixel PMTs are arranged to cover the circular 134 cm diameter surface at the base of the conical mirror. The radiator and the detection plane are enclosed in the volume of a conical reflector, which provides the necessary photon ring expansion. The reflector increases the RICH acceptance reflecting high inclination photons.

Figure 2-18 summarizes the velocity resolution of the RICH as a function of the particle charge Z. The velocity resolution for $|Z| > 1$ is better than 0.1% at $\beta \sim 1$. Figure 2-19 shows the charge resolution $\Delta Z/Z$ for $1 \leq Z \leq 8$ particles.

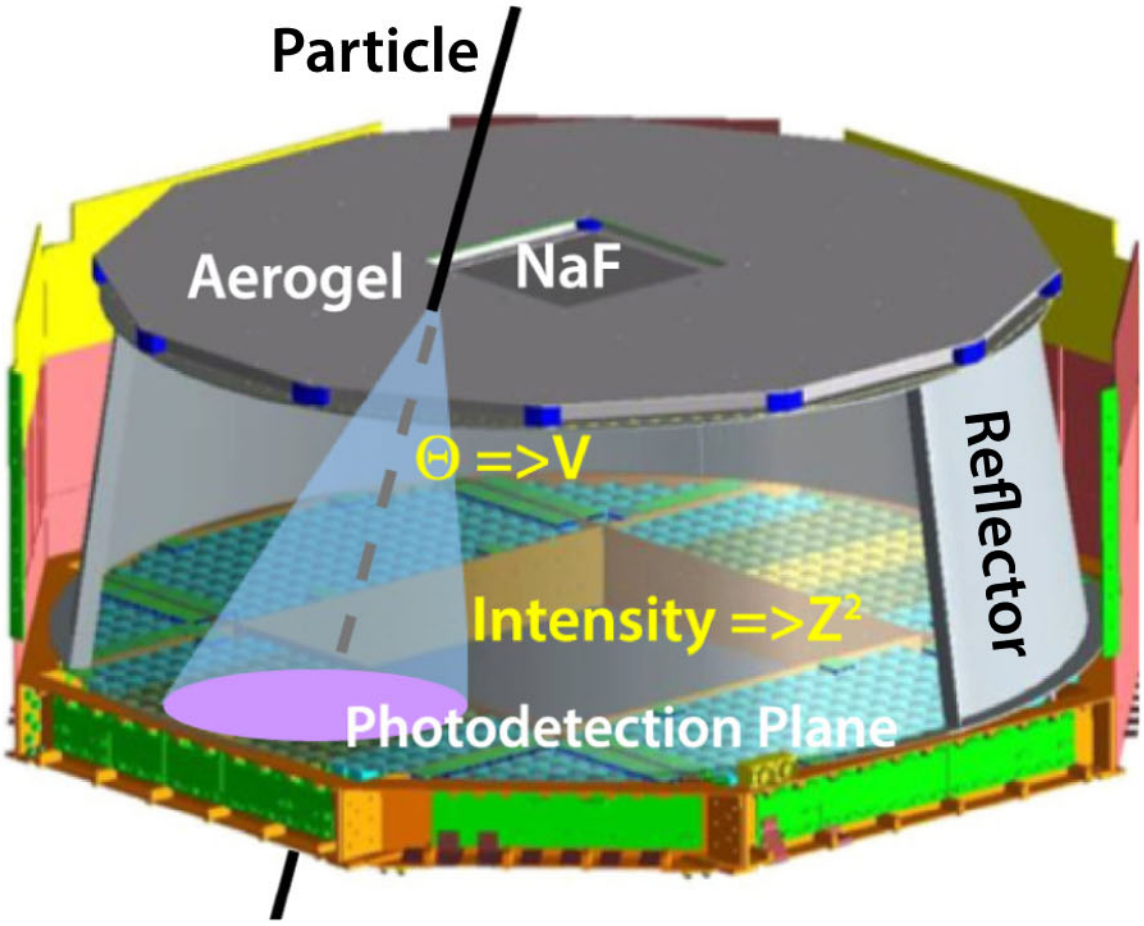

Figure 2-17: Schematic of the RICH. It is composed by three parts: the radiator layer, the expansion volume with conical reflector, and the photon-detection plane.

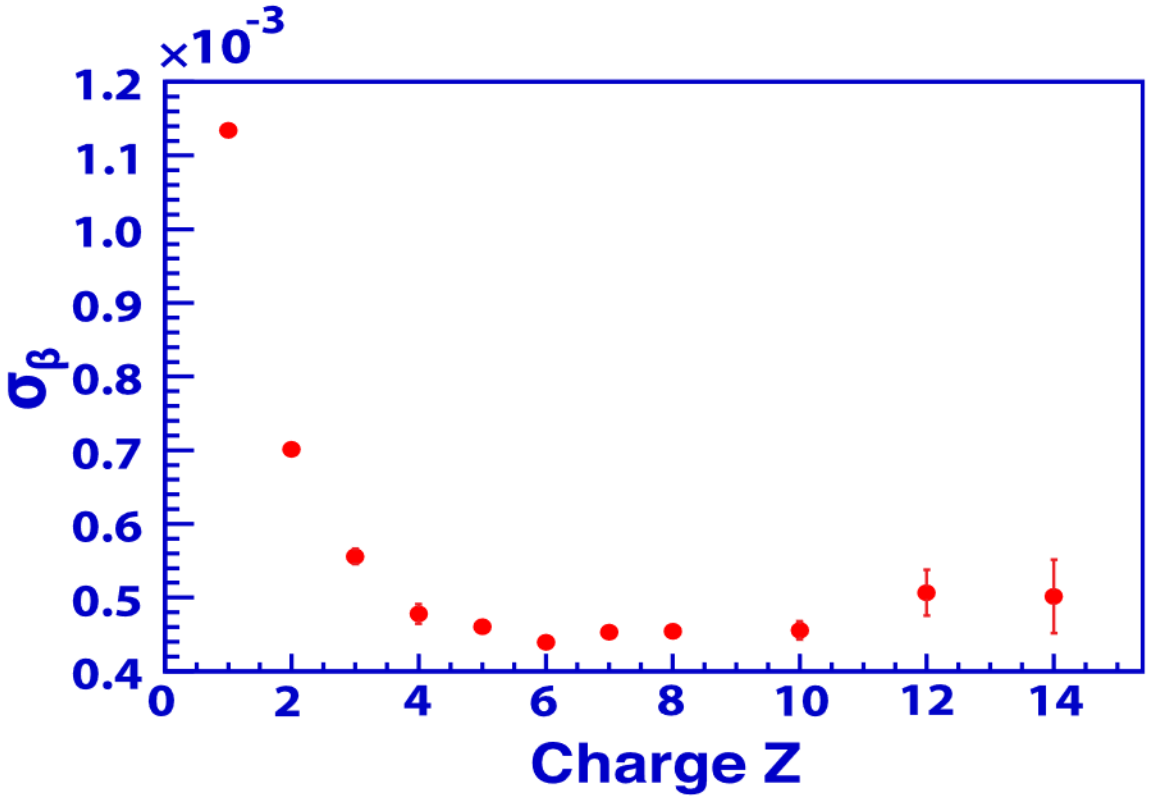

Figure 2-18: RICH velocity resolution as a function of charge Z for the aerogel radiator. Figure is from Ref. [60].

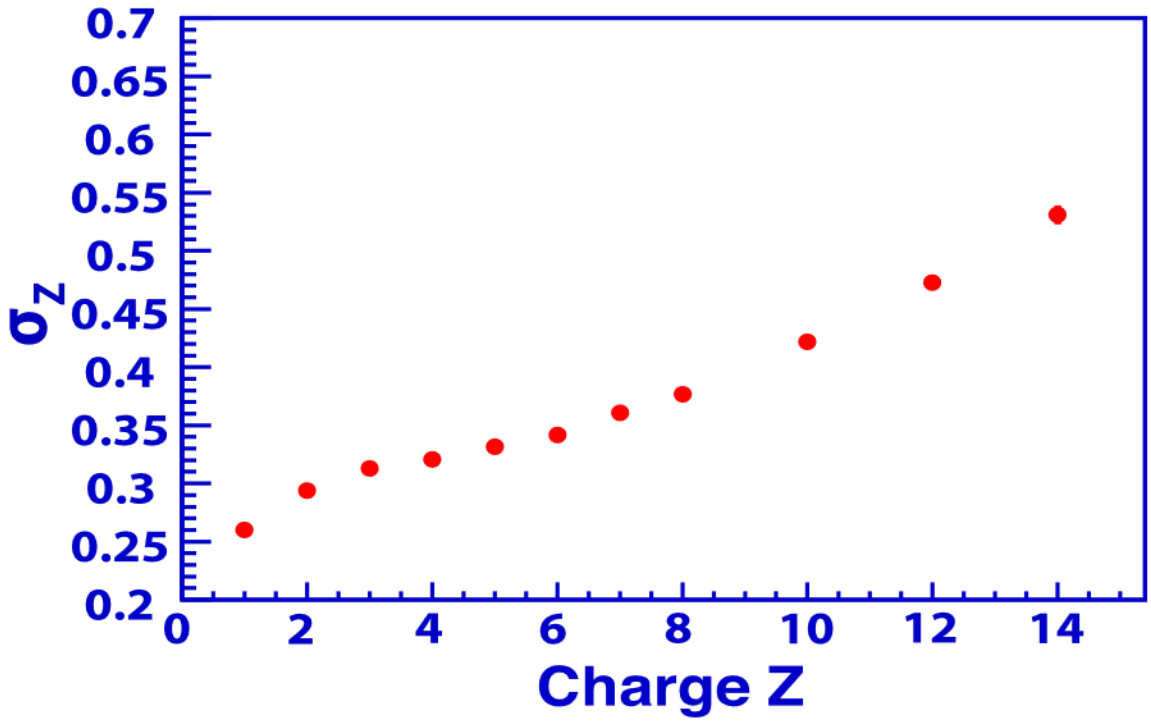

Figure 2-19: RICH charge resolution as a function of charge Z for the aerogel radiator. Figure is from Ref. [60].

2.1.7 Electromagnetic Calorimeter (ECAL)

The Electromagnetic Calorimeter (ECAL) provides a precise 3-dimensional reconstruction of the shower profile and the electromagnetic shower energy. It separates $e^{\pm}$ from protons independently from the TRD based on the different characteristic profiles of electromagnetic and hadronic showers.

The ECAL is a lead-scintillating fibre sampling calorimeter with 17 radiation length (X_0). It is formed by a stack of 9 super-layers (SL) consisting of 11 grooved 1 mm lead foils interleaved by 1 mm plastic scintillating fibres, for a total active dimensions of 648×648×167 mm^3. The SLs are arranged along the Z-axis. Each SL is 18.5 mm thick and corresponds to 1.9 X_0. In each SL, the fibres run in one direction only. The 3D imaging capability of the ECAL is obtained by stacking SL with fibres oriented in alternating directions (five SLs with fibres parallel to the X-axis and four parallel to the Y-axis). The fibres are read out on one end by 1296 photosensors (324 PMTs each with 4 anodes). The assembled ECAL is shown in Figure 2-20.

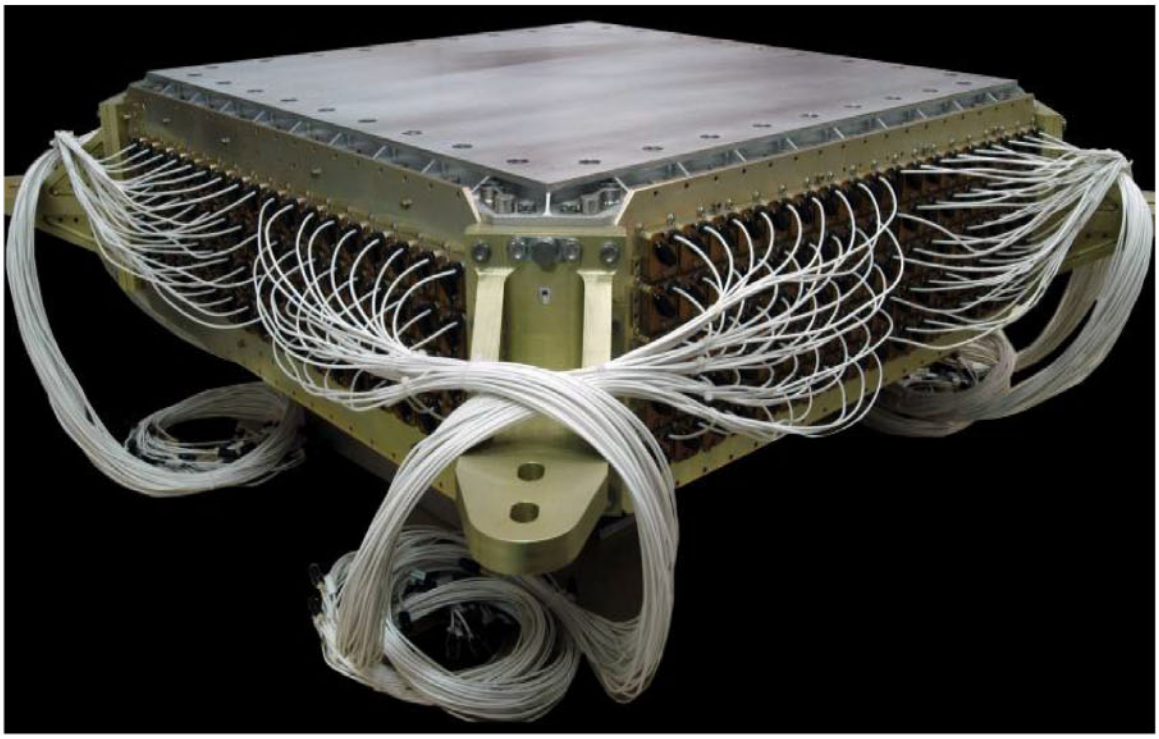

Figure 2-20: A photo of the completed ECAL before installation in AMS.

The energy of the incoming particle is measured by applying corrections for the rear and lateral energy leakages, and for the anode inefficiency, to the deposited energy. These corrections ensure an accurate measurement of the incoming energy E of $e^{\pm}$. From the beam tests of the complete AMS detector, the energy resolution of the ECAL has been measured and parameterized as a function of energy E (in GeV) [80], $\frac{\sigma(E)}{E} = \sqrt{\frac{0.104^2}{E} + 0.014^2}$.

Furthermore, a multivariate classifier, based on a boosted decision trees algorithm (BDT) [81], is constructed by using the 3D shower shape in the ECAL. This is used to further differentiate between $e^{\pm}$ and protons independently from the TRD. The ECAL proton rejection capability is shown in Figure 2-21.

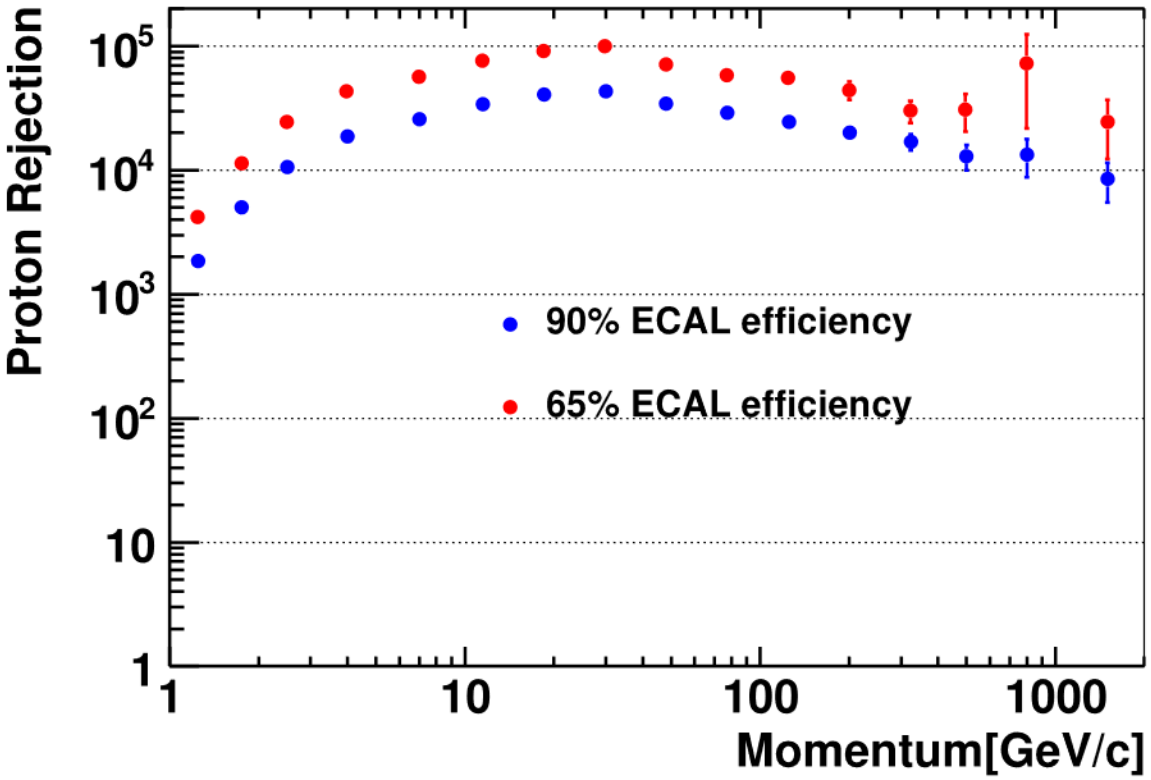

Figure 2-21: Comparison of the measured proton rejection for 90% (blue data points) and 65% (red data points) $e^{\pm}$ selection efficiencies. The tighter cut further reduces the proton background by a factor of ~ 3. This is independent of the rejection power of the TRD shown in Figure 2-8. Figure is from Ref. [60].

2.2 Trigger and Monte Carlo Simulation

The AMS trigger is generated by the signals coming from the TOF, ACC, and ECAL [71] [82].

Six sub-triggers (five physics triggers and one unbiased trigger) were designed and implemented for data taking aboard the ISS:

1. single charged: 4 out of 4 TOF layers above the high threshold (defined in Section 2.1.3), in coincidence with an absence of signals from the ACC;

2. normal ions: 4 out of 4 TOF layers above the super high threshold, in coincidence with less than 5 hits from the ACC;

3. unbiased charged: 3 out of the 4 TOF layers above the high threshold, pre-scaled by a factor of 100;

4. slow ions: similar to normal ions, but with an extended gate width to latch the signals, as a dedicated trigger to detect potential strangelets;

5. electrons and positrons: 4 out of 4 TOF planes above the high threshold in coincidence with both X and Y projections of ECAL energy deposition above threshold;

6. photons: both X and Y projections of ECAL energy deposition above the threshold and the ECAL shower angle inside the detector geometrical acceptance;

The unbiased trigger is 100% efficient for particles with $Z > 1$, so it is used to evaluate trigger efficiencies in data analysis. Detailed studies for the trigger efficiencies will be presented in Section 3.6.

The AMS Monte Carlo (MC) simulation contains a detailed description of the detector: its geometry and composition, with the best possible estimates of the matter density distribution of both active and passive areas in the instrument. The MC simulation also describes the physical processes that take place inside the detector when a particle passes through.

MC simulated events are produced using a dedicated program developed by the collaboration based on the GEANT4-10.3 package [83]. The program simulates electromagnetic and hadronic [84] interactions of particles in the material of AMS and generates detector responses. The digitization of the signals are simulated precisely according to the measured characteristics of the electronics. The simulated events then undergo the same reconstruction as used for the data. The simulated events have the same data structure as the data, with the additional information from the MC generation parameters: the particle type, generated rigidity, etc.

Chapter 3

Measurements of the Fluorine, Sodium, and Aluminum Fluxes

As discussed in Section 1.1.1, the fundamental measurement in cosmic rays is the flux, defined as the number of particles of a given species per unit of time, area, solid angle, and energy or, for AMS, rigidity.

The isotropic flux Φ_i in the rigidity bin $(R_i, R_i + \Delta R_i)$ is obtained from:

$$\Phi_i = \frac{N_i}{A_i \varepsilon_i T_i \Delta R_i} \ [\mathrm{m}^{-2}\mathrm{s}^{-1}\mathrm{sr}^{-1}\mathrm{GV}^{-1}] \tag{3.1}$$

where N_i is the number of events collected by AMS after background subtraction and bin-to-bin migration correction; A_i is the effective acceptance (detector geometrical factor multiplied by particle survival probability when interacting with the AMS detector materials and by efficiencies from the detection, reconstruction and selection) estimated from Monte Carlo simulation, and corrected for the small differences between the data and simulation; ε_i is the trigger efficiency; T_i is the exposure time (data collection time) in seconds, and ΔR_i is the rigidity bin width chosen according to the rigidity resolution and available statistics. Each factor of this equation will be discussed in detail in this chapter.

3.1 Exposure time

The exposure time is the effective amount of time that the detector was not busy with the electronics readout and consequently ready to start data acquisition and trigger on an incoming event. This is affected by the detector's live time and the requirement of particle rigidity above the geomagnetic cutoff. For example, when the ISS passes the South Atlantic Anomaly (SAA) region, the data acquisition of the AMS detector saturates due to the high particle rates. Furthermore, the Earth's magnetic field will prevent the low-rigidity cosmic rays from reaching AMS, introducing a rigidity dependence of the exposure time.

The exposure time is calculated on a second-by-second basis using the Run Time Information (RTI) database in the AMS Offline Software, which stores the orbital and relevant DAQ information for each second of AMS data collection time on the ISS. A set of standard selection criteria has been studied by the AMS collaboration to retain only those seconds when AMS could measure the flux accurately:

- Good RTI information:

1) the ratio of the number of triggered events (N_{trig}) to the number of reconstructed events (N_{evt}) greater than 0.98 ($N_{trig}/N_{evt} > 0.98$);

2) the data acquisition live time greater than 0.5;

3) the AMS z-axis pointing within 40° of the local zenith;

4) the ratio of the number of absent events (N_{err}) over N_{evt} less than 0.1 ($N_{err}/N_{evt} < 0.1$);

- Remove seconds in the SAA region.
- Remove bad runs with known off-nominal condition.

Then the exposure time is accumulated for each rigidity bin when the lower edge is greater than a factor of 1.2 times the maximum geomagnetic cutoff within the AMS field of view to account for the suppression of exposure time to galactic cosmic rays due to the Earth's magnetic field. The geomagnetic cutoff is calculated by back-tracing [85] particles from the top of AMS out to 50 Earth's radii using the most recent International Geomagnetic Reference Field [86, 87] model.

The rigidity dependence of the exposure time in the first 8.5 years is shown in Figure 3-1. Because of the influence of the geomagnetic field, the exposure time for galactic cosmic rays increases with rigidity and becomes constant at 1.97×10^8 s above 30 GV.

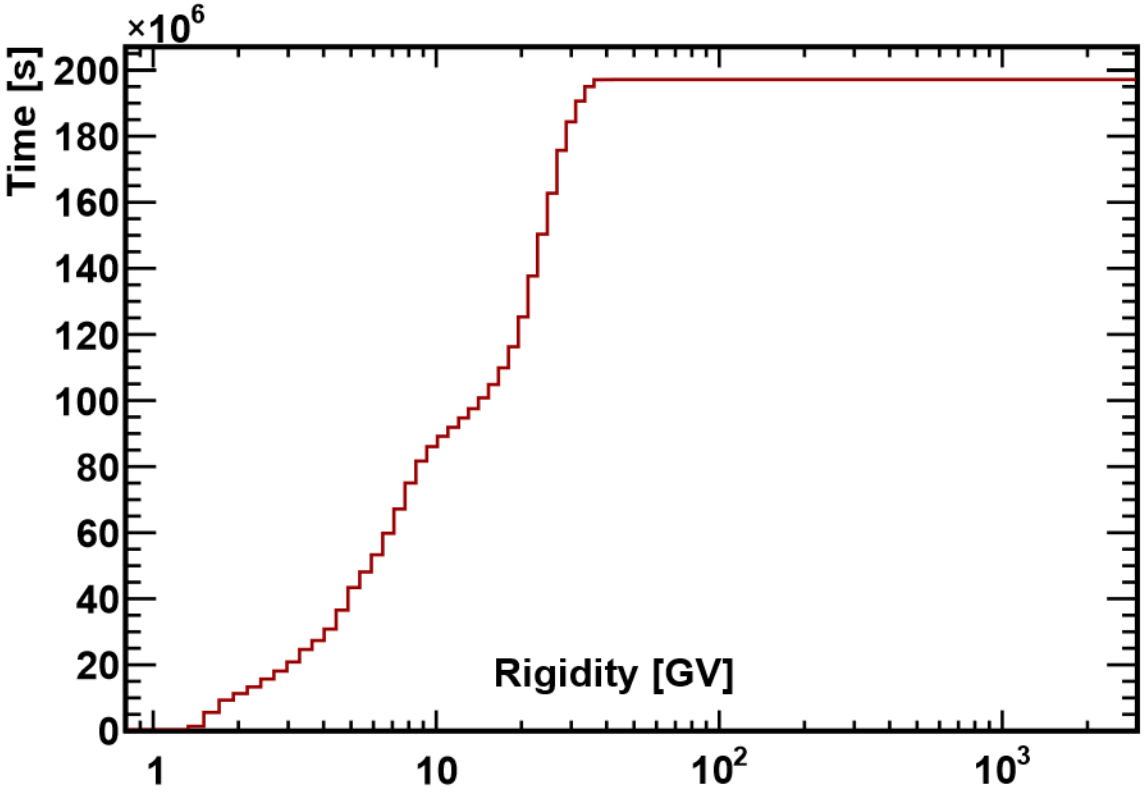

Figure 3-1: The AMS exposure time as a function of rigidity using data from the beginning of operation in May 2011 until Oct 2019.

3.2 Event Selection

In the first 8.5 years, AMS has collected 1.50×10^{11} cosmic ray events. Only events collected during nominal operating conditions (i.e., passed the selection criteria in Section 3.1) are used in the flux measurements. Fluorine, sodium, and aluminum events are required to be downward going and to have a reconstructed track in the inner tracker which passes through L1. In the highest rigidity region, $R \geq 1.2$ TV, the track is also required to pass through L9. Track fitting quality criteria such as

a χ^2/d.o.f. < 10 in the bending coordinate are applied. Charge measurements on L1, the inner tracker, the upper TOF, the lower TOF, and, for $R \geq 1.2$ TV, L9 are required to be compatible with charge $Z = 9$ for fluorine, $Z = 11$ for sodium, and $Z = 13$ for aluminum. The measured rigidity is required to be greater than a factor of 1.2 times the maximum geomagnetic cutoff within the AMS field of view. The detailed event selection is summarized below:

1. Inner Tracker (L2 to L8)

   (a) at least five hits in the Y coordinate, and, in addition, among these five hits, there is at least one hit on L2 and on each of the three inner tracker planes, which is denoted as L2&(L3|L4)&(L5|L6)&(L7|L8);

   (b) the normalized χ^2 of the inner tracker track fit in the Y direction is required to be less than 10;

   (c) consistency of the charge measurement: $8.63 < Z_{Inner} < 9.37$ for fluorine, $10.58 < Z_{Inner} < 11.42$ for sodium, and $12.52 < Z_{Inner} < 13.48$ for aluminum;

   (d) the interpolation of the inner tracker track should be within the fiducial volume of at least five inner tracker layers;

2. External Tracker Layers (L1 and L9)

   (a) tracker L1 hit (associated to the track) with well-reconstructed clusters in both X and Y coordinates;

   (b) consistency of the charge measurement: $7.92 < Z_{L1} < 9.61$ for fluorine, $9.73 < Z_{L1} < 11.73$ for sodium, and $11.53 < Z_{L1} < 13.83$ for aluminum;

   (c) the normalized χ^2 of the track fit in the Y direction is required to be less than 10;

   (d) the difference between the χ^2 of the track fit with the inner and L1 hits and the χ^2 of the track fit with inner hits only in the Y direction is required to be less than 10;

(e) the interpolation of the inner tracker track should be within the fiducial volume of tracker L1;

(f) for $R \geq 1.2$ TV, the tracker L9 hit is required to have both X and Y clusters, with consistency of the charge measurement: $8.47 < Z_{L9} < 10.08$ for fluorine, $10.38 < Z_{L9} < 12.27$ for sodium, and $12.29 < Z_{L9} < 14.47$ for aluminum;

3. TOF

(a) velocity β is reconstructed using TOF signals plus tracker track information;

(b) $\beta > 0.4$;

(c) consistency of the charge measurement: $8.38 < Z_{upperTOF} < 10.5$ for fluorine, $10.33 < Z_{upperTOF} < 12.5$ for sodium, and $12.29 < Z_{upperTOF} < 14.5$ for aluminum;

(d) for $R \geq 1.2$ TV, consistency of the charge measurement: $8.38 < Z_{lowerTOF}$ for fluorine, $10.33 < Z_{lowerTOF}$ for sodium, and $12.29 < Z_{lowerTOF}$ for aluminum;

4. Physics Trigger (see Section 2.2)

5. Quality cuts

(a) Rigidity is greater than a factor of 1.2 times the maximum geomagnetic cutoff. Note that the cut in Section 3.1 is on the exposure time; this is the corresponding cut on the events.

The event counts passing all event selections amount to 0.29 million for fluorine, 0.46 million for sodium, and 0.51 million for aluminum.

3.3 Effective Acceptance

The effective acceptances A_i are calculated using MC simulation and then corrected for small differences between the data and simulated events related to a) event reconstruction and selection, namely in the efficiencies of velocity vector determination, track finding, charge determination and b) the details of inelastic interactions of nuclei in the AMS materials. Detailed discussion of these corrections is presented in 3.3.1.

The effective acceptance A_i is the product of the geometric acceptance A_{geom}, the selection efficiencies ε_{sel}, and the scale factor used to correct for the small differences between the MC simulation and data. The product $A_{geom}\varepsilon_{sel}$, is determined from MC as the product of the fraction of simulated events that pass the selection in the rigidity interval $(R_i, R_i + \Delta R_i)$ and the geometric factor A_0. The MC simulated events are generated isotropically in the top plane of a 3.9×3.9×3.9 m^3 concentric cube, which covers the entire AMS field of view. So the geometric factor A_0 is given by

$$A_0 = \int_S \int_\Omega cos\theta d\omega d\sigma = \pi \times 3.9 \times 3.9 m^2 sr \approx 47.78 m^2 sr, \tag{3.2}$$

where $d\sigma$ is the element of surface area S, $d\omega = d\phi dcos\theta$ is the element of solid angle Ω, θ is the polar angle, and ϕ is the azimuth angle.

3.3.1 Corrections to the Effective Acceptance

Detailed efficiency evaluations are presented in the following sections using the sodium nuclei as an example. The data to MC efficiency ratios are used as corrections to the effective acceptance.

3.3.1.1 Velocity Vector Determination Efficiency

The velocity vector determination efficiency requires that the velocity vector β is reconstructed using TOF measurements, and $\beta > 0.4$ to ensure that particles are down-going. The event sample used to study this efficiency requires the extrapolation

of tracker tracks within the TOF planes geometry, and the charge measured on the L1 and inner tracker is compatible with fluorine, sodium, and aluminum.

The efficiency of the velocity vector determination is evaluated to be more than 99.5%. For all nuclei species under study, excellent agreement between data and MC is found. The small correction is independent of rigidity and remains at the per mil level.

3.3.1.2 Track Finding Efficiency

The track finding efficiency includes the inner track reconstruction efficiency, L1 hit efficiency, and L9 hit efficiency for $R \geq 1.2$ TV.

The inner track reconstruction efficiency includes a convolution of the effect of the dead strips and non-sensitive area between ladders, the hit efficiency, and the minimum number of hits required for reconstructing a track.

To get the inner track reconstruction efficiency, a reconstructed track using only the TOF and TRD clusters is built to select the particle inside the tracker fiducial volume (see a sketch of AMS detector in Figure 3-2). Then the hits on the external layers (L1, L9) are taken to be the one with the highest charge and closest to the TOF and TRD track extrapolation. The sample is selected by requiring that the TOF and TRD track extrapolation is within the tracker fiducial volume, along with cuts on the charge measurements in the TOFs and the external layer hits. Then the inner track reconstruction efficiency corresponds to the efficiency that such a tracker track is built with at least 5 hits on the inner tracker layers and track fitting quality criteria $\chi^2 < 10$ in the bending coordinate. We also require the inner tracker charge to be larger than 6.5 for fluorine, 8.5 for sodium, and 11.5 for aluminum to separate the reconstructed track from any δ-ray tracks.

To estimate the rigidity without using the tracker, the events are split into three groups, and the rigidity is estimated by:

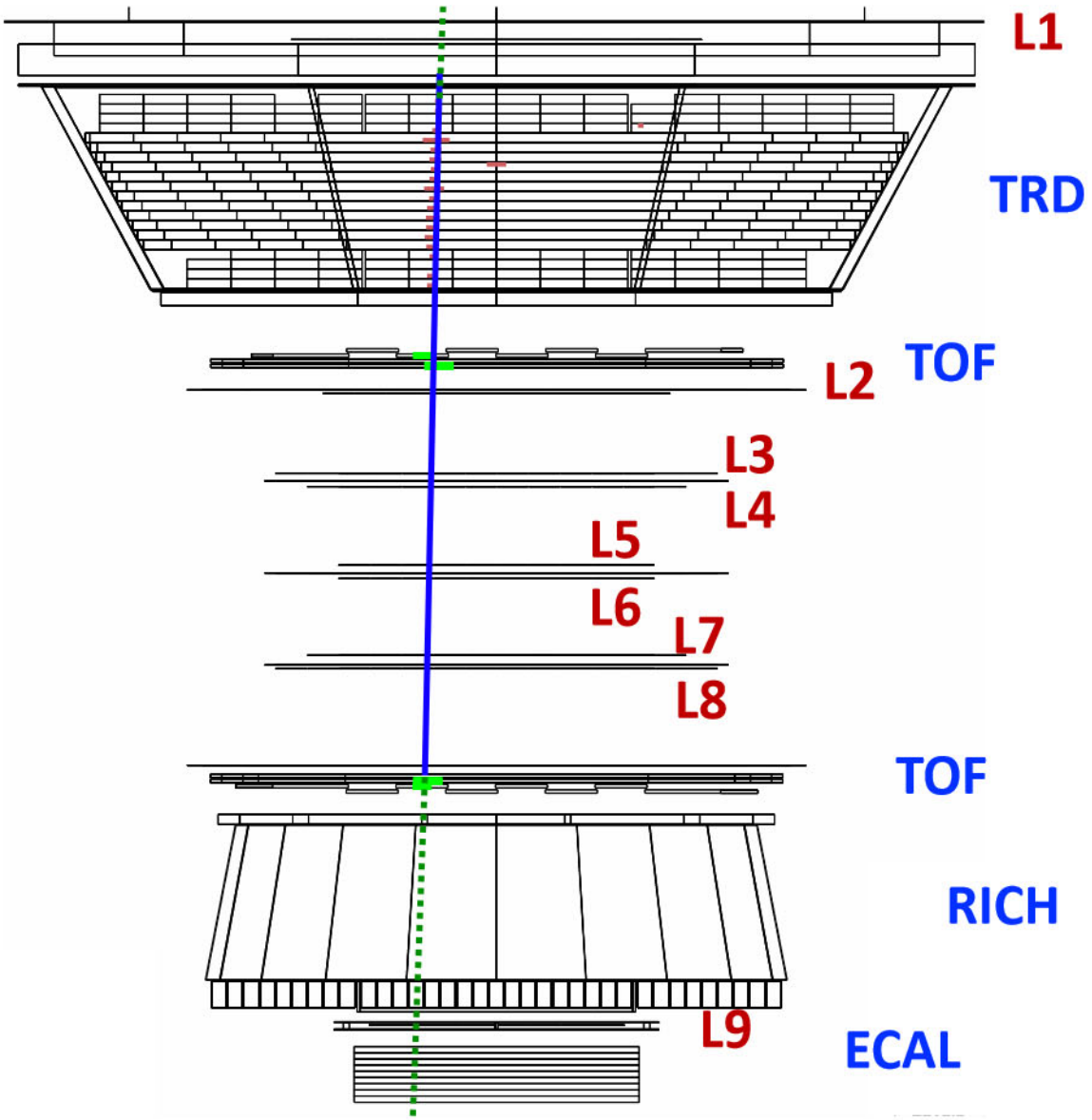

Figure 3-2: Schematic of the AMS detector. The solid blue line is the reconstructed track using the TOF and TRD clusters. The dashed green line indicates the TOF and TRD track extrapolation.

1. Below 6 GV, β measured by the TOF are converted to rigidity based on

$$R = \frac{m\beta}{Z\sqrt{1-\beta^2}} \tag{3.3}$$

   where Z is the particle charge, and m is the nuclei mass.

2. Between 6 GV and 20 GV, the geomagnetic cutoff is used as the rigidity estimator.

3. Above 20 GV, the energy deposition in the ECAL provides an estimation of the rigidity.

The inner track reconstruction efficiency is shown in Figure 3-3 for sodium data and MC. The inner track reconstruction efficiency, in low rigidity region, has a drop due to multiple scattering. Then it increases and becomes flat at high rigidity.

For fluorine, sodium, and aluminum, the ECAL energy deposition estimator can not provide the estimation above 20 GV due to limited statistics. However, by using carbon sample in data, which is much more abundant in cosmic rays, the inner track reconstruction efficiency is measured to be flat above 20 GV which is consistent with the MC prediction [88]. The systematic uncertainties arising from the assumption of the high rigidity behavior of the efficiencies are estimated by comparing constant extrapolation of the efficiency from 20 GV and true behavior of the efficiency as a function of generated rigidity, using MC simulated events.

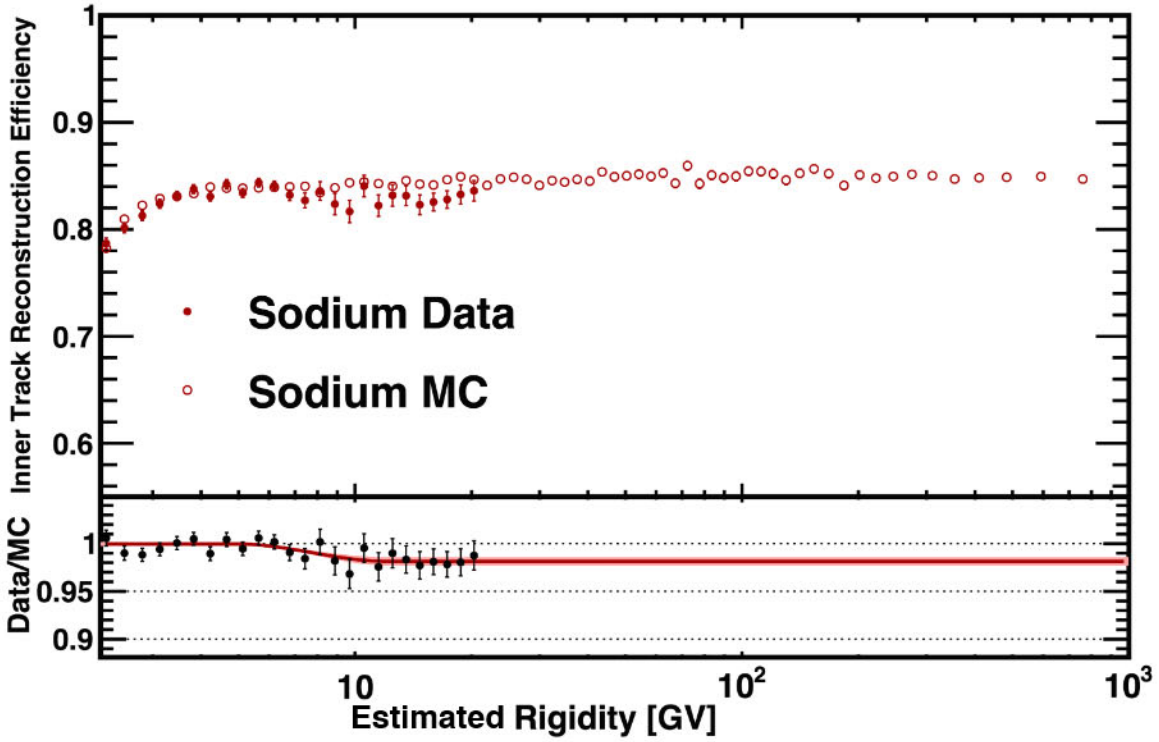

Figure 3-3: The inner track reconstruction efficiency for sodium data (filled dots) and MC simulation (open circles) as a function of estimated rigidity. The bottom panel shows the ratio of the efficiency in data to simulation, along with the spline fit to the ratio (curve) and the 68% CL interval (band). The fit above 20 GV is obtained from constant extrapolation.

3.3.1.3 Charge Determination Efficiency

Charge measurements on L1, the inner tracker, the upper TOF, and, for $R \geq 1.2$ TV, the lower TOF, and L9 are required to be compatible with charge $Z = 9$ for fluorine, $Z = 11$ for sodium, and $Z = 13$ for aluminum.

Figure 3-4 shows the inner tracker charge distribution for samples selected by using the charge measurements with L1, the upper TOF, and the lower TOF. The selections on the inner tracker charge for fluorine, sodium, and aluminum are indicated by the dashed line in Figure 3-4. The selections ensure negligible charge confusion ($< 0.5\%$) from noninteracting nuclei. The rigidity dependence of the inner tracker charge determination efficiency for sodium data and MC simulation is shown in Figure 3-5. For all nuclei species under study, a good agreement between MC and data is observed with discrepancies of less than 1%.

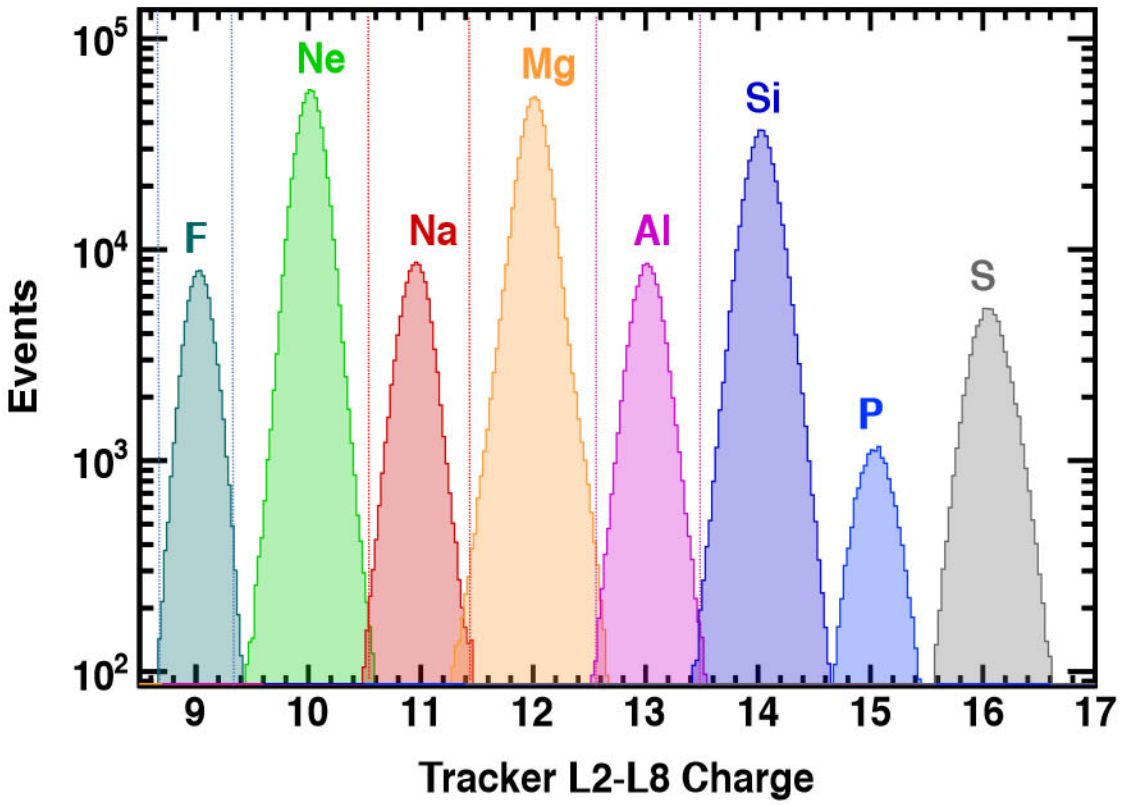

Figure 3-4: Charge distribution measured by the inner tracker for nuclei from Z=9 to Z=16 selected by charge measured with L1, the upper TOF, and the lower TOF. The vertical dashed lines indicate the charge selection for fluorine (cyan), sodium (red), and aluminum (magenta).

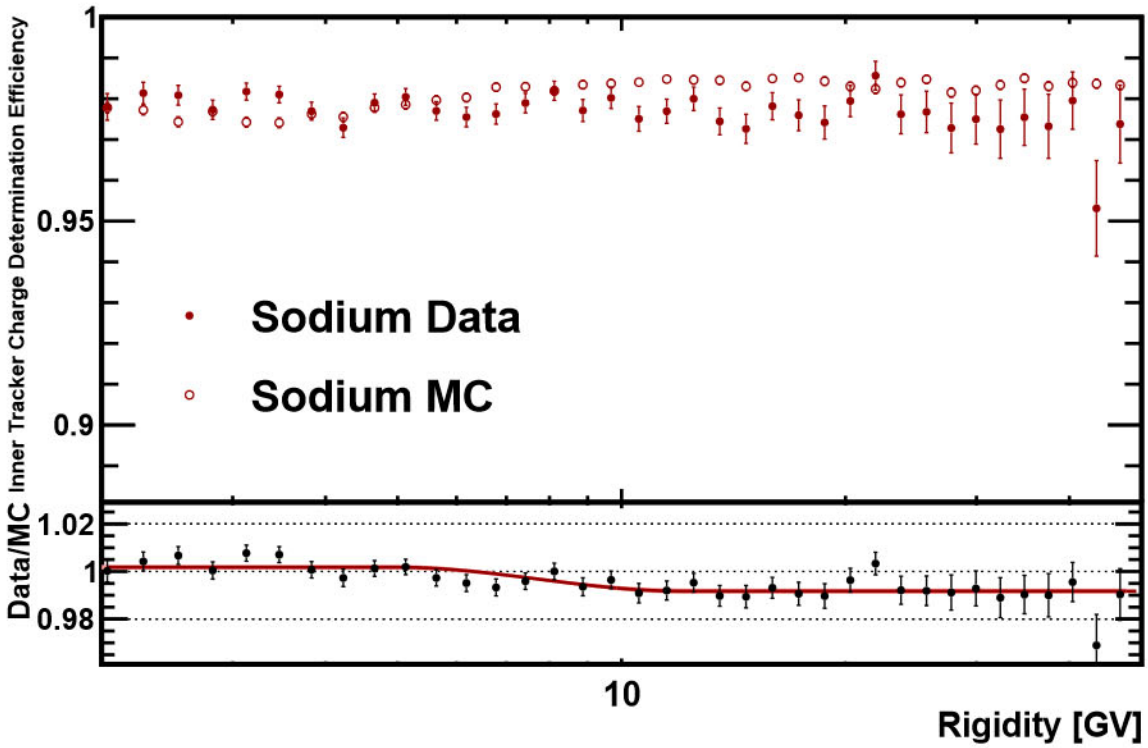

Figure 3-5: The inner tracker charge determination efficiency for sodium data (filled dots) and MC simulation (open circles) as a function of rigidity. The bottom panel shows the ratio of the efficiency in data to simulation, along with the spline fit to the ratio (curve) and the 68% CL interval (band not visible).

3.3.2 Total Correction

With all the efficiencies and the data/MC efficiency ratios, the total correction to the effective acceptance is obtained as the product of all individual efficiency ratios.

The total data to MC correction (red curve) applied to the MC acceptance of sodium is shown in Figure 3-6. The red band shows the systematic uncertainty of the ratio. The total corrections to the effective acceptance from the differences between data and MC simulation were found to be $< 4\%$ over the entire rigidity range. Similar corrections are obtained for fluorine and aluminum.

The systematics related to reconstruction and selection can be evaluated from the uncertainty associated with different correction factors (i.e., MC to data efficiency ratios). Since the efficiency ratios are parameterized by a spline fit and an extrapolated constant fit at high rigidity, the systematic error is contributed by the uncertainty

of the spline fit and the constant assumption. For the spline fit, the 68% CL interval obtained from the fit is taken as the systematic error. In order to estimate the systematic error of the constant assumption, by comparing constant extrapolation of the efficiency to high rigidity and true behavior of the efficiency as a function of generated rigidity, this deviation is taken as the systematic uncertainty. The systematic errors on the fluxes associated with the reconstruction and selection are $< 1\%$ over the entire rigidity range.

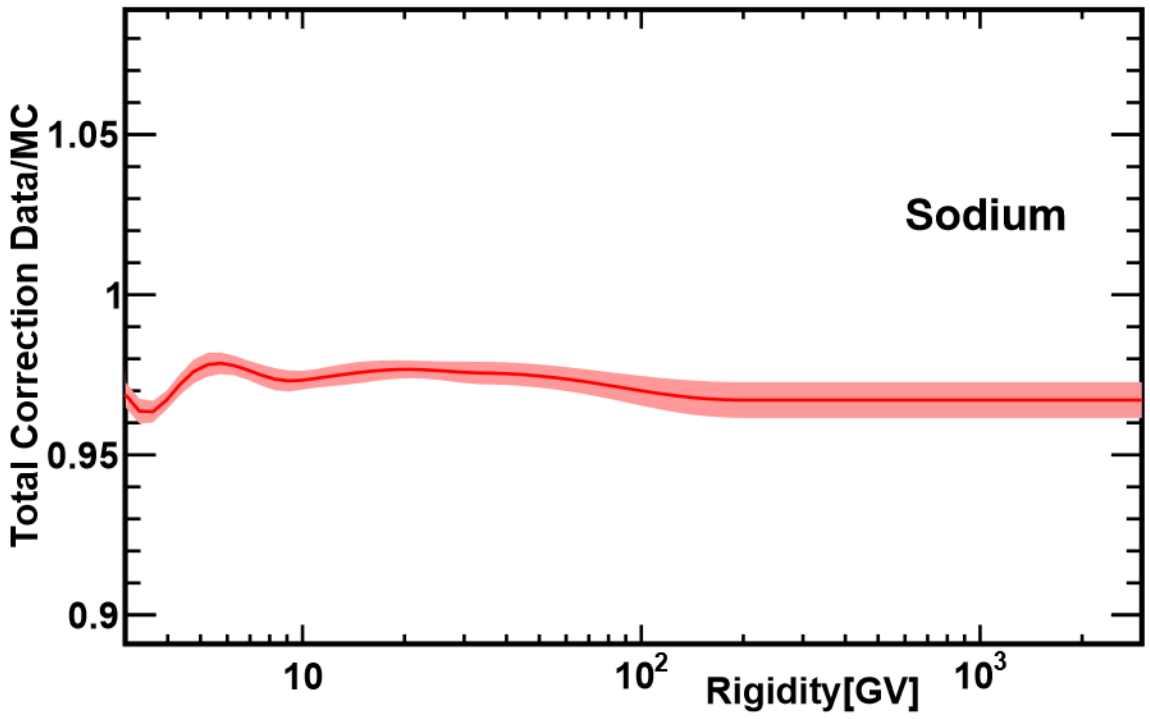

Figure 3-6: The sodium nuclei total data to MC correction factor (red curve) as a function of rigidity. The red band represents the systematic uncertainty of the correction factor at 68% CL.

3.4 Nuclear Interaction Cross Section

Cosmic ray nuclei entering AMS could interact with the detector materials. In order to accurately measure cosmic ray fluxes, precise knowledge of nuclear interactions with detector materials is crucial. A dedicated study [84] has been performed to verify and tune the description of inelastic nuclear interactions in the AMS MC simulation.

To simulate the nuclear interactions with the AMS materials, the GEANT4 Glauber-Gribov model [83,89] is used for the interaction cross-section simulation; the INCL++ package [90] is used to model inelastic interactions below 5 GeV/n, while the DPM-JET package [91,92] is used at higher energies.

The material traversed by nuclei between L1 and L9 is composed, by weight, of 67% carbon, 21% aluminum, and small amounts of silicon, oxygen, hydrogen, sodium, and other elements. Most materials are between L1 and L2 (mainly the TRD and Upper TOF) and between L8 and L9 (mainly the Lower TOF and RICH).

Since the inelastic cross sections of Nuclei + C, and Nuclei + Al have been measured only below a few GV for some species, to accurately determine the effect on the acceptance of nuclear interactions in the detector, we have developed the methods to precisely measure the magnitude and the rigidity dependence of the survival probability of each nuclei species when traversing the detector materials.

The survival probability ε^{sur} (i.e., the probability of a particle passing the detector without inelastic interaction) can be expressed by

$$\varepsilon^{sur} = e^{-n\sigma_I} \tag{3.4}$$

where n is the total number of target nuclei per area and σ_I is the nuclear interaction cross section.

3.4.1 Nuclear Survival Probabilities

The survival probability between L1 and L2, and between L8 and L9 are measured using data periods (1.4×10^5 s) in which AMS was oriented "horizontally", i.e., tilted $90° \pm 10°$ with respect to the local zenith. In this condition, cosmic nuclei can travel from L9 to L1 and from L1 to L9, as shown in Figure 3-7. In both cases, the inner tracker L2-L8 is used to identify particles and to measure their rigidities. The L1-L2 survival probability is evaluated by preselecting particles with the inner tracker, using the upper part as a target, and selecting surviving particles with a charge cut on Layer 1. The L8-L9 survival probability is evaluated by preselecting particles with

the inner tracker, using the lower part as a target, and selecting surviving particles with a charge cut on Layer 9.

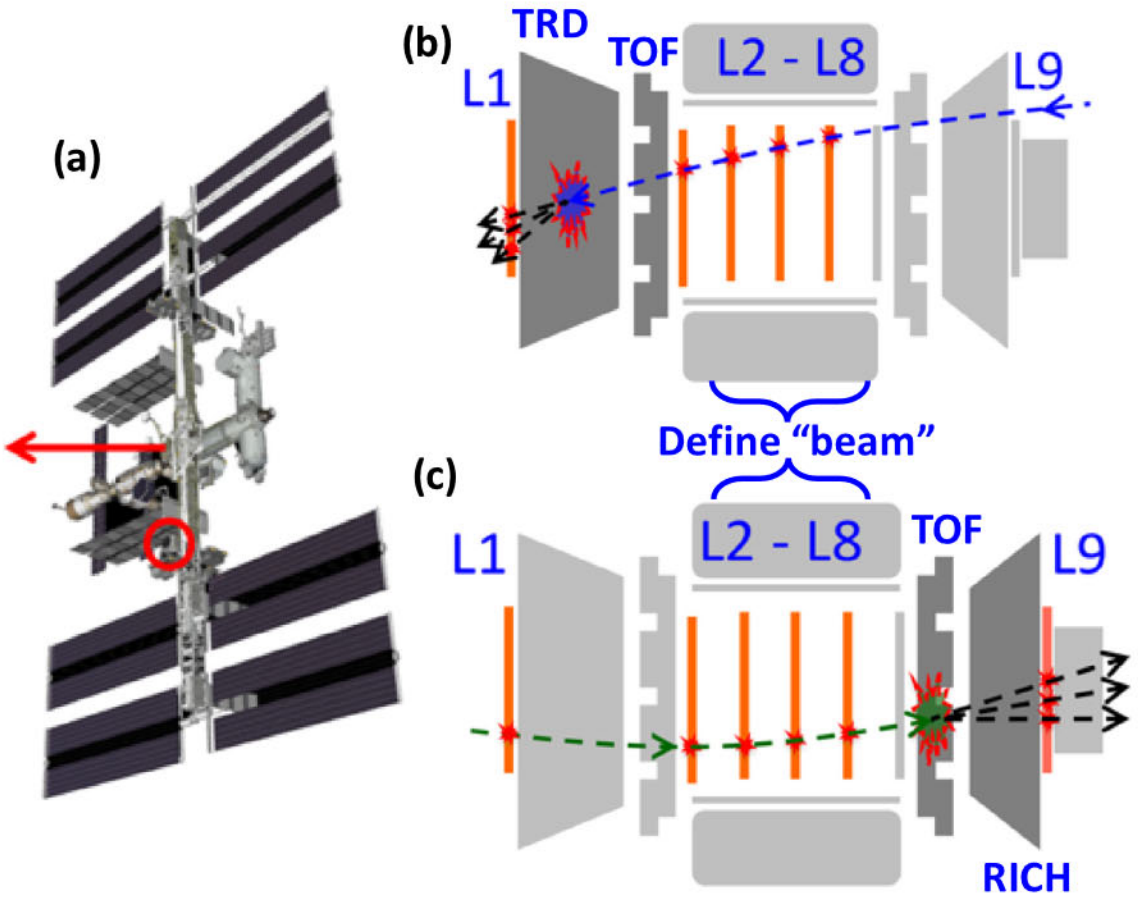

Figure 3-7: (a) Schematic of AMS flying horizontally. (b) Illustration of the L2 to L1 nuclei survival probability measurement in the AMS materials of upper TOF and TRD. (c) Illustration of the L8 to L9 nuclei survival probability measurement in the AMS materials of lower TOF and RICH. Note, that both in (b) and (c) we use L2–L8, located inside the magnet and marked "Define beam" in the figures, to identify particles and to measure their rigidities. Figure is from Ref. [60].

Given the short exposure time in the horizontal configuration (only 0.13% of the total exposure time), only the helium (He) event sample has enough statistics for this study. The comparison of the measured survival probabilities ε^{sur}_{Data} with the MC estimates ε^{sur}_{MC} is used to calculate the interaction cross sections on carbon target σ_C for data based on Eq. (3.4)

$$\sigma_C^{Data} = \frac{log(\varepsilon^{sur}_{Data})}{log(\varepsilon^{sur}_{MC})}\sigma_C^{MC}. \tag{3.5}$$

Figure 3-8 shows AMS tuned (derived from Eq. (3.5)) He+C interaction cross section as a function of rigidity comparing to the GEANT4 Glauber-Gribov model [83, 89]. We observed a systematic bias in the interaction cross sections of the GEANT4 Glauber-Gribov model. Earlier measurements from other experiments are also shown in Figure 3-8.

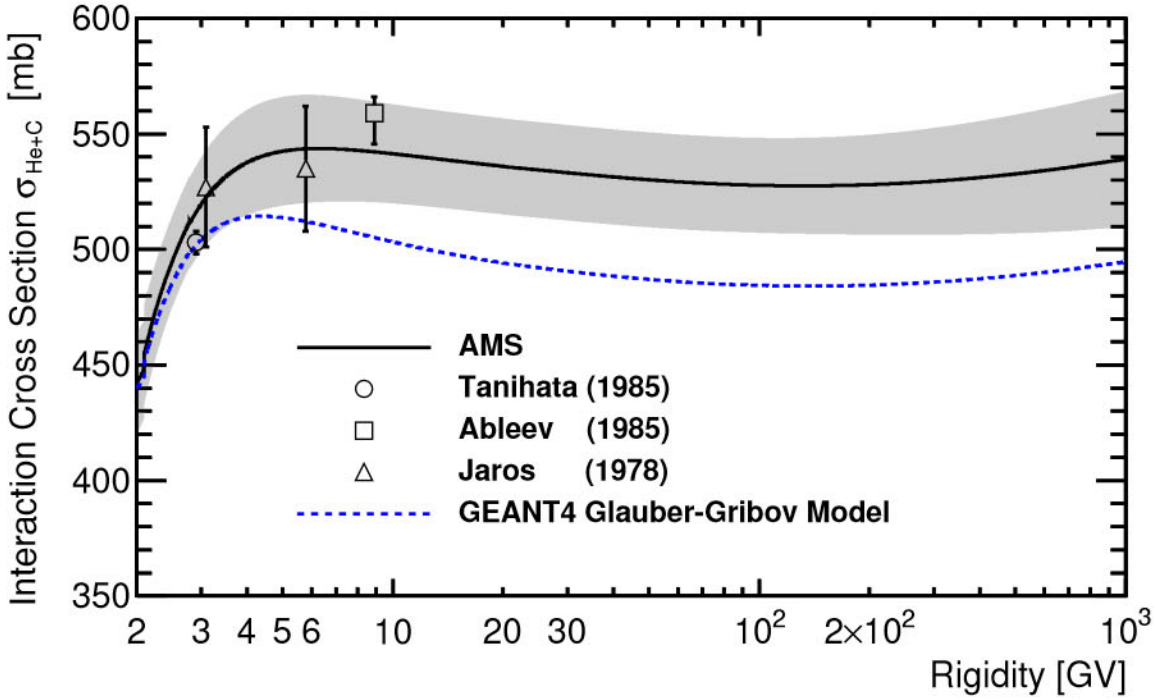

Figure 3-8: The He interaction cross section on carbon target (σ_{He+C}) as a function of rigidity measured by AMS (solid curve) in the rigidity range from 2 GV to 1 TV, together with earlier measurements (open circle [93], open squares [94] and open triangles [95]) and the GEANT4 Glauber-Gribov model [83, 89] (dashed curve). The grey band indicates the systematic error (68% CL) of the AMS result. Figure is from Ref. [84].

The cross-section model with rigidity dependence tuned to the AMS He data is scaled respectively in the AMS simulation to match the data for each nuclear species.

For heavy nuclei with $Z > 8$, the statistics collected during horizontal runs is too low. Hence to perform a similar study, a new estimation method using only downward going events (from tracker L1 to tracker L9) in nominal flight configuration has been developed. Due to limited statistics, fluorine, sodium, and aluminum events cannot be used to perform this study. Neon, magnesium, silicon, sulfur, and iron events are

used for this study and, from this study, the interaction cross sections of fluorine, sodium, and aluminum will be derived. The detailed discussion is carried out using magnesium (Mg) events.

The event samples of nuclei with charge Z are required to be downward going, have a reconstructed track in the inner tracker, and charge measured compatible with Z on tracker L1. Due to nuclear interactions between L1 and L2, the inner tracker then measures charge $Z' \leq Z$. The probability that a charge Z event on L1 will change to charge Z' in the inner tracker is $P^Z_{Z'} = \frac{N^{inner}_{Z'}}{\sum_{Z''} N^{inner}_{Z''}} = \frac{N^{inner}_{Z'}}{N_{tot}}$ where $N^{inner}_{Z'}$ is the number of events having inner tracker charge Z', and $N_{tot} = \sum_{Z''} N^{inner}_{Z''}$ is the total number of events of all possible charge channels.

The survival probability ε^{L12sur}_Z is evaluated when $Z'_{inner} = Z$ as no fragmentation happened, so $\varepsilon^{L12sur}_Z = P^Z_Z = \frac{N^{inner}_Z}{N_{tot}}$.

Figure 3-9 shows the inner tracker charge distribution for data and MC events selected with L1 charge $Z = 12$ (Mg) in the rigidity range from 20 to 21 GV. MC simulation well reproduces data, and all the break-up channels down to He are clearly visible.

As the charge measured on L1 is used to define the charge samples for the incoming particles, it is necessary to consider the possible contamination due to finite L1 charge resolution.

The contamination is evaluated using the event distribution from L2 charge. The L2 charge samples are selected using charge measured by L1, the upper TOF, and the L3-L8. The fraction of Z' nuclei $N^{L1Z}_{Z'}$ within the L1 charge selection ($|Z_{L1} - Z| < 0.5$) is

$$f^Z_{Z'} = \frac{N^{L1Z}_{Z'}}{\sum_{Z''} N^{L1Z}_{Z''}} = \frac{\int^{Z+0.5}_{Z-0.5} n_{Z'}(Q)dQ}{\sum_{Z''} \int^{Z+0.5}_{Z-0.5} n_{Z''}(Q)dQ} \tag{3.6}$$

where Q is the measured L2 charge, $n_{Z'}$ is the event distribution of charge Z' nuclei sample obtained from L2 charge, and $\sum_{Z''} N^{L1Z}_{Z''}$ is the total number of events of all possible charge channels within the L1 charge selection ($|Z_{L1} - Z| < 0.5$).

For L1 selected Mg nuclei sample, the estimated contaminations from Ne ($f^{Z=12}_{Z'=10}$),

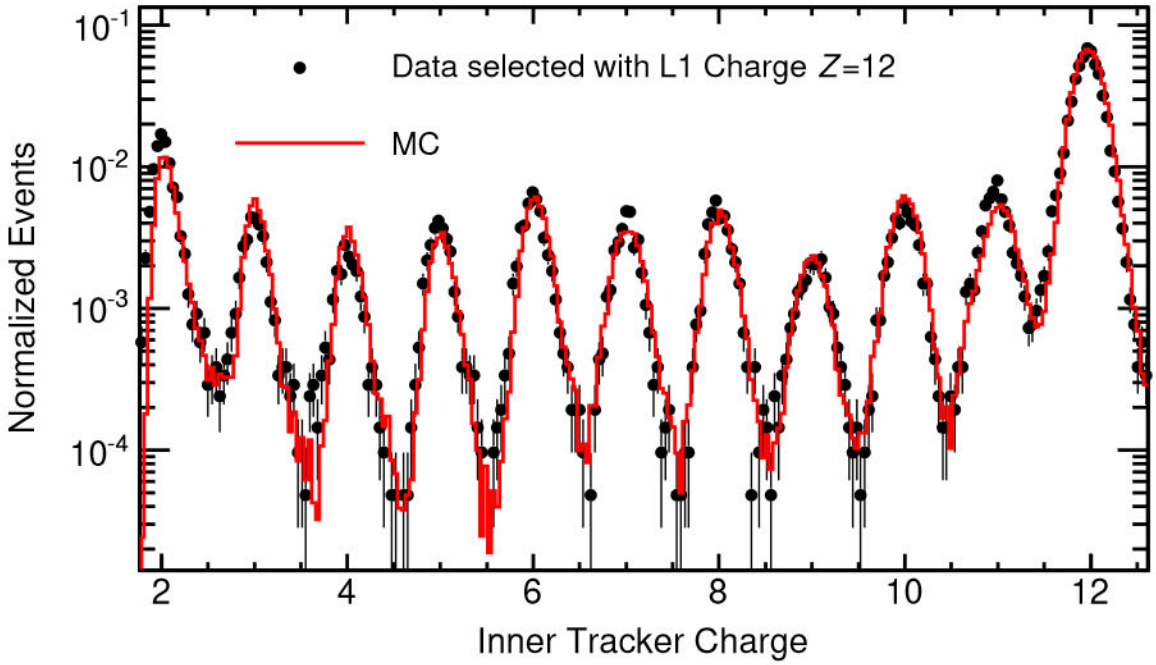

Figure 3-9: The inner tracker charge distribution for data (points) and MC (histogram) events selected with L1 charge Z = 12 (Mg) in the rigidity range from 20 to 21 GV. Both distributions have been normalized to their total number of events for comparison. Figure is from Ref. [84].

Na ($f^{Z=12}_{Z'=11}$), Al ($f^{Z=12}_{Z'=13}$), and Si ($f^{Z=12}_{Z'=14}$), are shown in Figure 3-10.

Considering the contamination, the number of events with inner tracker charge Z' become the sum of surviving events that carry charge Z' on L1 and the events that are fragmented from heavier nuclei Z'':

$$N^{inner}_{Z'} = \varepsilon^{L12sur}_{Z'} N^{L1Z}_{Z'} + \sum_{Z''>Z'} P^{Z''}_{Z'} N^{L1Z}_{Z''} = (\varepsilon^{L12sur}_{Z'} f^{Z}_{Z'} + \sum_{Z''>Z'} P^{Z''}_{Z'} f^{Z}_{Z''}) N_{tot}. \quad (3.7)$$

As the break-up probabilities of heavier nuclei with charge $Z'' > Z'$ is small ($P^{Z}_{Z''>Z} \ll 1$ as in Figure 3-11) and contamination of heavier nuclei is also small ($f^{Z}_{Z''>Z} \ll 1$ as in Figure 3-10), Eq. (3.7) is simplified to be $N^{inner}_{Z'} = \varepsilon^{L12sur}_{Z'} f^{Z}_{Z'} N_{tot}$. The survival probability with the contamination correction is given by

$$\varepsilon^{L12sur}_{Z'=Z} = \frac{N^{inner}_{Z'=Z}}{f^{Z}_{Z'=Z} N_{tot}}. \quad (3.8)$$

Figure 3-12 presents the MC to data ratio of the obtained L1-L2 survival proba-

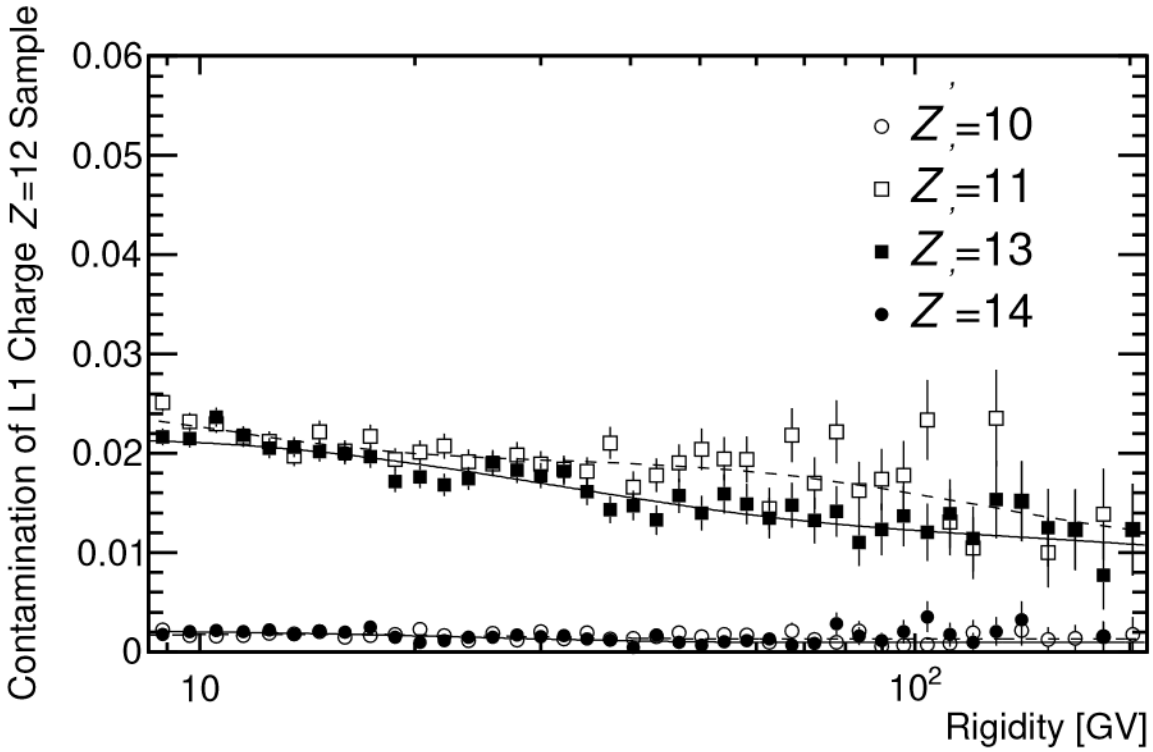

Figure 3-10: The estimated relative contamination from Ne ($f^{Z=12}_{Z'=10}$, open circles), Na ($f^{Z=12}_{Z'=11}$, open squares), Al ($f^{Z=12}_{Z'=13}$, solid squares), and Si ($f^{Z=12}_{Z'=14}$, solid circles) as functions of rigidity for a sample selected by charge $Z = 12$ (Mg) measured on L1. The contamination from $Z' < 10$ and $Z' > 14$ is negligible. Figure is from Ref. [84].

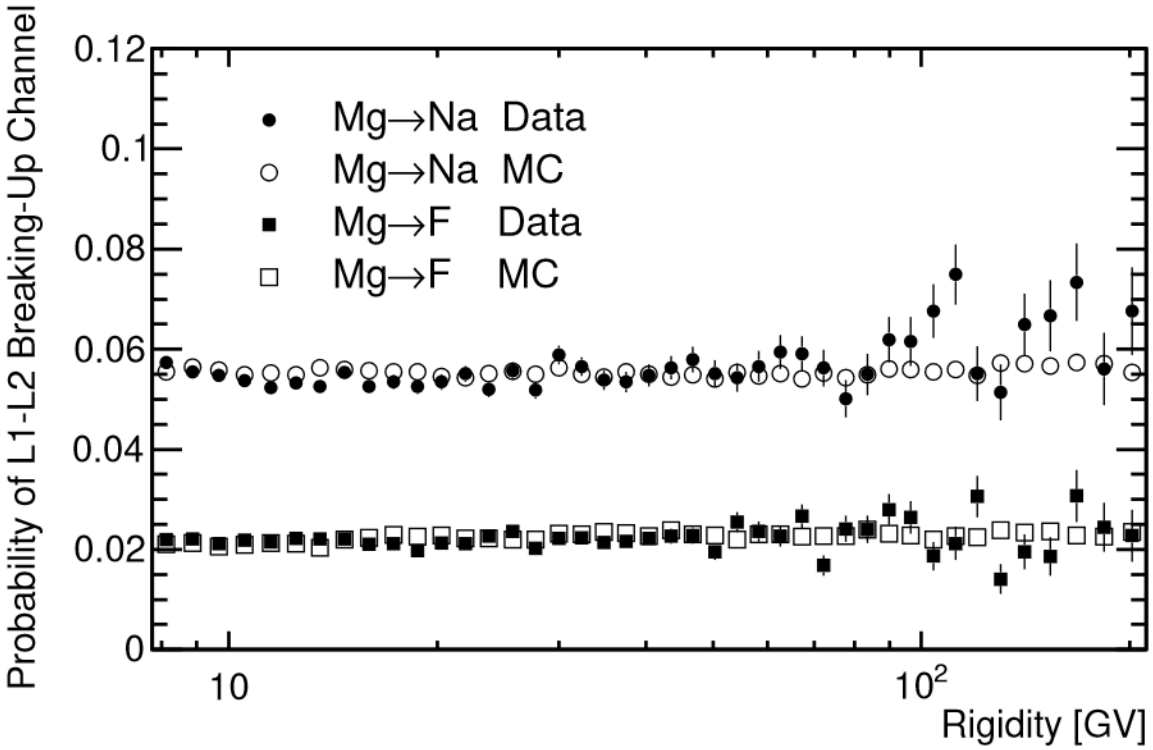

Figure 3-11: The nuclear break-up probabilities between L1 and L2 for the channels Mg to Na ($P^{Z=12}_{Z'=11}$) and Mg to F ($P^{Z=12}_{Z'=9}$) as functions of rigidity for data (solid circles and solid squares) and MC (open circles and open squares). Figure is from Ref. [84].

bilities for Mg nuclei. As seen, the survival probabilities in the MC simulation are in good agreement with the data for Mg nuclei over the entire rigidity range.

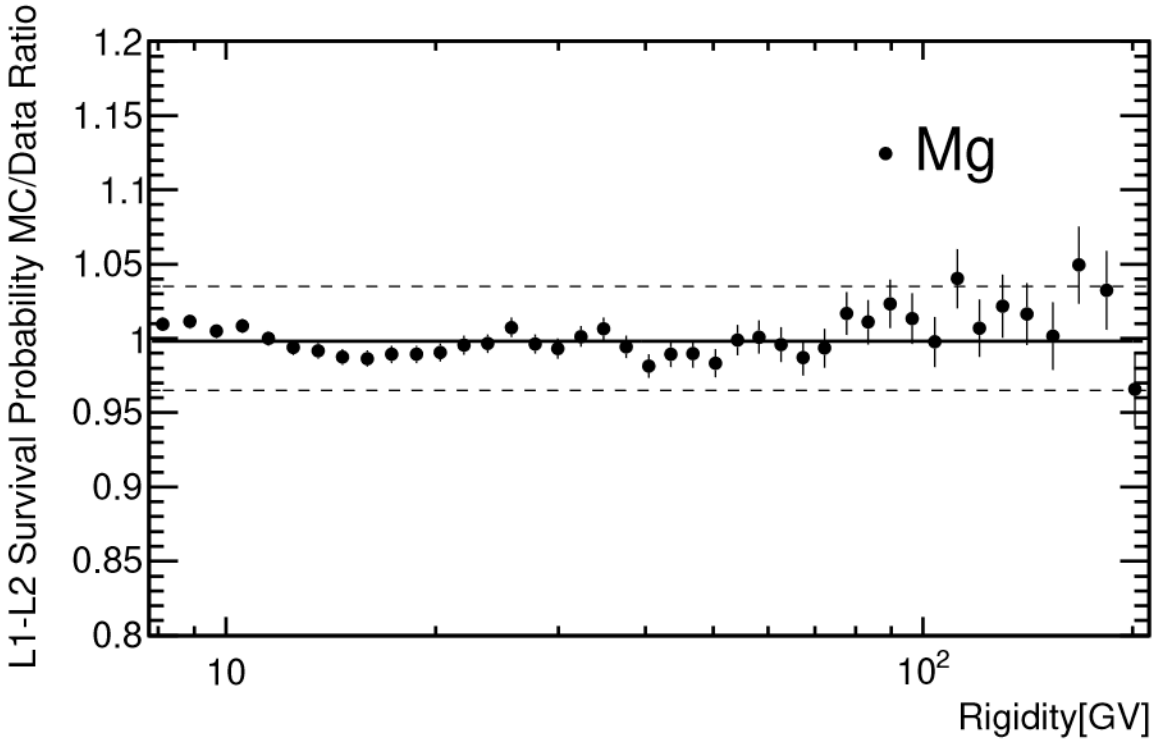

Figure 3-12: The MC/Data ratio of survival probabilities between L1 and L2 for Mg nuclei. The solid line shows the constant fit to the ratio and the dashed lines indicate the systematic error range (68% CL). Figure is from Ref. [84].

3.4.2 Nuclear Interaction Cross Sections on Carbon Target

Based on the study with He nuclei, we observed a bias in the interaction cross sections of the GEANT4 Glauber-Gribov model [83, 89]. Therefore we developed a new cross-section model to match the data. Since the cross-section model with rigidity dependence tuned to the AMS He data describes well other nuclei like Mg, the cross sections of different charged nuclei are take to have similar rigidity dependence. Therefore, for each nuclear species, one cross-section measurement at a given rigidity is enough to define the cross section over the entire rigidity range.

The AMS measured $\sqrt{\sigma_I}$ is parameterized as function of nuclear charge radius r_c studied by electron scattering, isotope-shift measurements, and studies of muonic atoms [96]:

$$\sqrt{\sigma_I} = k(r_c^p + r_c^t - r_0) \tag{3.9}$$

where $\sqrt{\sigma_I}$ is the square root of the interaction cross section, r_c^p is the charge radii of the projectile, r_c^t is the charge radii of the target, r_0 is an overlap charge radius parameter in nuclear collision, and k is a scaling factor.

Figure 3-13 shows the linear dependence of $\sqrt{\sigma_{N+C}^{15GV}}$ on r_c^p with $r_c^t = 2.4702 \pm 0.0022$ fm for carbon target [97]. The fit to the measured data yields $r_0 = 1.891 \pm 0.078$(fit) fm and $k = 10.23 \pm 0.25$(fit) $\pm$ 0.15(mat) mb$^{1/2}$fm^{-1}, with χ^2/d.o.f = 2.7/7 [84]. The first error quoted (fit) takes into account statistical and uncorrelated systematic errors. The second error (mat) is the correlated error from 3% uncertainty on the overall AMS materials, which could potentially simultaneously move all the measured points higher or lower.

Eq. (3.9) can be used to calculate the interaction cross section for cosmic-ray nuclei of low statistics for which we cannot perform the above cross-section study, such as fluorine (F), sodium (Na), and aluminum (Al). The interaction cross sections on carbon target is calculated by the parameterized Eq. (3.9) knowing the r_c^p. The nuclear interaction cross sections on carbon target for ^{19}F ($r_c^p = 2.8976 \pm 0.0028$ fm), ^{23}Na ($r_c^p = 2.9936 \pm 0.0021$ fm), and ^{27}Al ($r_c^p = 3.0610 \pm 0.0031$ fm) [97] are calculated to be $\sigma_{F+C}^{15GV} = 1265 \pm 84$(fit) $\pm$ 37(mat) mb, $\sigma_{Na+C}^{15GV} = 1336 \pm 88$(fit) $\pm$

39(mat) mb, and $\sigma_{Al+C}^{15GV} = 1387 \pm 90(\text{fit}) \pm 41(\text{mat})$ mb. The corresponding errors are calculated with propagation of uncertainty through Eq. (3.9).

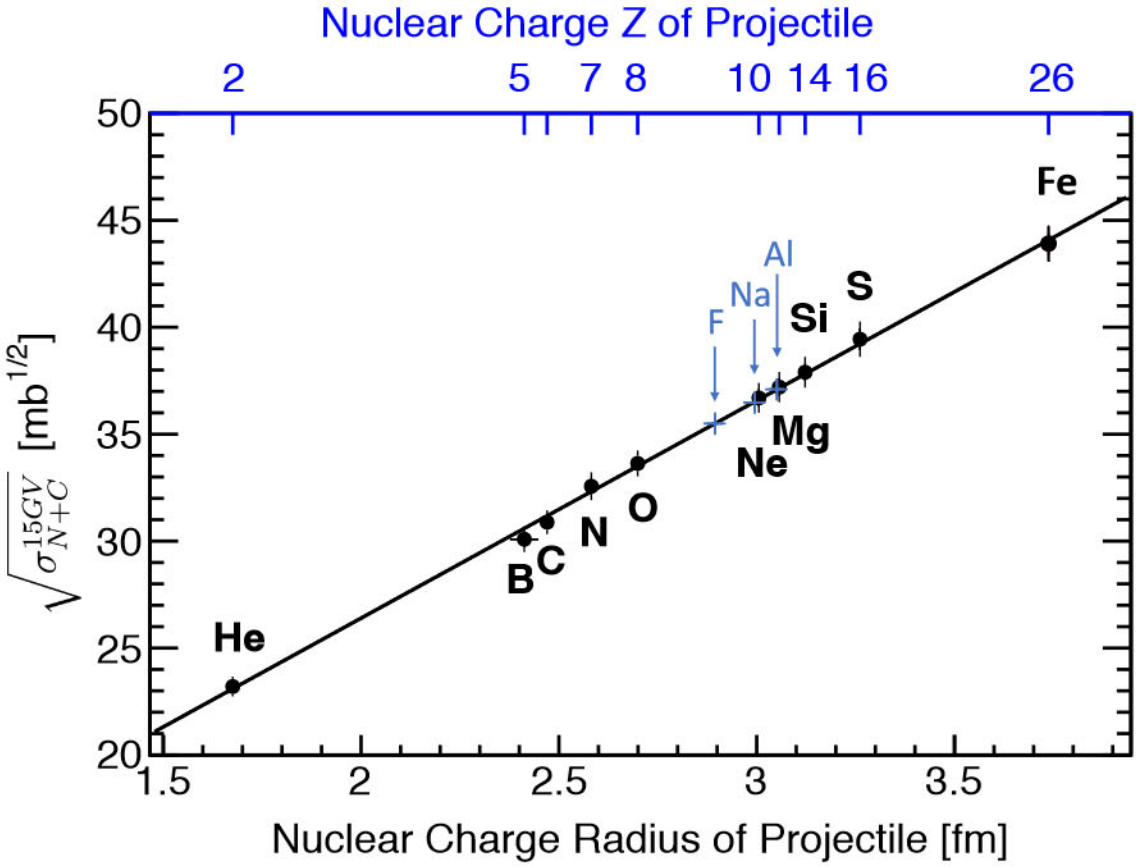

Figure 3-13: The square root of the interaction cross section on carbon target at rigidity 15 GV ($\sqrt{\sigma_{N+C}^{15GV}}$) as a function of projectile charge radius (r_c^p) [97]. The line shows the fit with Eq. (3.9). The isotopic compositions used are ^{4}He (He), 30%^{10}B+70%^{11}B (B), ^{12}C (C), 50%^{14}N+50%^{15}N (N), ^{16}O (O), ^{20}Ne (Ne), ^{24}Mg (Mg), ^{28}Si (Si), ^{32}S (S) and ^{56}Fe (Fe). As seen, the linear function describes the data well. Accordingly, the light blue markers show the extrapolation of the nuclear interaction cross sections on carbon target for ^{19}F, ^{23}Na, and ^{27}Al. Figure is updated from [84,98].

The corresponding systematic error due to uncertainties in the evaluation of the interaction cross section on the F flux is $< 3\%$ up to 100 GV and rises smoothly to 4% at 2.9 TV. The corresponding systematic error on both the Na and Al fluxes is $< 3.5\%$ up to 100 GV and rises smoothly to 4% at 3.0TV. Note that above 100 GV, the small rigidity dependence of the cross section from the Glauber-Gribov model is treated as an uncertainty and added in quadrature to the uncertainties from the measured interaction probabilities.

The total systematic error associated with the acceptance calculation is obtained by taking in quadrature this systematic error due to uncertainties in the evaluation of the inelastic cross section and systematic error from different correction factors in event reconstruction and selection (Section 3.3.2).

3.5 Background Estimation

After applying the charge selections on the tracker L1, inner tracker, upper and lower TOF, the background of fluorine, sodium, and aluminum samples come from two sources.

First is the residual background after L1 charge cut, resulting from interactions of heavier nuclei like Mg and Si in the material between L1 and L2 (TRD and upper TOF).

The background to F events is evaluated using a data-driven method, i.e., by fitting the charge distribution from L1 with charge distribution templates of O, F, Ne, and Na, as shown in Figure 3-14. The charge distribution templates are obtained from a selection of non-interacting samples at L2 by requiring that L1 and L3–L8 measure the same charge value. The charge distributions should be nearly identical for L1 and L2, since the layout and electronics are the same [74]. The background is then calculated by integrating the charge templates of O, Ne and Na within the L1 charge selection interval for F indicated by the dashed lines. The same procedure is applied to evaluate the background to Na and Al events, as shown in Figure 3-15 and Figure 3-16.

This background varies smoothly from 4% below 10 GV to 15% at 2.9 TV for F, from 8% below 10 GV to 25% at 3 TV for Na, and from 9% below 10 GV to 16% at 3 TV for Al.

The second source of background is the background resulting from interactions of heavier nuclei like Mg and Si in the material above L1 (thin support structures made of carbon fiber and aluminum honeycomb).

Interactions that happened above L1 cannot be identified by AMS since they

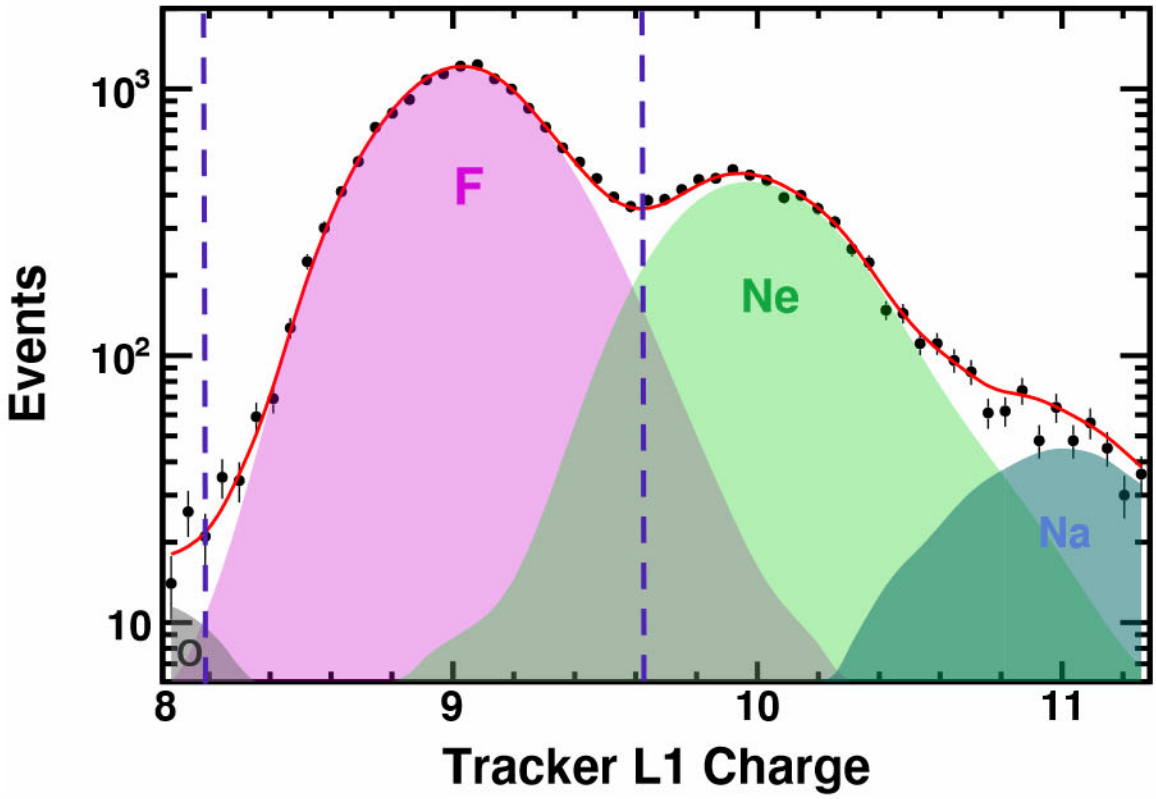

Figure 3-14: Charge distributions measured by tracker L1 for fluorine events selected by the inner tracker L2-L8 in the rigidity range between 18 and 22 GV (black dots). The solid red curve shows the fit to the data of the sum of the O, F, Ne, and Na charge distribution templates. The templates are obtained from non-interacting samples at L2 by using combined L1, upper TOF, L3-L8, and lower TOF charge selections. The charge selection for F applied on tracker L1 is shown as vertical dashed lines.

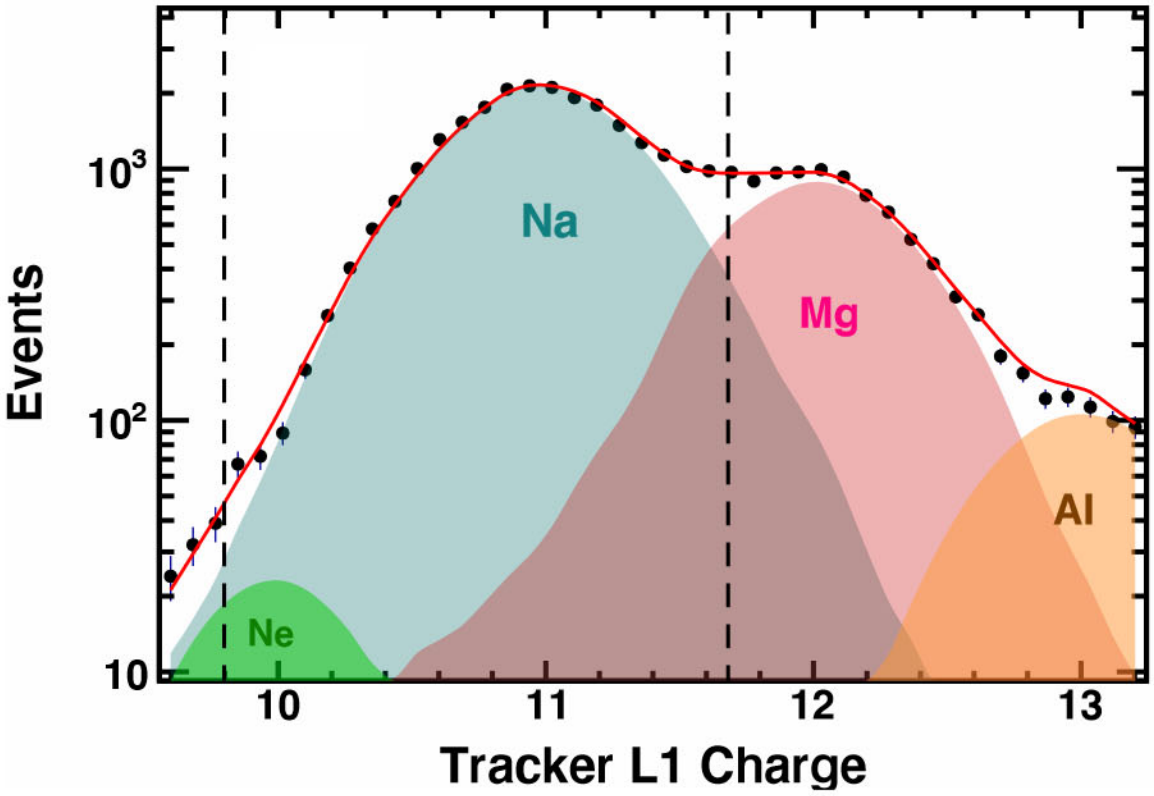

Figure 3-15: Charge distributions measured by tracker L1 for sodium events selected by the inner tracker L2-L8 in the rigidity range between 18 and 22 GV (black dots). The solid red curve shows the fit to the data of the sum of the Ne, Na, Mg, and Al charge distribution templates. The templates are obtained from non-interacting samples at L2 by using combined L1, upper TOF, L3-L8, and lower TOF charge selections. The charge selection for Na applied on tracker L1 is shown as vertical dashed lines.

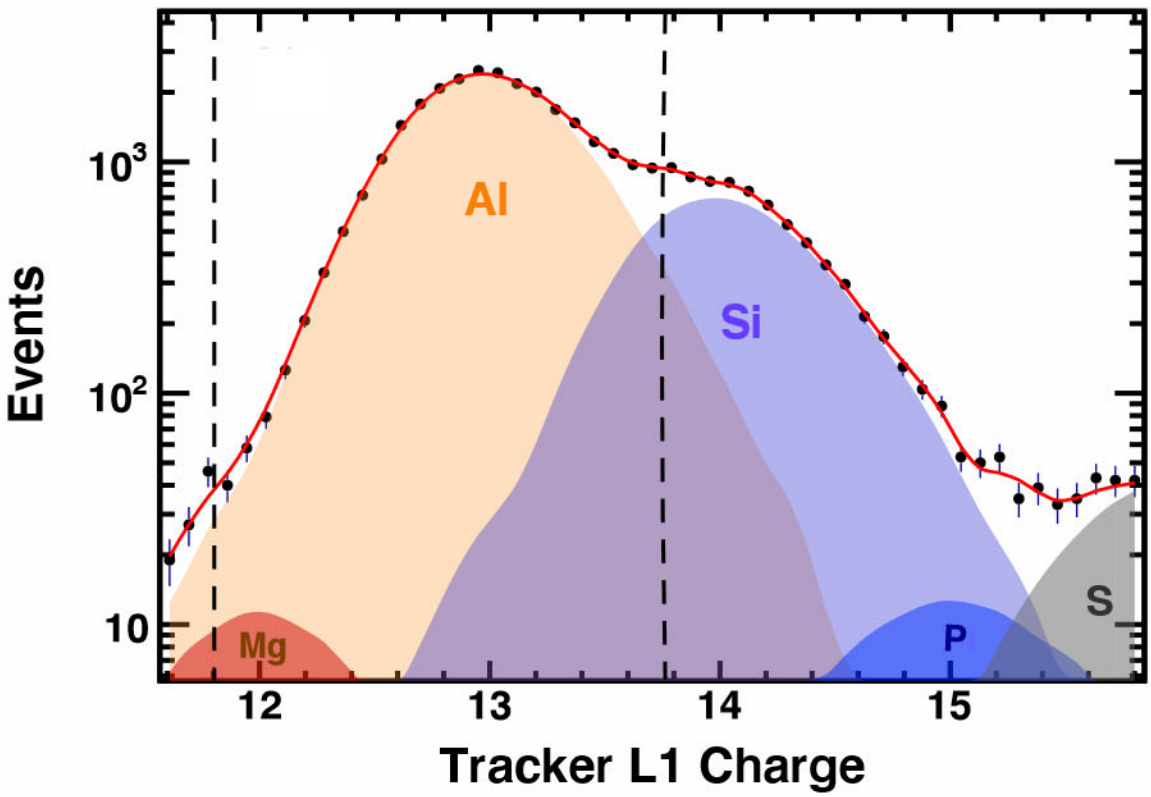

Figure 3-16: Charge distributions measured by tracker L1 for aluminum events selected by the inner tracker L2-L8 in the rigidity range between 18 and 22 GV (black dots). The solid red curve shows the fit to the data of the sum of the Mg, Al, Si, P, and S charge distribution templates. The templates are obtained from non-interacting samples at L2 by using combined L1, upper TOF, L3-L8, and lower TOF charge selections. The charge selection for Al applied on tracker L1 is shown as vertical dashed lines.

happen before particles reaching the first sub-detector, tracker L1. Therefore, this background is estimated from simulation, using MC samples reweighted according to AMS flux measurements (e.g., MC fluorine samples are reweighted to the fluorine flux from this analysis). The MC simulation of nuclear interactions has been validated with data using nuclear charge changing cross sections (Ne; Mg; Si; ...→ F + X) measured by AMS, as shown in Figure 3-17.

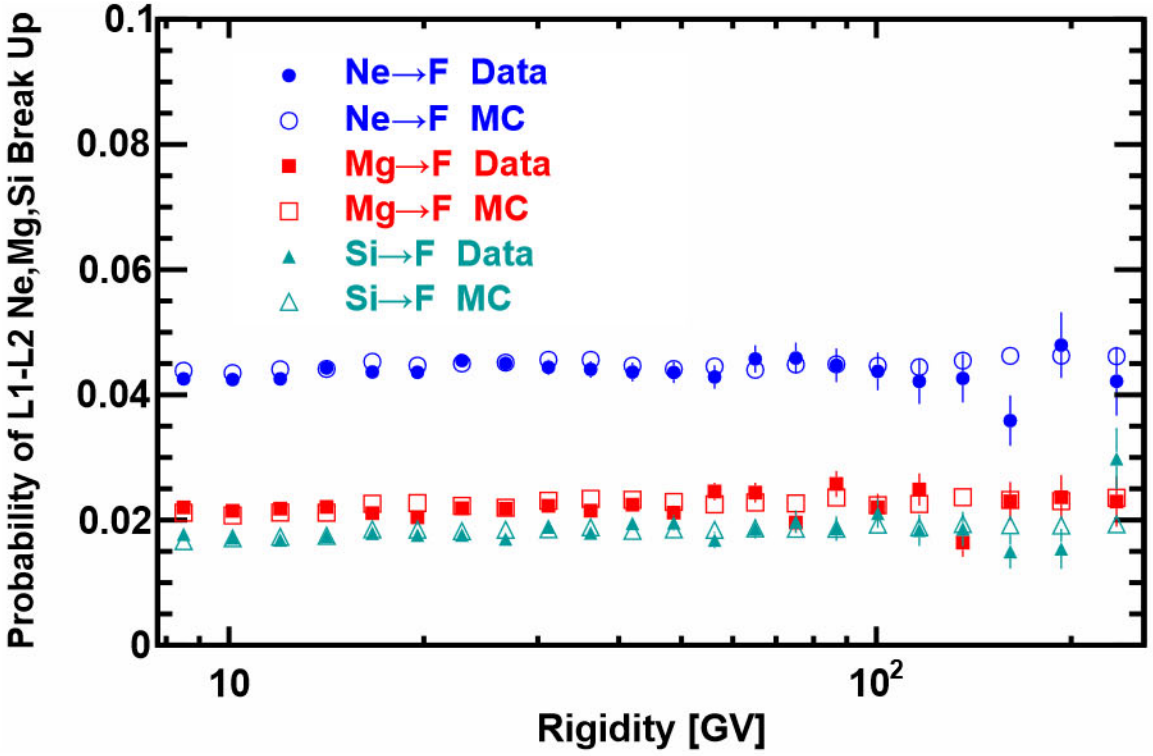

Figure 3-17: Comparison of the simulated (MC) and measured (Data) Ne, Mg, Si →F break-up probabilities between L1 and L2.

Considering that the total collected fluorine event counts N'_F are the sum of event counts from incoming fluorine nuclei N_F and the above tracker L1 background $\sum N_{X\to F}$, the fluorine flux without this background can be expressed as

$$\begin{aligned}\Phi_F = \frac{N_F}{A_F T \Delta R} = \frac{N'_F - \sum N_{X\to F}}{A_F T \Delta R} &= \frac{N'_F - \sum \Phi_X A_{X\to F} T \Delta R}{A_F T \Delta R} \\ &= \Phi'_F(1 - \sum \frac{A_{X\to F}}{A_F}\frac{\Phi_X}{\Phi'_F}) \\ &= \Phi'_F(1 - \sum \delta_X),\end{aligned} \tag{3.10}$$

where Φ'_F is the fluorine flux before subtraction of this background and $A_{X\to F}$ is the fluorine acceptance obtained from MC samples of fragmented nuclei X (Ne, Mg, ...). The MC acceptance $A_{X\to F}$ and A_F are expressed in reconstructed rigidity to account for the bin-to-bin migration effect due to the finite tracker rigidity resolution. So, the above tracker L1 background $\sum \delta_X$ is estimated in the reconstructed rigidity and will be subtracted from the raw event counts before unfolding.

Figure 3-18 shows the rigidity dependence of the above tracker L1 background for F.

The same procedure is applied to evaluate the background to Na and Al events, the rigidity dependence of this background is shown in Figure 3-19 for Na and Figure 3-20 for Al.

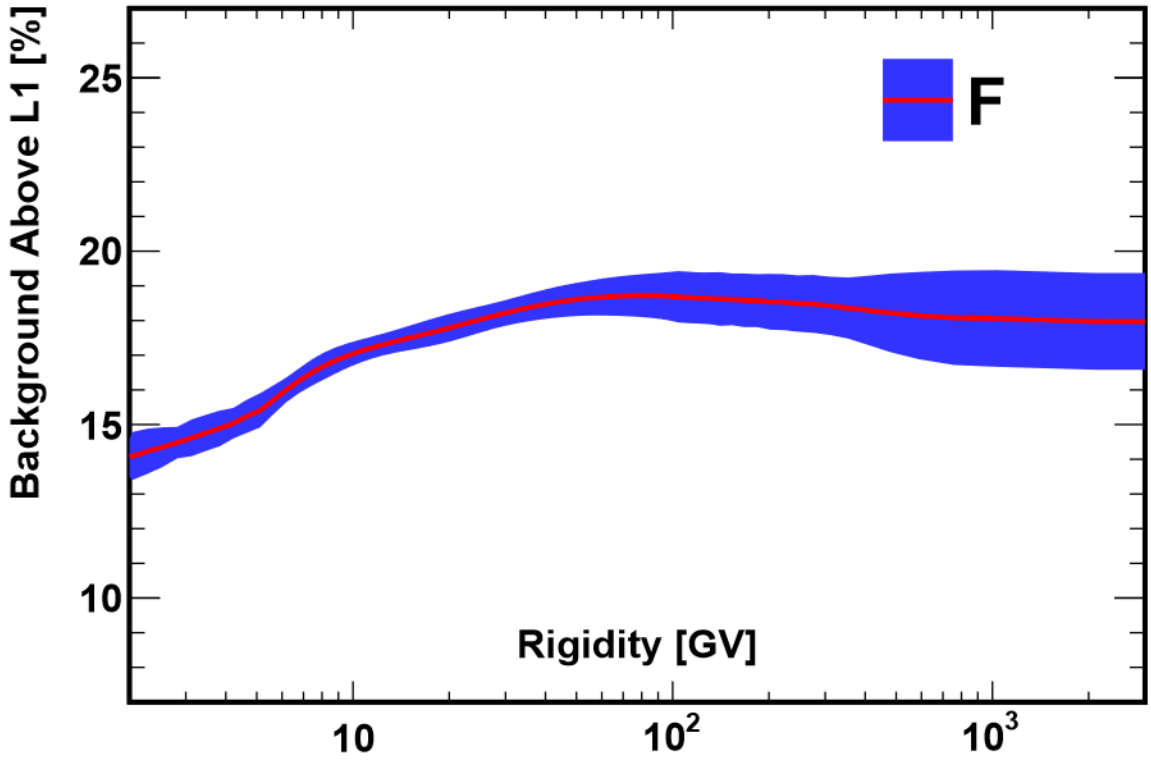

Figure 3-18: F background from heavier nuclei interactions above L1 together with its uncertainty at 68% CL (blue shaded area) as a function of rigidity. The amount of background as a function of rigidity is determined by nuclei interaction cross sections, by the relative abundance of heavier nuclei to F and by L1, upper TOF and lower TOF charge selection criteria, which were chosen to minimize the background uncertainty.

The systematic uncertainty from background evaluation is separated into two com-

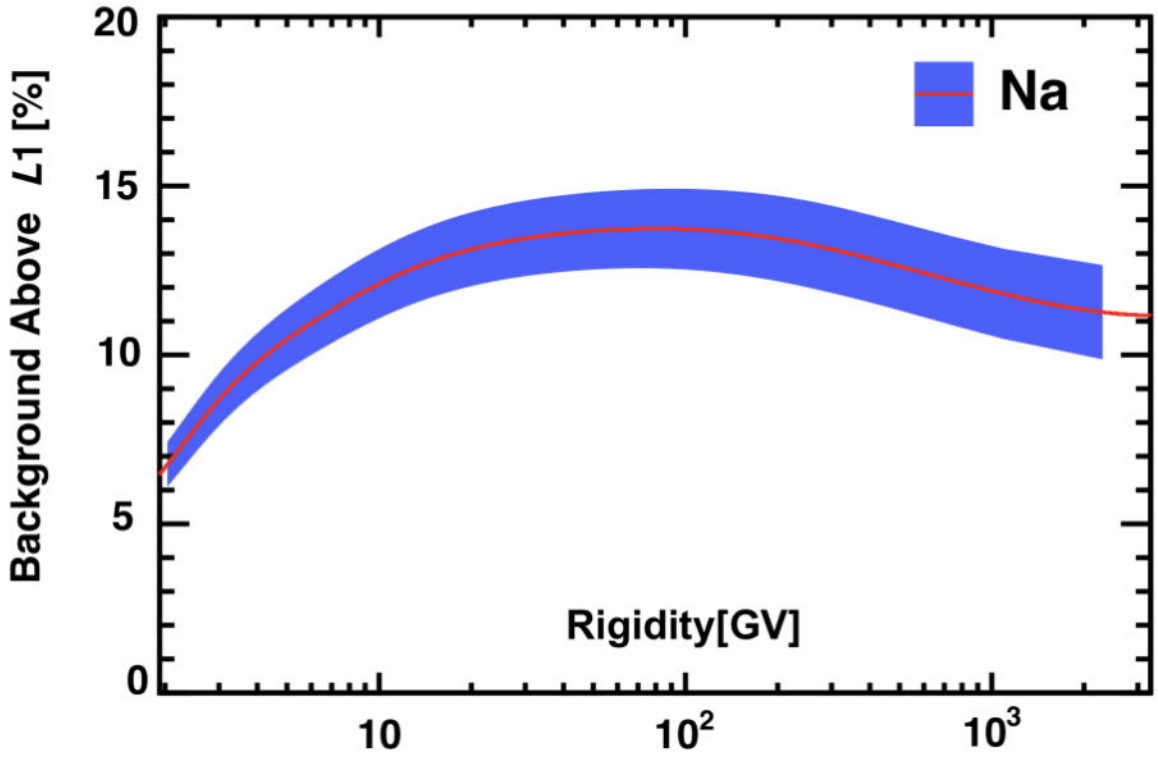

Figure 3-19: Na background from heavier nuclei interactions above L1 together with its uncertainty at 68% CL (blue shaded area) as a function of rigidity. The amount of background as a function of rigidity is determined by nuclei interaction cross sections, by the relative abundance of heavier nuclei to Na and by L1, upper TOF and lower TOF charge selection criteria, which were chosen to minimize the background uncertainty.

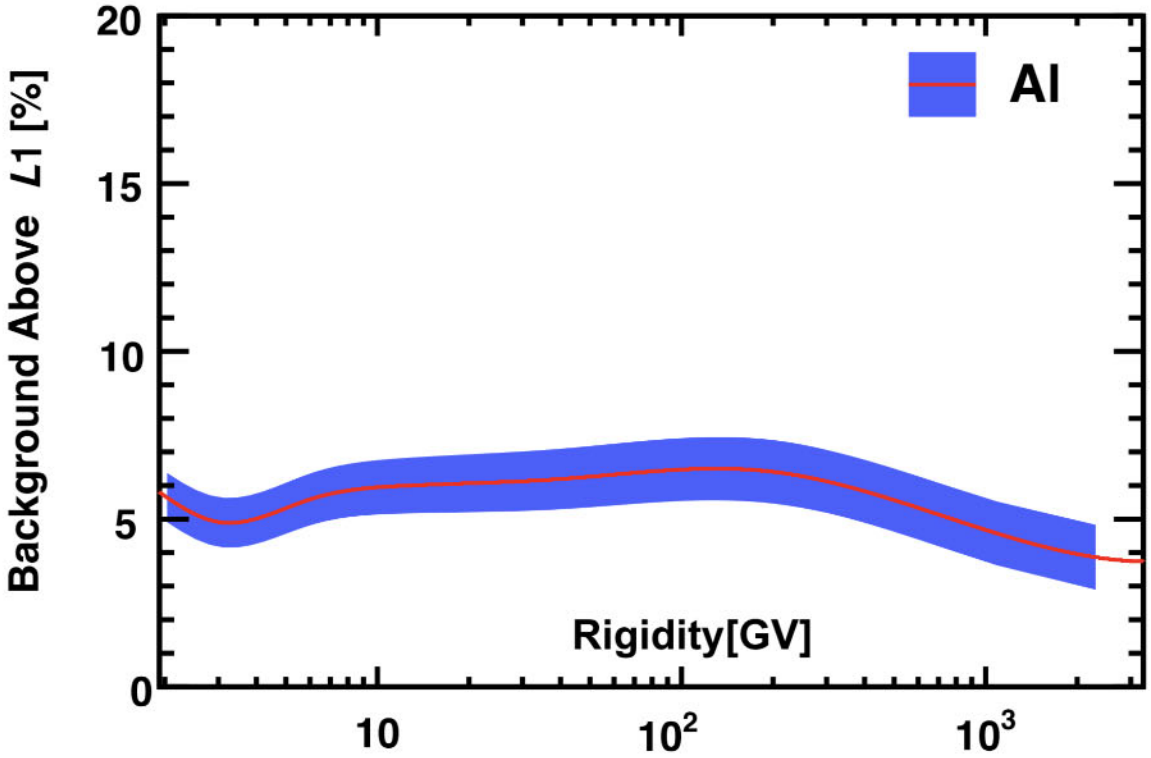

Figure 3-20: Al background from heavier nuclei interactions above L1 together with its uncertainty at 68% CL (blue shaded area) as a function of rigidity. The amount of background as a function of rigidity is determined by nuclei interaction cross sections, by the relative abundance of heavier nuclei to Al and by L1, upper TOF and lower TOF charge selection criteria, which were chosen to minimize the background uncertainty.

ponents: uncertainty from estimation of the residual interaction background between L1 and L2, and from interactions above L1.

The background from interactions between L1 and L2 is estimated by the template fit with charge distribution templates obtained from non-interacting samples at L2. The same procedure is performed by using samples at L1 to evaluate the background contamination and the uncertainty that arises from different template selection is taken as the systematic error.

The systematic error of above L1 background estimation comes from the uncertainties of the MC acceptance ratio $A_{Z'\to Z}/A_Z$ and the flux ratio $\Phi_{Z'}/\Phi_Z$ in Eq. (3.10). The acceptance ratio depends on the nuclear charge changing cross sections on AMS material (Mg→F+X, Mg→Na+X, Si→Al+X ..). The uncertainty of this ratio can be evaluated by comparing the difference between the MC to data ratio of $Z' \to Z$ break-up channel probability in L1-L2 and L8-L9.

The overall uncertainty due to background subtraction is obtained by taking in quadrature the uncertainties of the two backgrounds. It is 1.5% at 2 GV, 2% at 100 GV, and 6% at 2.9 TV for F, 1.5% at 2 GV, 1.5% at 100 GV, and 6% at 3.0 TV for Na, and 1% at 2 GV, 1.5% at 100 GV, and 5% at 3.0 TV for Al.

3.6 Trigger Efficiency

The trigger efficiency is calculated by

$$\varepsilon_{trig}(R) = \frac{N_{phys}(R)}{N_{phys}(R) + f_{unbiased} \times N_{unbiased}(R)} \tag{3.11}$$

where N_{phys} corresponds to all the events passing the selection cuts and with at least one physics trigger, $N_{unbiased}$ is the number of events with only unbiased trigger, and $f_{unbiased}$ is the scale factor for unbiased events, which is 100. The different trigger criteria have been discussed in Section 2.2. As discussed in Section 3.5, nuclear interactions that happened between L1 and L2 and above L1 represent backgrounds in the fluorine, sodium, and aluminum samples. The secondaries produced in the

nuclear interactions trigger the ACC and cause bias in the trigger efficiency study, so the trigger efficiency of fluorine, sodium, and aluminum can not be measured directly.

An energetic charged particle moving through matter interacts with the bound orbital electrons in the material and transfers energy to the electrons. When the energy transferred to the electron is higher than the ionization energy, the electron is ejected from its orbit. This electron is referred as the δ-ray. Since the inefficiency is mostly due to δ-rays produced by incoming nuclei in the tracker materials and which then trigger the ACC and fail the trigger requirement, and more δ-rays are produced with increasing energy and increasing charge, we first study the trigger efficiencies of the neighbouring nuclei. As seen in Figure 3-21, the trigger efficiencies of oxygen, neon, magnesium, and silicon form a nearly linear relationship with charge. Thus the trigger efficiencies of fluorine, sodium, and aluminum can be obtained by the interpolation of the neighbouring nuclei.

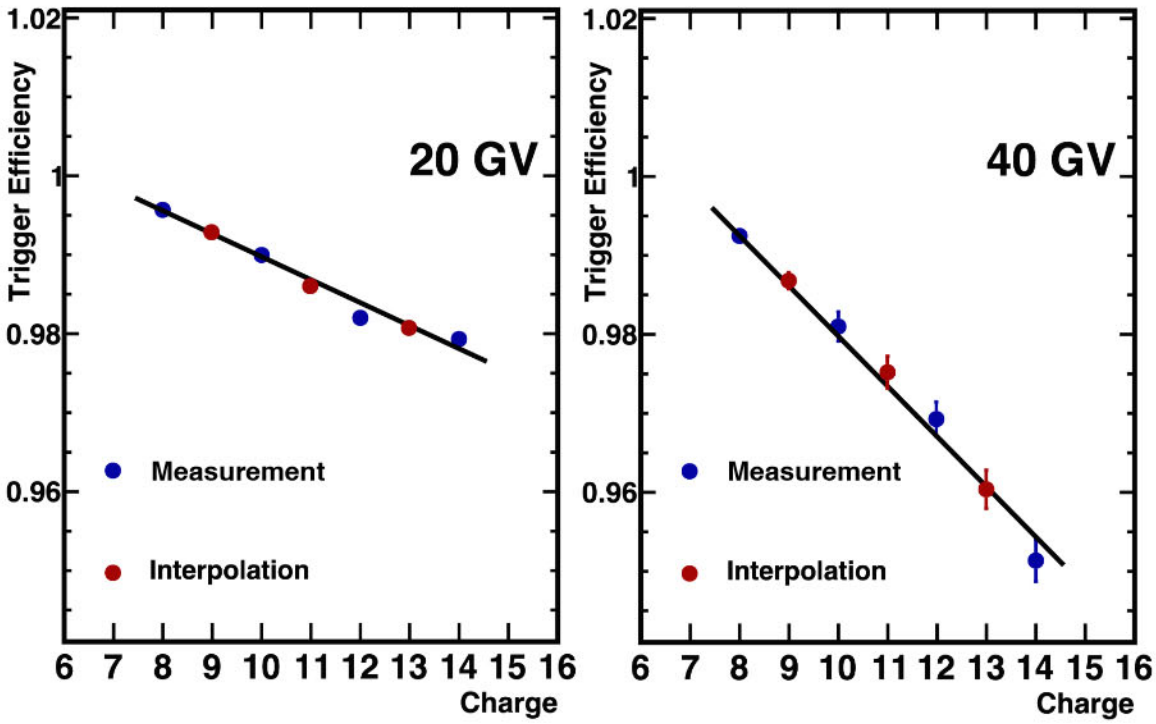

Figure 3-21: The trigger efficiency as a function of charge at 20 GV (left) and 40 GV (right). The blue points are the measured trigger efficiencies of oxygen, neon, magnesium, and silicon. The red points are the trigger efficiencies of fluorine, sodium, and aluminum, obtained by the interpolation of the neighbouring nuclei. Black lines are the linear fits of the blue points.

Figure 3-22 shows the trigger efficiency of sodium as a function of rigidity, interpolated by the measured trigger efficiencies of neon and magnesium. The trigger efficiency has been measured to be $> 95\%$ over the entire rigidity range for fluorine, sodium, and aluminum, where the inefficiency is mostly due to δ-rays produced by incoming nuclei in the tracker materials and which then entered the ACC. The systematic error on the F, Na, and Al fluxes associated with the trigger efficiency measurement is $< 1\%$ over the entire rigidity range.

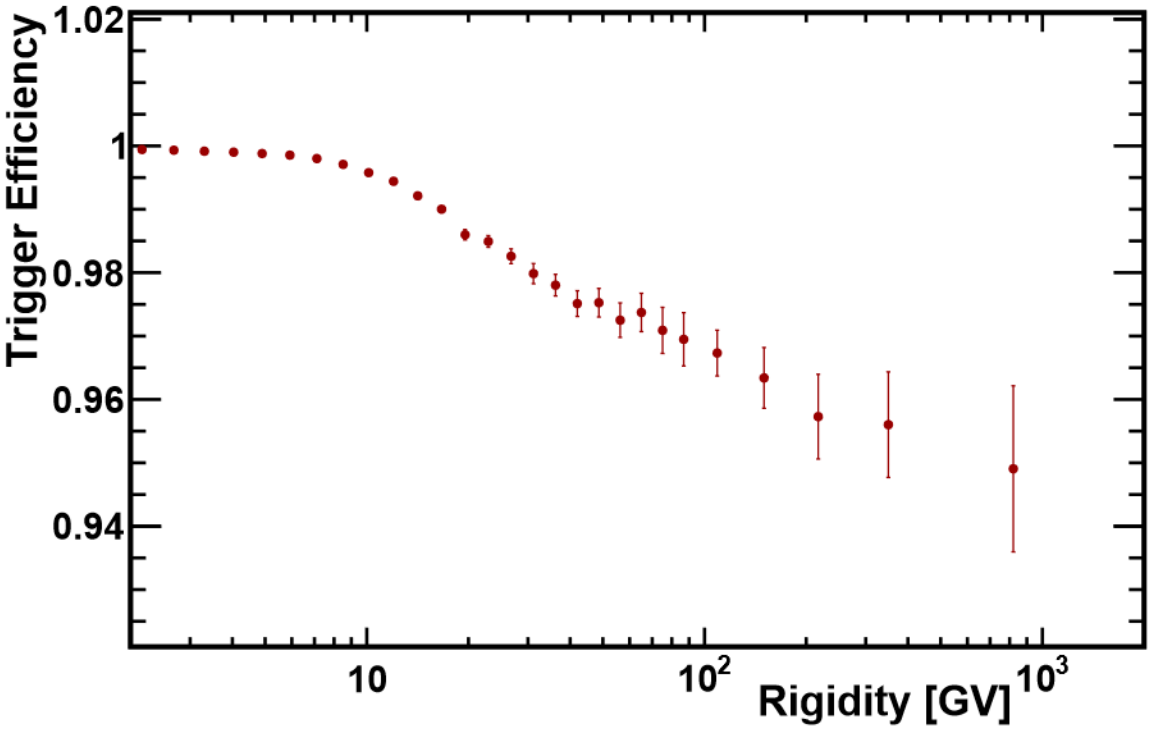

Figure 3-22: The trigger efficiency of sodium as a function of rigidity, evaluated by the interpolation of measured trigger efficiencies of neon and magnesium.

3.7 Tracker Resolution Function and Unfolding of the Flux

Event counts in a given bin of true rigidity may migrate to different bins of reconstructed rigidity. This process is called bin-to-bin migration. This bin-to-bin migration is mainly due to 1) the particle losing energy when traversing the detector

materials (e.g., by ionization); and 2) measurement of rigidity affected by the finite resolution of the tracker.

Particles traversing the detector will deposit their energy via ionization, resulting in a measured rigidity lower with respect to the rigidity at the top of the detector. The effect of energy loss moves events from higher to lower rigidity bins. The mean rate of energy loss is described by the Bethe-Bloch formula [6]

$$-\frac{dE}{dx} = KZ^2\frac{z}{A}\frac{1}{\beta^2}[\frac{1}{2}\ln\frac{2m_ec^2\beta^2\gamma^2T_{max}}{I^2} - \beta^2 - \frac{\delta(\beta\gamma)}{2}] \tag{3.12}$$

which is proportional to Z^2 and dramatically increase in low energy when $\beta\gamma < 3$. Figure 3-23 shows an example of the carbon energy loss in a single tracker layer as a function of $\beta\gamma$.

The tracker rigidity resolution depends on two factors [100]: 1) contribution from measurement error $\sigma_R^M/R = \sqrt{\frac{3}{2}}\frac{8R}{BL^2}\sigma_y$, where B is magnetic field, L is the level arm of the tracker, and σ_y is the tracker coordinate resolution; 2) contribution from multiple scattering $\sigma_R^{MS}/R = 0.045\frac{1}{B\sqrt{LX_0}}$, where X_0 is the radiation length of the tracker material. Multiple scattering of the particles during interaction with the detector material deflects the trajectories of the particles and limits the rigidity resolution at low rigidities (up to tens of GV). At higher rigidities, the dominant effect on rigidity resolution is the coordinate resolution σ_y.

The bin-to-bin migration of events distorts the measured cosmic ray flux and requires an unfolding procedure. Knowledge of the rigidity resolution is the key ingredient in the unfolding. The resolution is obtained from MC and validated with data. One of the verifications is show in Figure 3-24. The differences of the coordinates measured in L3 or L5 to those obtained from the track fit using the measurements from L1, L2, L4, L6, L7, L8, and L9 are compared between data and simulation, and a very good agreement is found. This procedure also directly measures the tracker bending coordinate accuracy of 8 μm for fluorine, 6 μm for sodium, and 7 μm for aluminum.

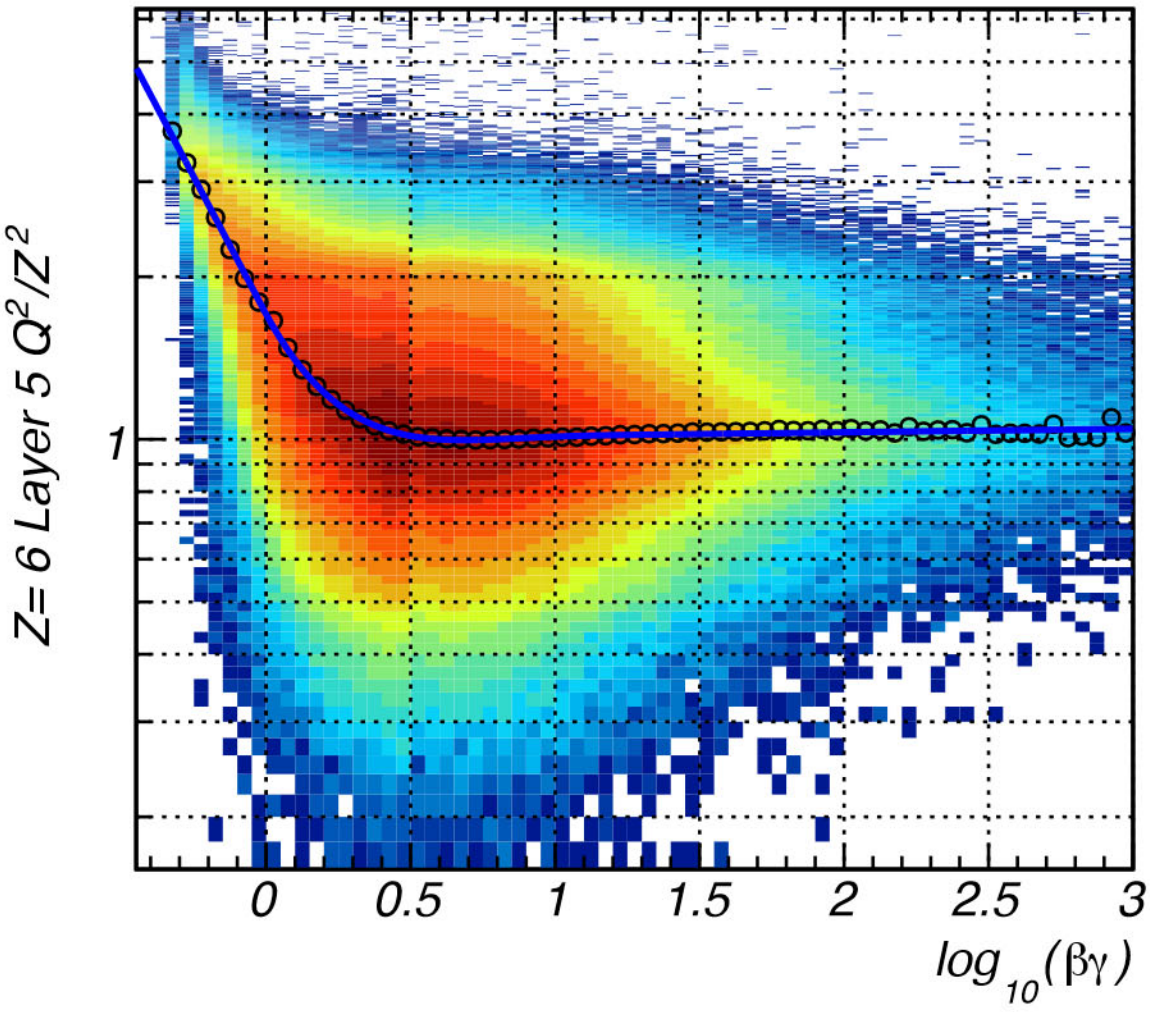

Figure 3-23: Carbon nuclei ionization energy loss in a single tracker layer as a function of $\beta\gamma$. The open black circles correspond to the peak values resulting from fits to the energy deposition in each slice of $\beta\gamma$. The peak profile is then fitted to obtain the final parameterization (blue curve) of the energy dependence. Figure is from Ref. [99].

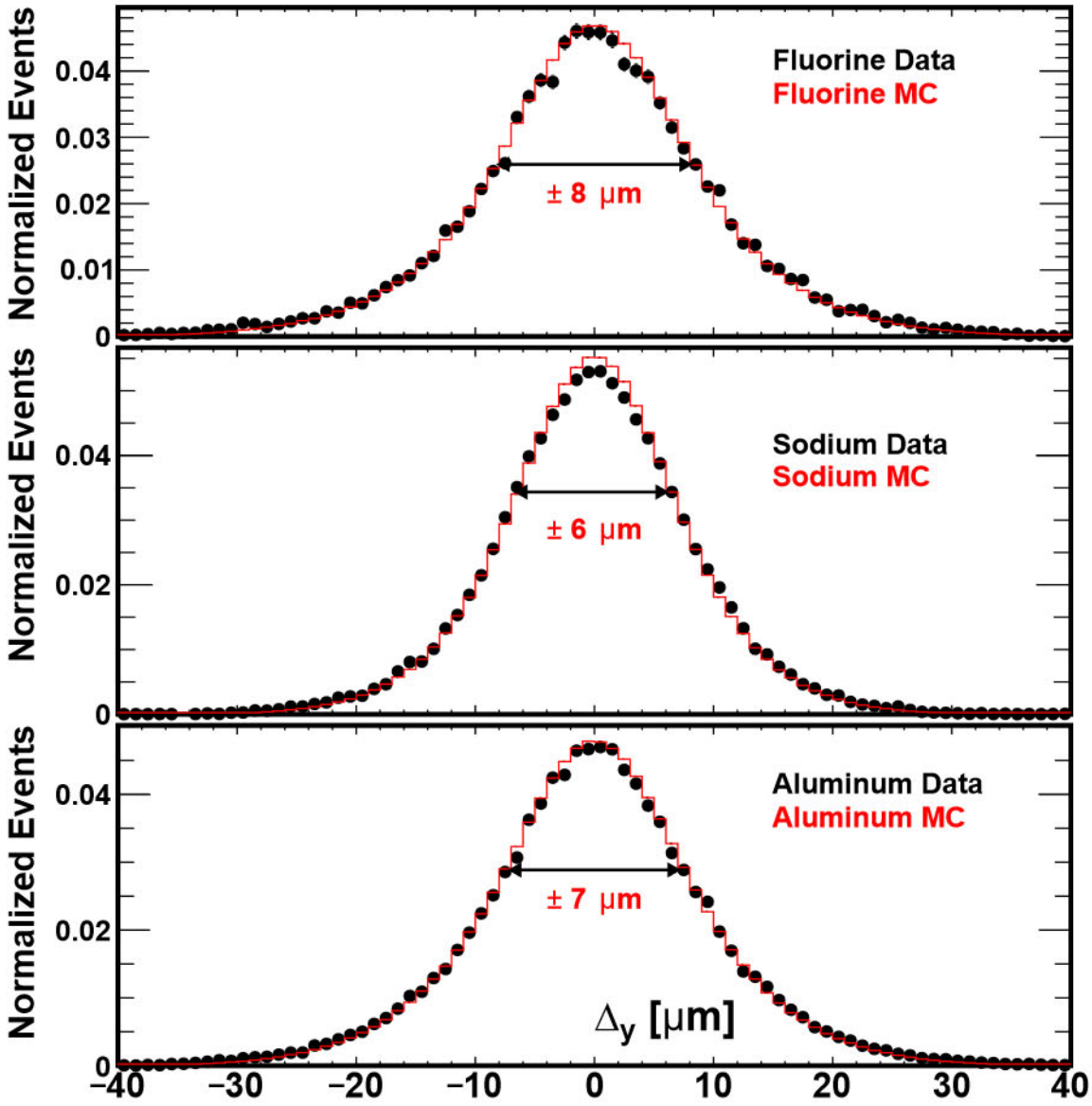

Figure 3-24: The differences Δy of the bending plane y coordinates measured in L3 or L5 to those obtained from the track fit using the measurements from L1, L2, L4, L6, L7, L8, and L9 for data and simulation for fluorine, sodium and aluminum. The measured bending coordinate accuracy is 8 μm for fluorine, 6 μm for sodium, and 7 μm for aluminum.

3.7.1 Tracker Resolution Function

The rigidity resolution function $\Delta\frac{1}{R}$ is evaluated from the difference between the inverse reconstructed rigidity and the inverse true rigidity generated in MC:

$$\Delta\frac{1}{R} = \frac{1}{R_{rec}} - \frac{1}{R_{gen}}. \tag{3.13}$$

The rigidity resolution function $\Delta\frac{1}{R}$ in each generated rigidity bin is parameterized by a double Gaussian core along with an exponentially modified Gaussian tail as

$$f(x = \Delta\frac{1}{R}) = \frac{f_1}{\sqrt{2\pi}\sigma_1} e^{-\frac{(x-\mu)^2}{2\sigma_1^2}} + \frac{f_2}{\sqrt{2\pi}\sigma_2} e^{-\frac{(x-\mu)^2}{2\sigma_2^2}} + \frac{1-f_1-f_2}{2\tau} e^{\frac{\sigma_3+2\tau(\mu-x)}{2\tau^2}} \text{erfc}(\frac{\mu - x + \sigma_3^2/\tau}{\sqrt{2}\sigma_3}) \tag{3.14}$$

where μ is the mean of the three distributions, σ_1 is the sigma of the first Gaussian, f_1 is the fraction of the first Gaussian to the distribution, σ_2 is the sigma of the second Gaussian, f_2 is the fraction of the second Gaussian to the distribution, σ_3 is the sigma of the tail function, and τ is the exponential factor of the tail function. Note that erfc is the complementary error function defined as $\text{erfc}(y) = \frac{2}{\sqrt{\pi}} \int_y^\infty e^{-t^2} dt$. These parameters are then parameterized as function of the generated rigidity to build up a 2D rigidity resolution function $\text{Res}(R_{gen}, \frac{1}{R_{rec}} - \frac{1}{R_{gen}})$, which will be used to describe the rigidity migration effects in the unfolding procedure.

Figure 3-25 illustrates the parameterizations of the rigidity resolution in different rigidity bins for the tracker L1- L8 configuration. Below 20 GV, the peak is shifted to lower reconstructed rigidities because of the energy losses, while the tail is mostly coming from multiple scattering; at intermediate rigidities, 20-100 GV, the peak is centered at zero and the distribution becomes more and more symmetric, the tail of the multiple scattering vanishes, while the tails due to the intrinsic spatial resolution appear; at higher rigidities, the distribution is symmetric.

Figure 3-26 shows the complete AMS rigidity resolution function as smearing matrices for the tracker L1- L8 and L1-L9 configurations.

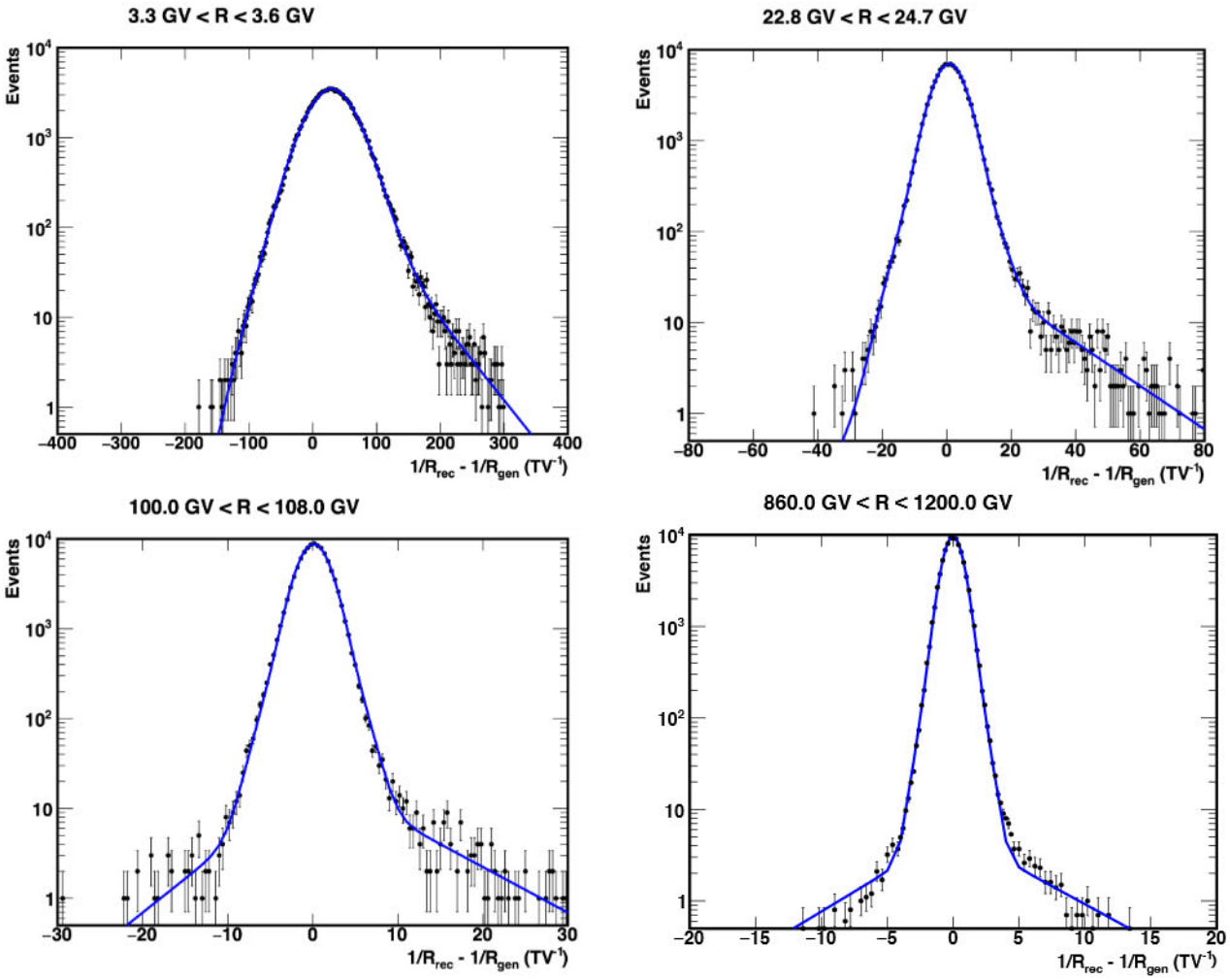

Figure 3-25: Examples of rigidity resolution parameterizations, using sodium sample in different rigidity ranges for the tracker L1- L8 configuration.

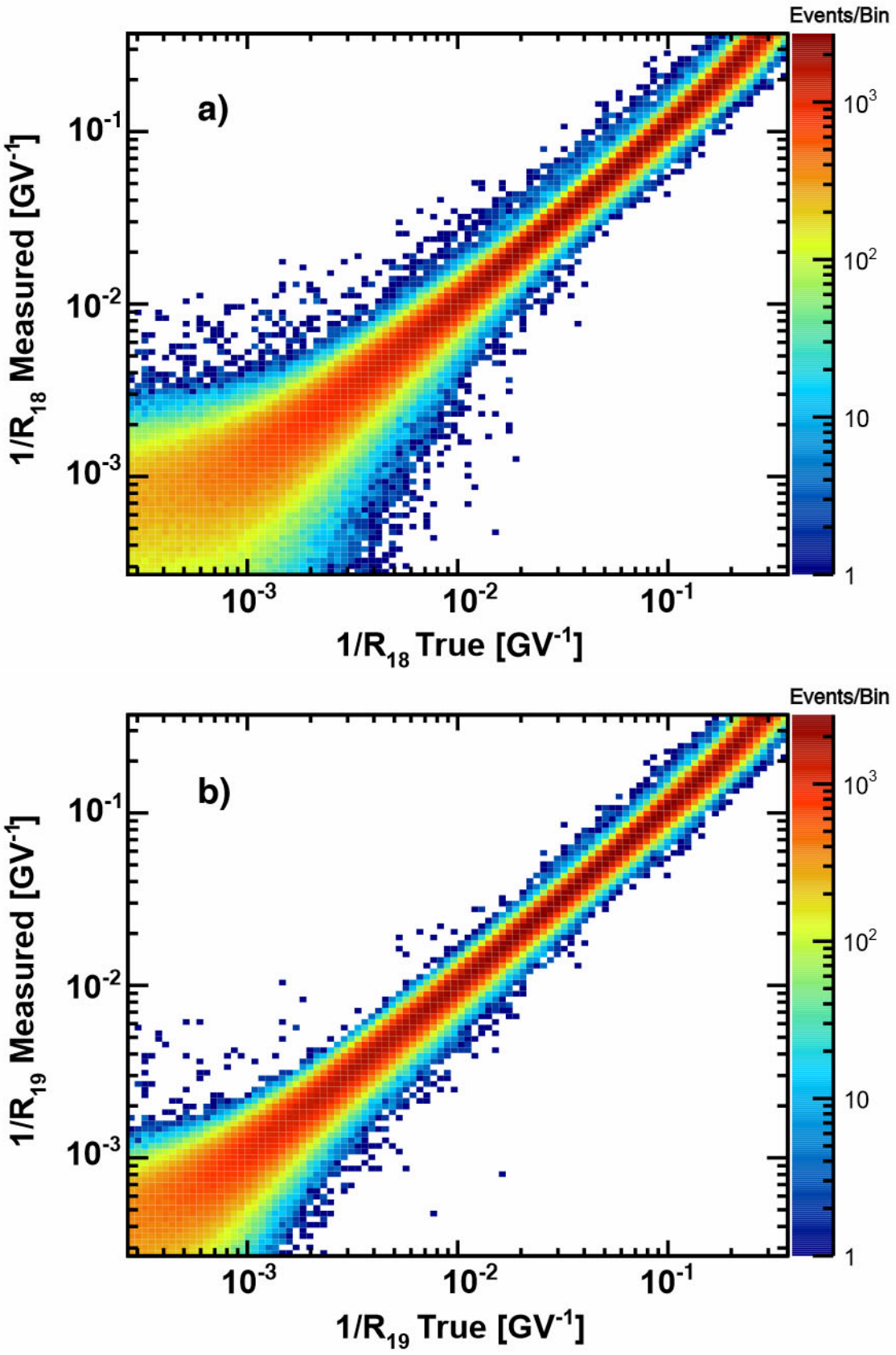

Figure 3-26: The AMS rigidity resolution smearing matrices for the tracker a) L1- L8 and b) L1-L9 configurations.

3.7.2 Forward Unfolding Method

In this analysis, the Forward Unfolding Method [101] is used for the unfolding of the flux.

With an initial true flux model $\Phi_t(\frac{1}{R_{gen}})$, the folded event rate $f_i^{cal}(\frac{1}{R_{gen}})$ in the i_{th} inverted reconstructed rigidity bin can be calculated by

$$f_i^{cal}(\frac{1}{R_{rec}}) = \frac{1}{\Delta R_{rec}} \int_{\frac{1}{R_i}}^{\frac{1}{R_i}+\Delta\frac{1}{R_i}} \int_0^{+\infty} \Phi_t(\frac{1}{R_{gen}}) Res(R_{gen}, \frac{1}{R_{rec}} - \frac{1}{R_{gen}}) A_{eff}(\frac{1}{R_{gen}}) d\frac{1}{R_{gen}} d\frac{1}{R_{rec}} \tag{3.15}$$

where $A_{eff}(\frac{1}{R_{gen}})$ is the effective acceptance calculated in the inverse reconstructed rigidity bin. The measured event rate $f_i^{rec}(\frac{1}{R_{rec}})$ is

$$f_i^{rec}(\frac{1}{R_{rec}}) = \frac{N_i^{rec}(\frac{1}{R_{rec}})}{T_i(\frac{1}{R_{rec}})} \tag{3.16}$$

where N_i^{rec} is the number of events after background subtraction. Then the true flux Φ_T can be obtained by minimizing

$$\chi^2 = \sum_{i=1}^{n_{bin}} (\frac{f_i^{rec} - f_i^{cal}}{\sigma_i})^2 \tag{3.17}$$

where σ_i is the the statistical error of the measured event rate N_i/T_i. After the true flux is obtained, the unfolding factor C_i defined as the ratio between folded and unfolded event rates, is calculated from

$$C_i = \frac{f_{i,rec}^{cal}}{f_{i,gen}^{cal}} = \frac{\int_{\frac{1}{R_i}}^{\frac{1}{R_i}+\Delta\frac{1}{R_i}} \int_0^{+\infty} \Phi_T(\frac{1}{R_{gen}}) Res(R_{gen}, \frac{1}{R_{rec}} - \frac{1}{R_{gen}}) A_{eff}(\frac{1}{R_{gen}}) d\frac{1}{R_{gen}} d\frac{1}{R_{rec}}}{\int_{\frac{1}{R_i}}^{\frac{1}{R_i}+\Delta\frac{1}{R_i}} \Phi_T(\frac{1}{R_{gen}}) A_{eff}(\frac{1}{R_{gen}}) d\frac{1}{R_{gen}}}. \tag{3.18}$$

Figure 3-27 presents the rigidity dependence of the unfolding factor C for fluorine, sodium, and aluminum. The dip around 1 TV is due to the requirement of track passing through L9 above 1.2 TV.

At low rigidity, up to ∼20 GV, the effect of migration is mostly due to energy losses and multiple scattering. This steadily becomes less significant up to around

100 GV. Then the unfolding factor increases with rigidity again resulting from finite coordinate resolution.

As discussed in Section 3.7.1, the rigidity resolution function has a double Gaussian core and an exponentially modified Gaussian tail. The systematic error on the fluxes due to the rigidity resolution functions can be estimated by repeating the unfolding procedure while varying the width of the Gaussian cores of the resolution function by 5% and by independently varying the amplitude of the non-Gaussian tails by 10%.

The resulting systematic error on the F flux is less than 1% below 200 GV and smoothly increasing to 7% at 2.9 TV. The resulting systematic error is 3.5% at 2 GV, <1% from 3 GV to 300 GV for both Na and Al fluxes and increases smoothly to 5% for Na and 4% for Al at 3.0 TV.

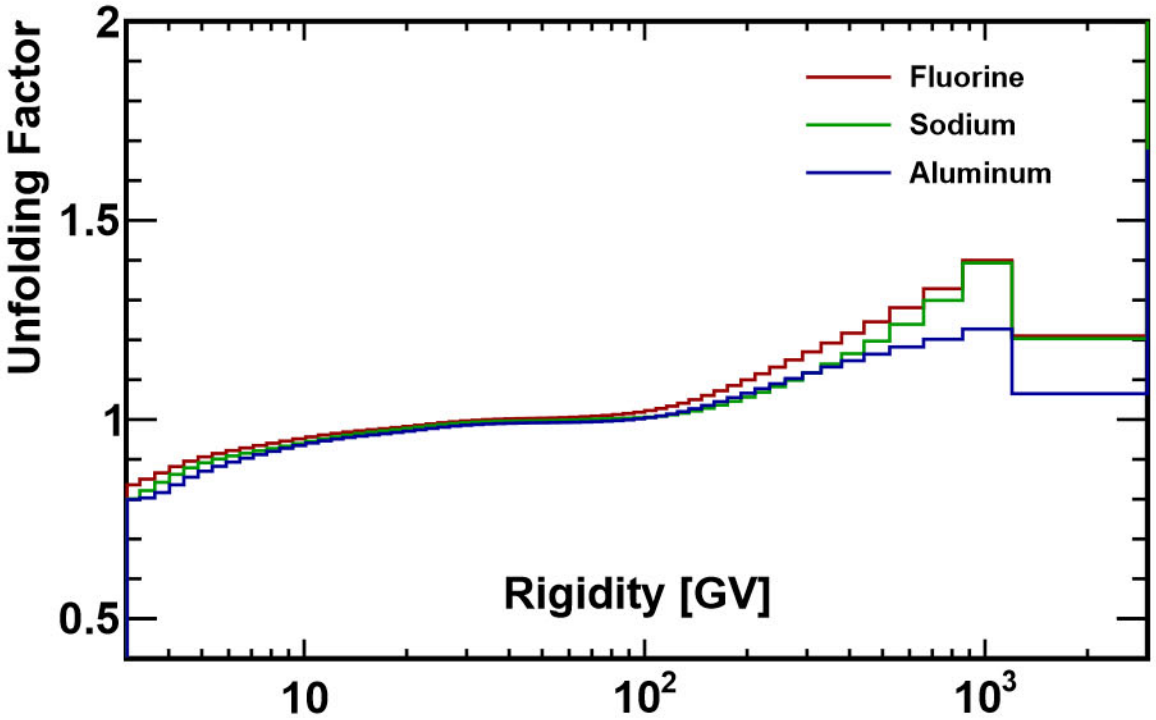

Figure 3-27: The rigidity dependence of the unfolding factor for fluorine (red), sodium (green), and aluminum (blue).

3.8 Systematic Error

The systematic errors include the uncertainties in the trigger efficiency, the acceptance calculation, the background subtraction, and the rigidity resolution function, which have been discussed above. In addition, two more systematic errors on geomagnetic cutoff factors and absolute rigidity scale were studied.

3.8.1 Geomagnetic Cutoff

The systematic error associated with the geomagnetic cutoff below 30 GV arises from the selection of the geomagnetic cutoff factor of 1.2. To evaluate the corresponding systematic errors, the geomagnetic cutoff factor is varied from 1.0 to 1.4, resulting in a negligible systematic uncertainty ($< 0.1\%$) in the rigidity range below 30 GV for F, Na and Al fluxes.

3.8.2 Absolute Rigidity Scale

There are two contributions to the systematic uncertainty on the rigidity scale. The first is due to residual tracker misalignment. This error is estimated from data by the comparison of the inverse absolute rigidity $1/|R|$ measured by the tracker, with the inverse energy $1/E$ measured by the ECAL, for positron events and electron events. It is found to be $1/30$ TV^{-1} [76], limited mostly by available positron statistics.

The second systematic error on the rigidity scale arises from the magnetic field map measurement (0.25%) and its temperature corrections (0.1%) [102].

The corresponding systematic errors on the fluxes are obtained by repeating the unfolding procedure with rigidity scale shifts of $R^{-1} \pm 1/30$ TV^{-1} and $R(1 \pm 0.27\%)$. The variations caused by these rigidity shifts are taken as systematic error.

The error on the F flux due to uncertainty on the rigidity scale is $< 1\%$ up to 200 GV and increases smoothly to 6.5% at 2.9 TV. The corresponding errors on Na and Al fluxes amount to $<0.4\%$ up to 100 GV for both Na and Al fluxes, increasing smoothly to 7% for Na and 6% for Al at 3.0 TV.

The systematic errors on the tracker misalignment and magnetic field map uncertainties are added in quadrature to arrive at the total rigidity scale systematic errors.

3.9 Total Error

The contributions to the systematic uncertainty from different sources for fluorine, sodium, and aluminum are shown in Figure 3-28, Figure 3-29, and Figure 3-30 respectively. The total error is obtained by propagating the various sources of systematic errors and adding them in quadrature, including also the statistical error. The total error is at the level of 5% for all nuclei up to ∼100 GV, dominated by systematics, while at high rigidity the total error is dominated by the statistics.

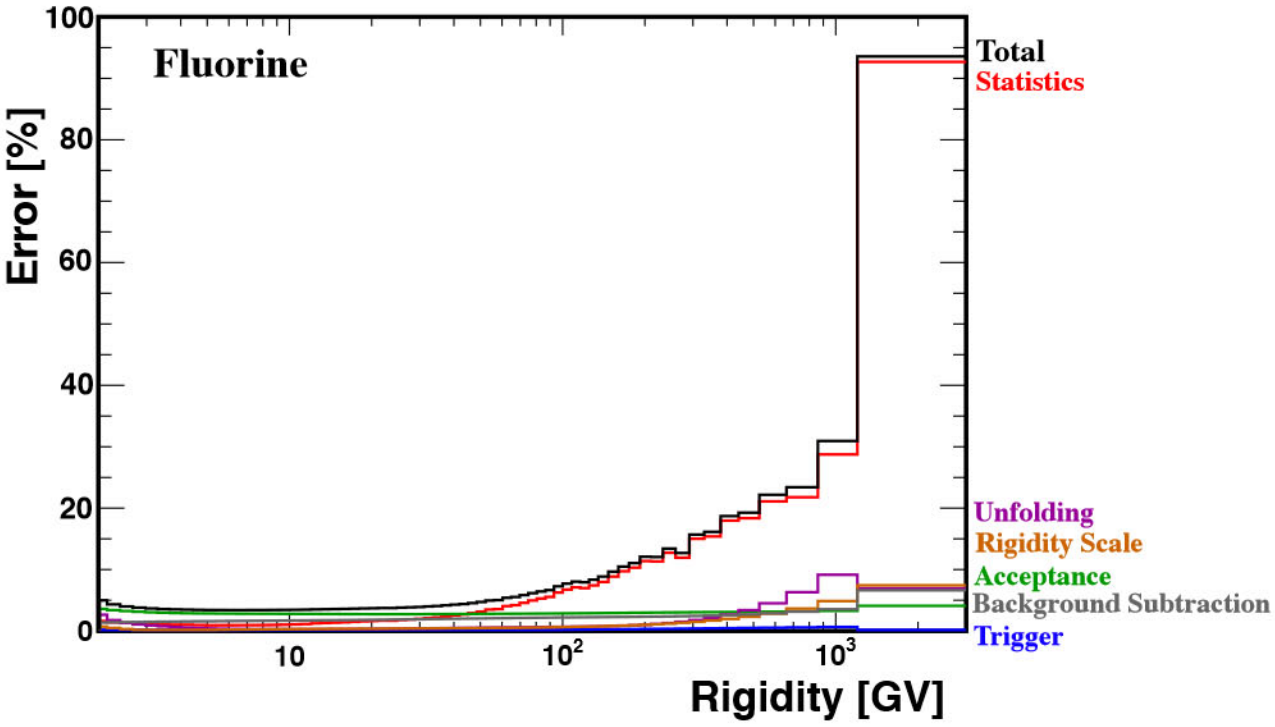

Figure 3-28: Total flux error as a function of rigidity for fluorine flux measurement, along with the breakdown of its components. All the constituent uncertainties are added in quadrature to arrive at the total error.

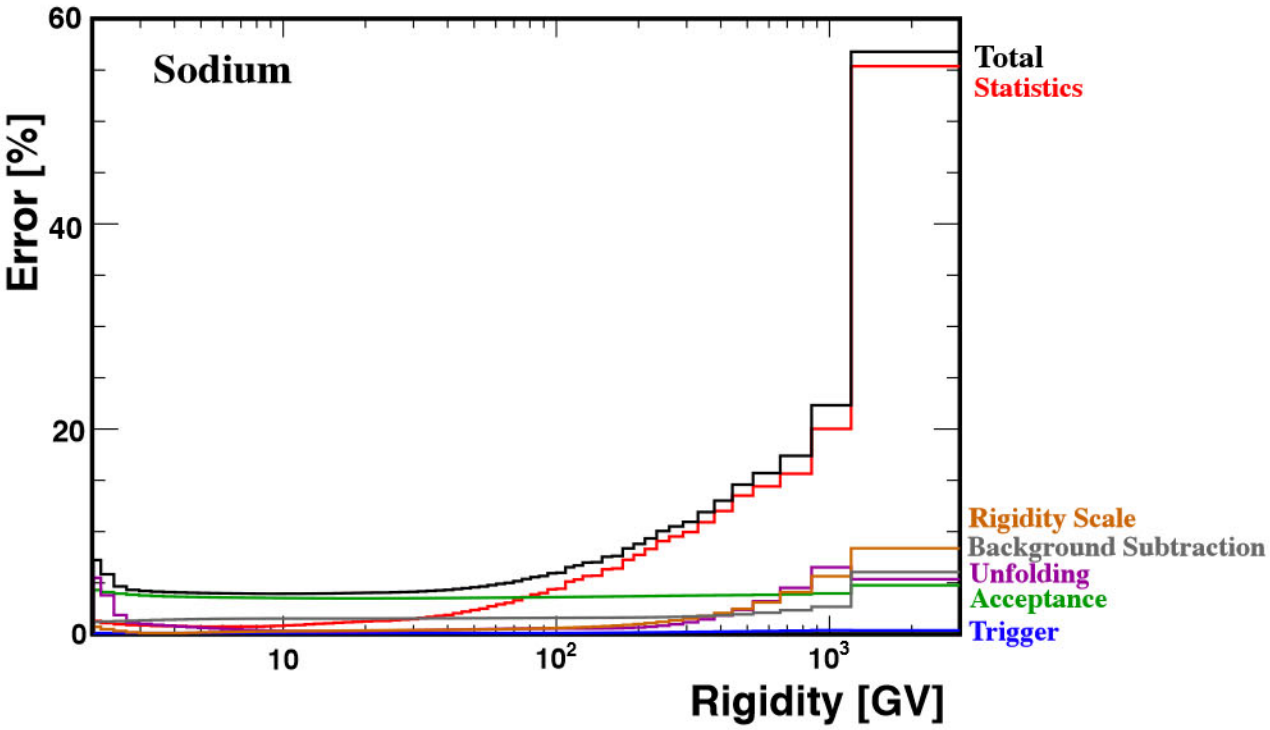

Figure 3-29: Total flux error as a function of rigidity for sodium flux measurement, along with the breakdown of its components. All the constituent uncertainties are added in quadrature to arrive at the total error.

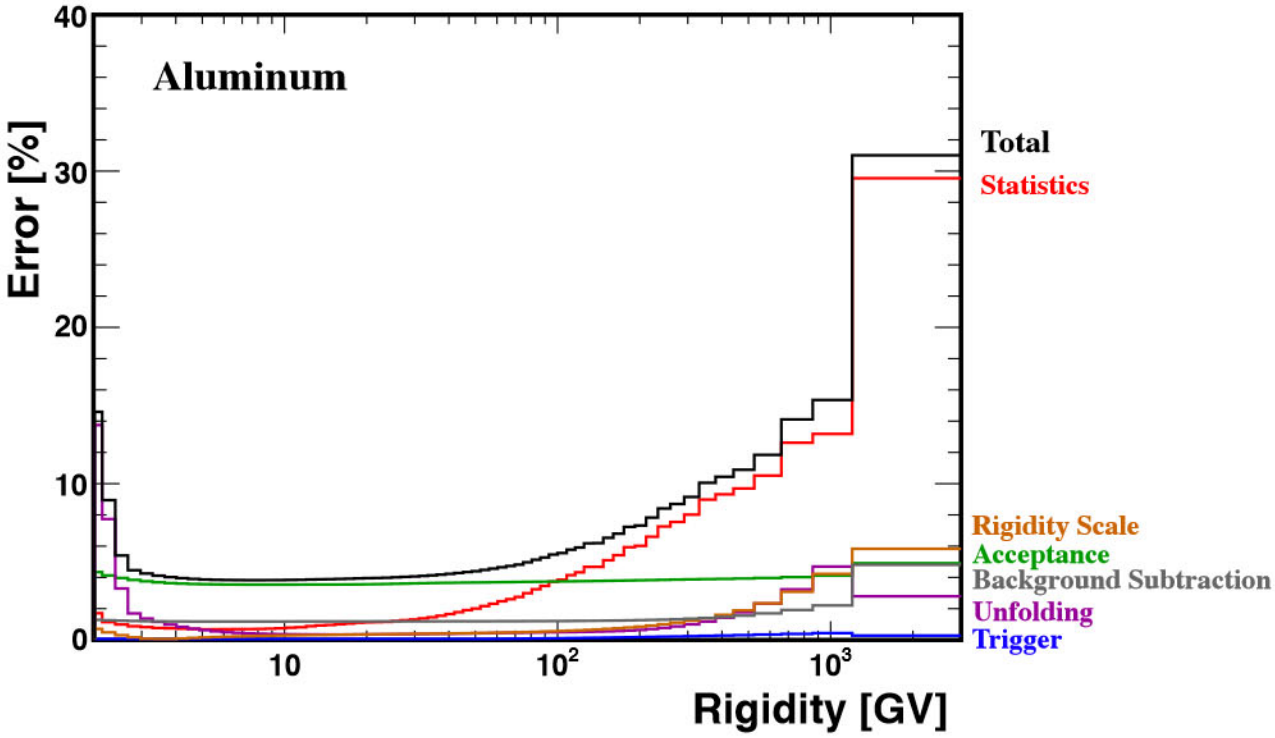

Figure 3-30: Total flux error as a function of rigidity for aluminum flux measurement, along with the breakdown of its components. All the constituent uncertainties are added in quadrature to arrive at the total error.

Chapter 4

Results

4.1 The Fluorine Flux and the Fluorine to Silicon Ratio

In the previous chapter, the measurements of the fluorine F events collected by AMS (N_F), the exposure time (T), the trigger efficiency (ε_F) and the effective acceptance (A_F), together with their relative uncertainties, have been evaluated. The flux is measured in 49 bins from 2.15 GV to 2.9 TV. By means of Eq. (3.1), they have been used to calculate the flux of fluorine.

Figure 4-1 shows the F flux as a function of rigidity $\tilde{R}$ with the total errors, the sum in quadrature of statistical and systematic errors. In this and subsequent figures, the data points are placed along the abscissa at $\tilde{R}$ calculated for a flux $\propto R^{-2.7}$ [103]. For comparison, Figure 4-1 also shows the AMS results on the boron B flux [60]. As seen, at high rigidities, the rigidity dependences of the F and B fluxes are identical; at low rigidities, they are different.

To examine the rigidity dependence of the F flux, the variation of the flux spectral index γ with rigidity was obtained in a model-independent way from

$$\gamma = d[\log(\Phi)]/d[\log(R)]. \tag{4.1}$$

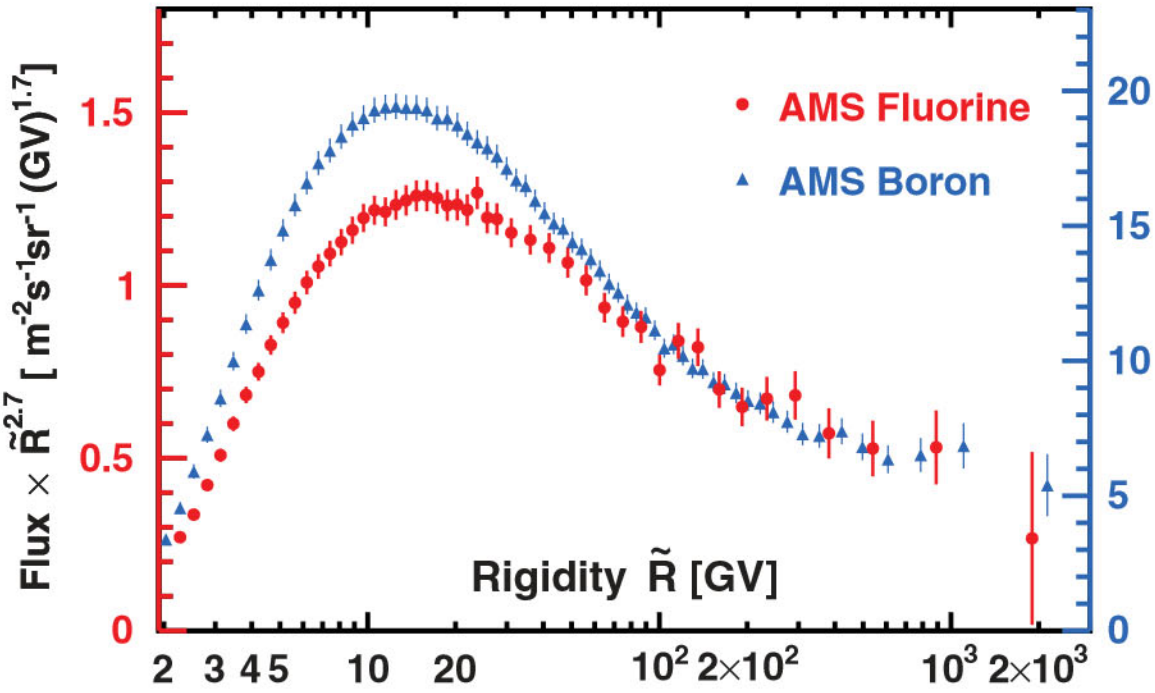

Figure 4-1: The AMS F flux multiplied by $\tilde{R}^{2.7}$ with total errors as a function of rigidity (red points and left axis) together with the AMS B flux [60] (blue points and right axis).

over non-overlapping rigidity intervals bounded by 7.09, 12.0, 16.6, 28.8, 45.1, 175.0, and 2900.0 GV. The results are presented in Figure 4-2 together with the B spectral index [60].

As seen in Figure 4-2, in the rigidity interval 175–2900 GV, the F spectral index is similar to the B spectral index. In particular, both fluxes harden above $\sim$ 200 GV.

To directly compare the rigidity dependence of the F flux with that of the light secondary cosmic ray B flux [60], the ratio of the F flux to the B flux, $\frac{\Phi_F}{\Phi_B}$, is computed. To establish the rigidity interval where the F and B fluxes may have identical rigidity dependence, the F/B flux ratio above 7 GV has been fit with

$$\frac{\Phi_F}{\Phi_B} = \begin{cases} \kappa(R/R_0)^{\Delta}, & R \leq R_0, \\ \kappa, & R > R_0. \end{cases} \tag{4.2}$$

The fit yields $\kappa = 0.078 \pm 0.003$, $R_0 = 150 \pm 60$ GV, and $\Delta = 0.083 \pm 0.007$ with a χ^2/d.o.f. = 19/33. Figure 4-3 shows the AMS F/B flux ratio as a function of

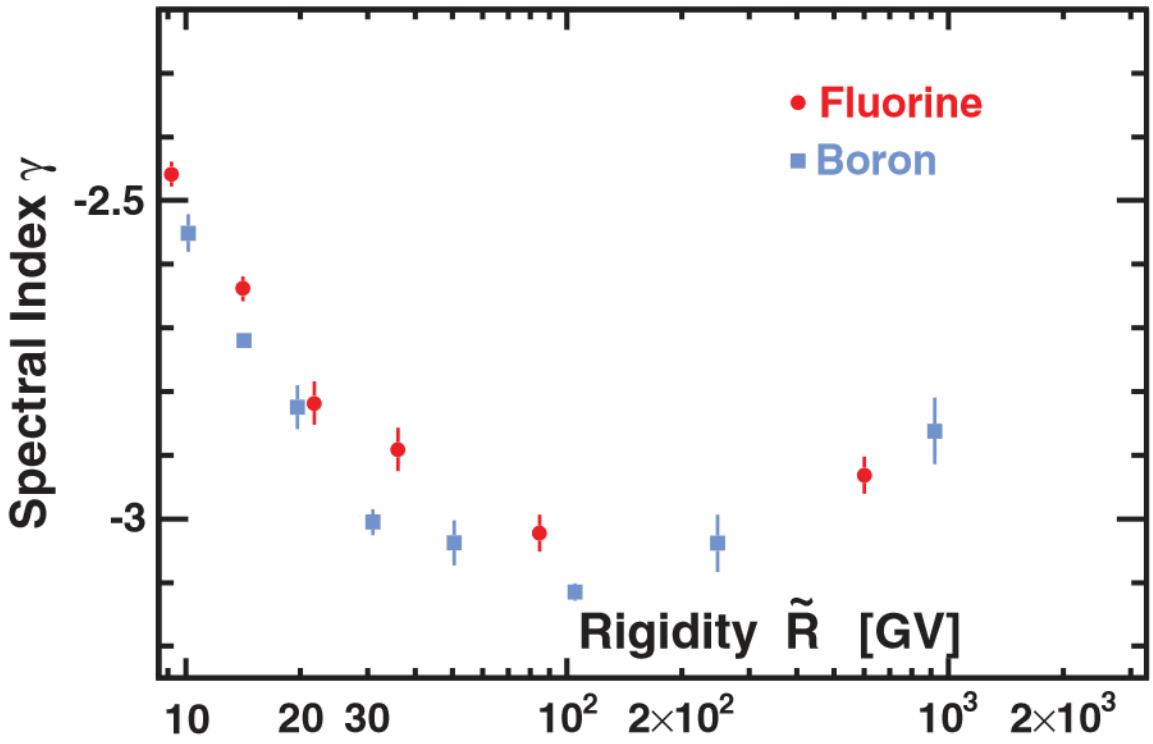

Figure 4-2: The AMS F spectral index (red points) together with the B spectral index (blue points) as a function of rigidity.

rigidity with total errors together with the fit results. As seen, above 150 ± 60 GV, the rigidity dependences of the F and B fluxes are identical, and at lower rigidities they are different. As shown in Figure 4-4, the F/B ratio does not change with time from 5 to 20 GV; i.e., solar modulation of the F/B flux ratio does not affect the fit results with Eq. (4.2). Note that fitting the F/B ratio with Eq. (4.2) above 20 GV does not change the fit results. Above 20 GV, the fit yields $\kappa = 0.078 \pm 0.003$, $R_0 = 145 \pm 65$ GV, and $\Delta = 0.084 \pm 0.014$ with a χ^2/d.o.f. = 16/21.

Figure 4-5 shows the AMS F flux as a function of kinetic energy per nucleon E_k together with earlier measurements [50, 54–57]. Data from other experiments are extracted using Ref. [58]. The F flux is expressed as a function of kinetic energy per nucleon E_k using

$$E_K = \left(\sqrt{Z^2\tilde{R}^2 + M^2} - M\right)/A \tag{4.3}$$

with Z the charge, M the mass, and A the atomic mass number. The rigidity is converted to E_k assuming that the sample is entirely ^{19}F.

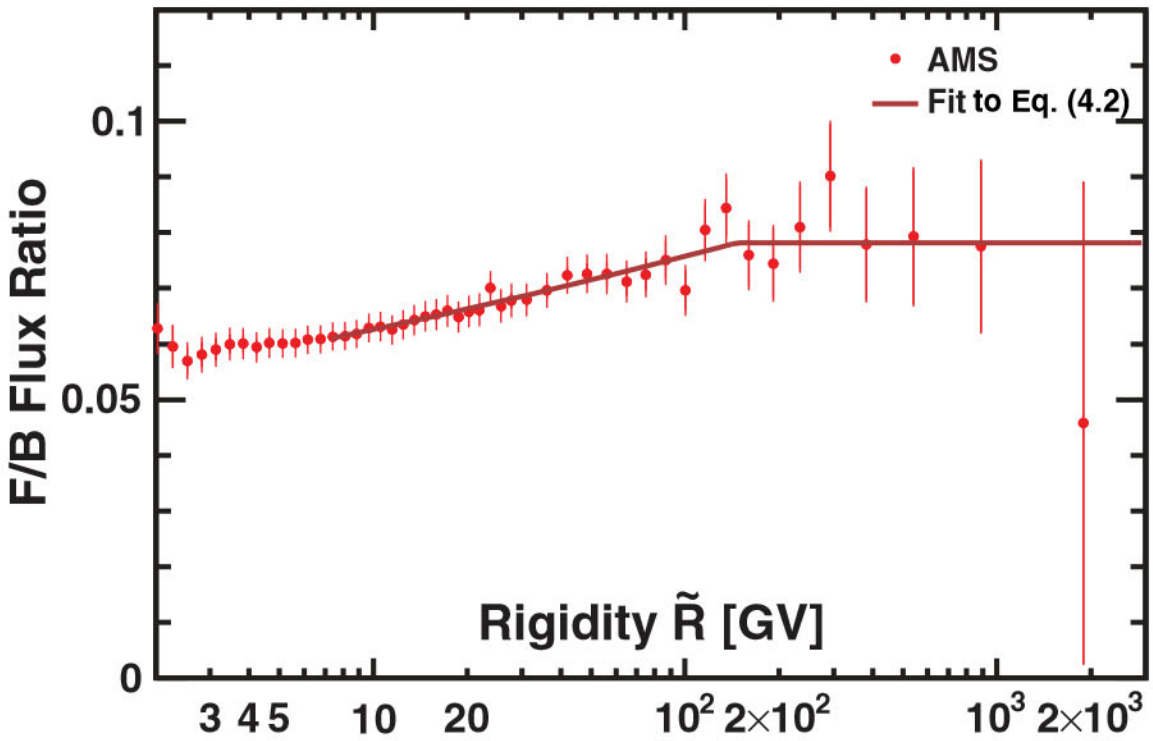

Figure 4-3: The AMS F/B flux ratio with total errors as a function of rigidity. The brown curve shows the fit results with Eq. (4.2).

To compare the rigidity dependence of the F flux with that of the Ne, Mg, and Si primary cosmic ray fluxes, which have an identical rigidity dependence above 80.5 GV [63], the ratio of the F flux to the characteristic heavy primary Si flux, F/Si was calculated. Figure 4-6 shows the AMS F/Si flux ratio as a function of rigidity together with the AMS B/O flux ratio [60].

The variation with rigidity of the spectral index Δ of the F/Si flux ratio was obtained by fitting it with

$$\frac{\Phi_{\mathrm{F}}}{\Phi_{\mathrm{Si}}} = \begin{cases} C(R/175GV)^{\Delta_1}, R \leq 175GV, \\ C(R/175GV)^{\Delta_2}, R > 175GV. \end{cases} \tag{4.4}$$

over the rigidity interval [28.8-2900] GV. The fitted values are $C^{\mathrm{F/Si}} = 0.044 \pm 0.001$, $\Delta_1^{\mathrm{F/Si}} = -0.34 \pm 0.02$, and $\Delta_2^{\mathrm{F/Si}} = -0.19 \pm 0.07$ with a χ^2/d.o.f. = 13/16. Above 175 GV, the spectral index $\Delta^{\mathrm{F/Si}}$ exhibits a hardening $(\Delta_2^{\mathrm{F/Si}} - \Delta_1^{\mathrm{F/Si}})$ of 0.15 ± 0.07, compatible with the AMS result on the hardening of the Li/C, Be/C, B/C, Li/O,

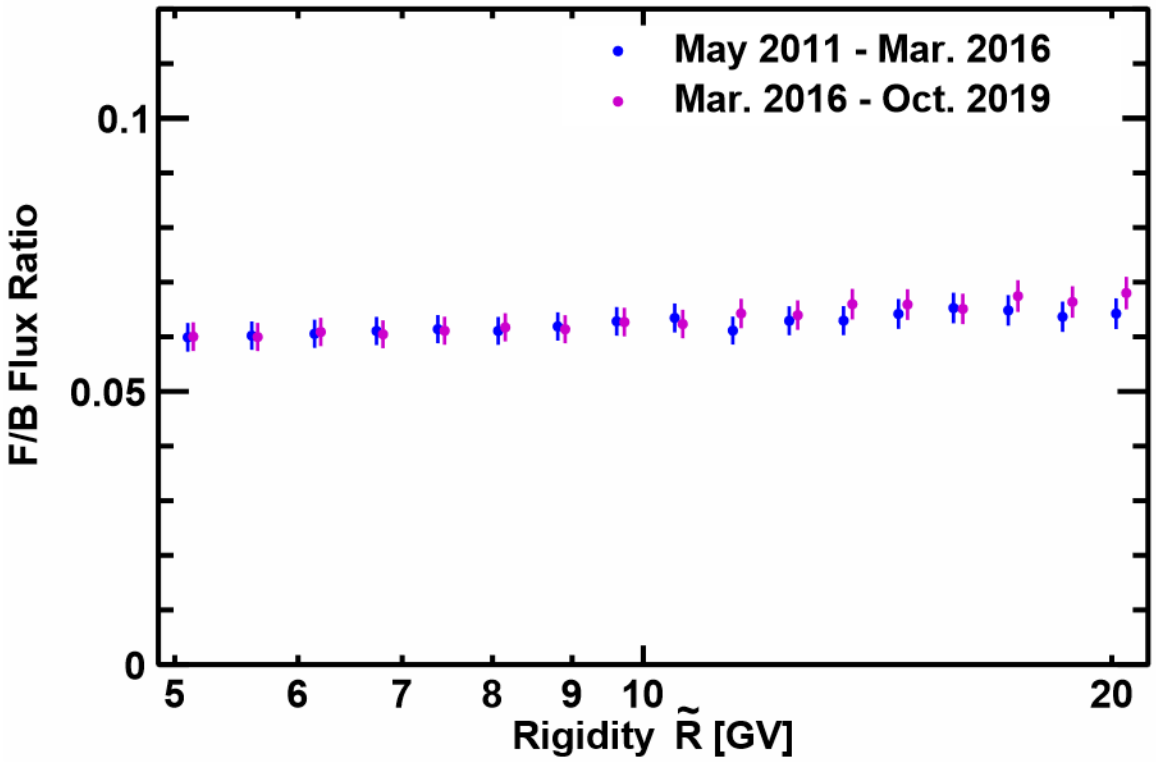

Figure 4-4: The AMS F/B flux ratio from 5 to 20 GV for two different time periods, May 19, 2011 to March 3, 2016 (blue dots) and March 3, 2016 to October 30, 2019 (magenta dots). For clarity, the data points are displaced horizontally.

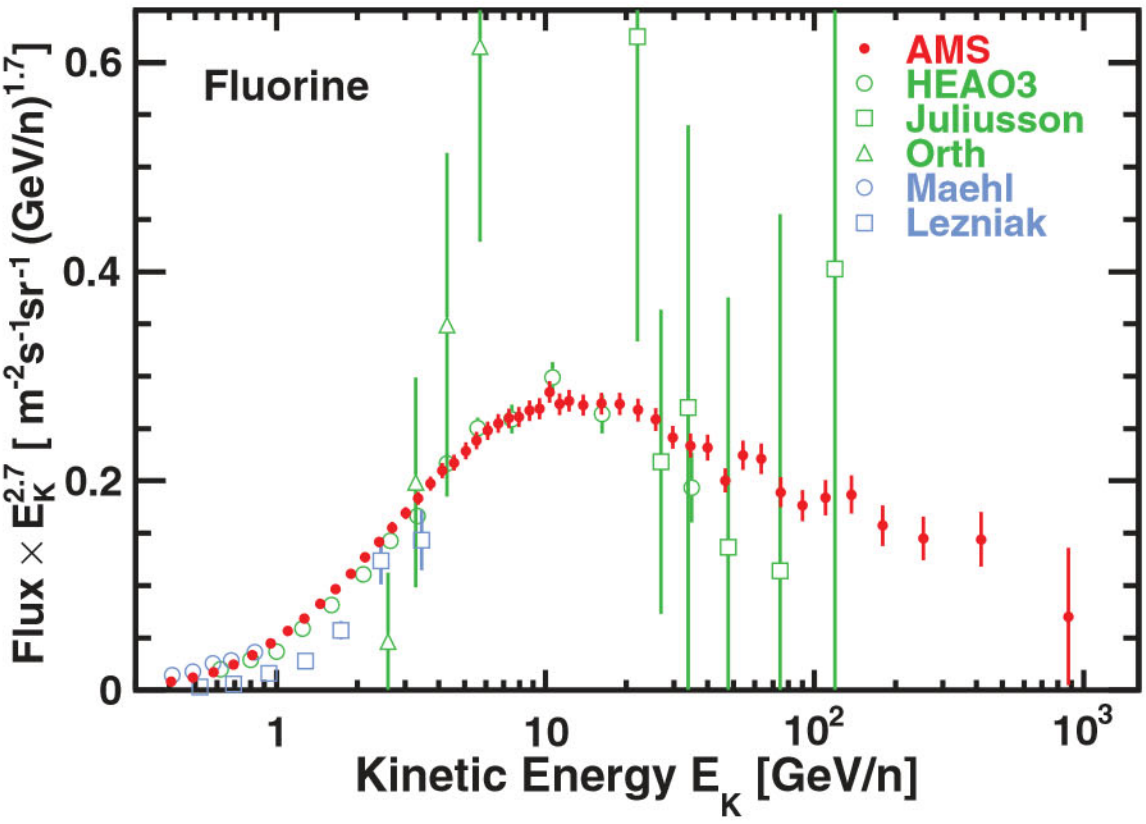

Figure 4-5: The AMS fluorine flux as a function of kinetic energy per nucleon E_k multiplied by $E_k^{2.7}$ together with earlier measurements [50, 54–57].

Be/O, and B/O flux ratios by 0.140 ± 0.025 [60].

To ensure that the choice of the inflection point of 175 GV does not affect the fit results, the inflection point (R_0) is allowed to vary. The F/Si ratio is fitted with

$$\frac{\Phi_{\rm F}}{\Phi_{\rm Si}} = \begin{cases} C(R/R_0)^{\Delta_1}, R \leq R_0, \\ C(R/R_0)^{\Delta_2}, R > R_0. \end{cases} \tag{4.5}$$

over the rigidity interval [28.8-2900] GV. The fitted values are $C^{\rm F/Si} = 0.046 \pm 0.001$, $\Delta_1^{\rm F/Si}$ = -0.35 ± 0.03, $\Delta_2^{\rm F/Si}$ = -0.21 ± 0.08, and R_0 = 150 ± 61 GV with a χ^2/d.o.f. = 13/15. So above 150 ± 61 GV, the spectral index of the F/Si ratio exibits a hardening ($\Delta_2^{\rm F/Si} - \Delta_1^{\rm F/Si}$) of 0.14 ± 0.08, in complete agreement with results of Eq. (4.4), ($\Delta_2^{\rm F/Si} - \Delta_1^{\rm F/Si}$) = 0.15 ± 0.07.

Figure 4-6 also shows the AMS F/Si fit results with Eq. (4.4) together with the predictions of the cosmic ray propagation model GALPROP [104] and of the latest GALPROP-HELMOD model [23] on the F/Si flux ratio and the AMS B/O fit results with Eq. (4.4), $C^{\rm B/O} = 0.097 \pm 0.003$, $\Delta_1^{\rm B/O}$ = -0.405 ± 0.005, and $\Delta_2^{\rm B/O}$ = -0.26 ± 0.03 with a χ^2/d.o.f. = 24/36.

To compare the rigidity dependence of the F/Si flux ratio with the lighter secondary-to-primary B/O flux ratio in detail, the [(F/Si)/(B/O)] ratio is computed and shown in Figure 4-7. Over the entire rigidity range, [(F/Si)/(B/O)] can be fitted with

$$\frac{\Phi_{\rm F}/\Phi_{\rm Si}}{\Phi_{\rm B}/\Phi_{\rm O}} = \begin{cases} k(R/R_0)^{\delta_1}, R \leq R_0, \\ k(R/R_0)^{\delta}, R > R_0. \end{cases} \tag{4.6}$$

The fit results are k = 0.39 ± 0.01, R_0 = 9.8 ± 0.9 GV, δ_1 = -0.055 ± 0.013, and δ = 0.052 ± 0.007 with a χ^2/d.o.f. = 24/45. As seen, the rigidity dependences of the F/Si and B/O flux ratios are distinctly different. Most importantly, the latest AMS result shows that above 10 GV, the [(F/Si)/(B/O)] ratio can be described by a single power law function $\propto R^{\delta}$ with $\delta = 0.052 \pm 0.007$ (a 7σ difference from 0). This shows, unexpectedly, that the heavier secondary-to-primary F/Si flux ratio rigidity

dependence is distinctly different from the lighter B/O (or B/C) rigidity dependence, indicating that the propagation properties of heavy cosmic rays, from F to Si, are different from those of light cosmic rays, from He to O.

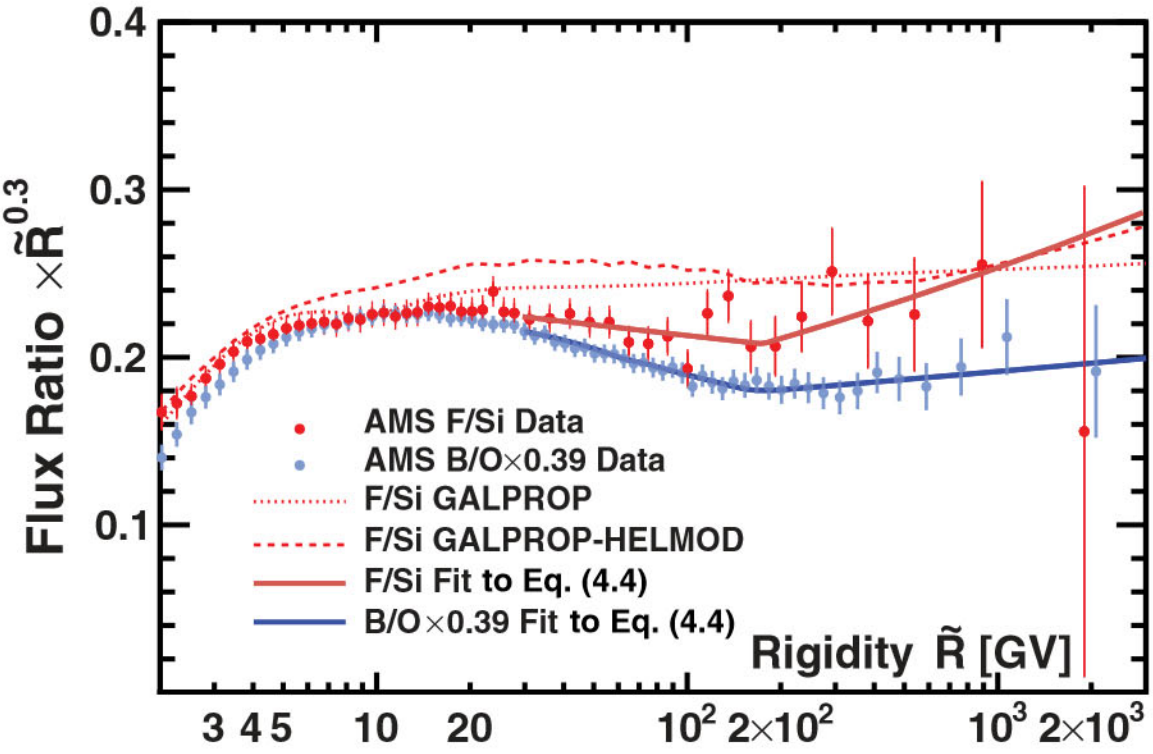

Figure 4-6: The AMS F/Si flux ratio (red dots) and AMS B/O flux ratio (blue dots) multiplied by $\tilde{R}^{0.3}$ with total errors as a function of rigidity. For display purposes, the B/O flux ratio is rescaled as indicated. The solid brown and blue curves show the F/Si and B/O fit results respectively with Eq. (4.4). The dotted and dashed red curves show the predictions of the F/Si ratio by the GALPROP model [104] and the GALPROP-HELMOD [23] model, respectively.

As shown in Figure 4-8, the [(F/Si)/(B/O)] ratio does not change with time below 20 GV; i.e., solar modulation on the [(F/Si)/(B/O)] ratio does not affect the fit results with Eq. (4.6).

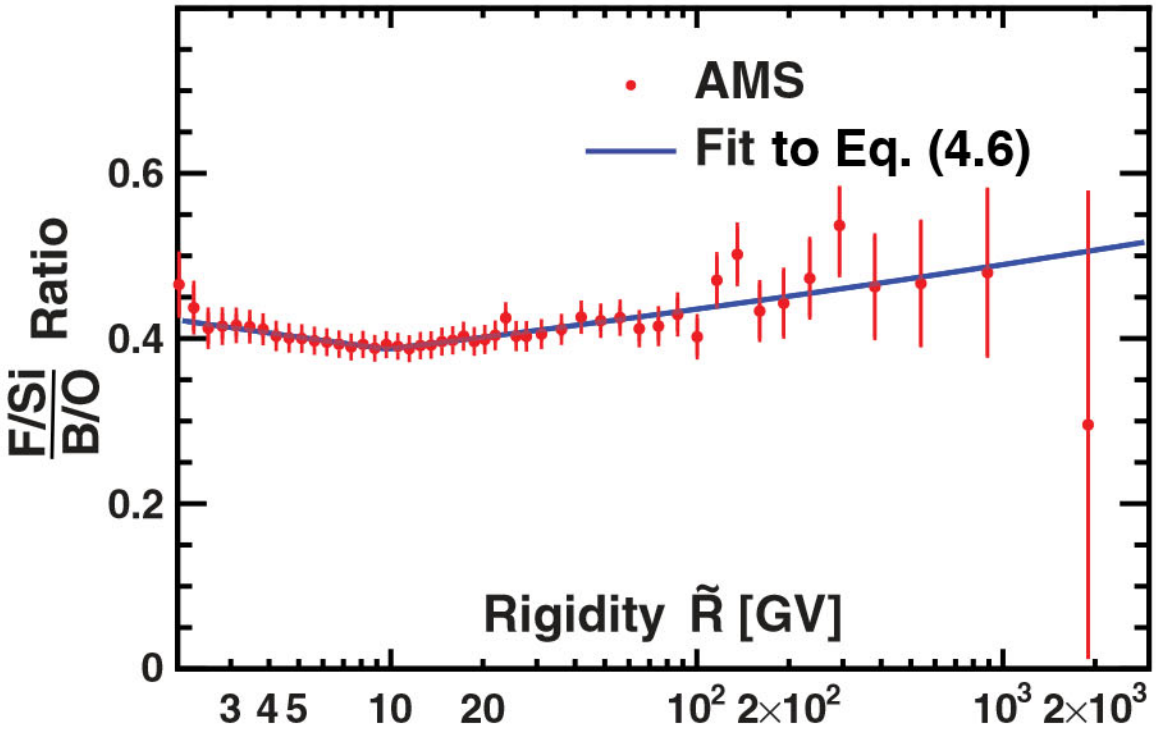

Figure 4-7: The AMS [(F/Si)/(B/O)] ratio as a function of rigidity with total errors. The solid blue curve shows the fit results of Eq. (4.6).

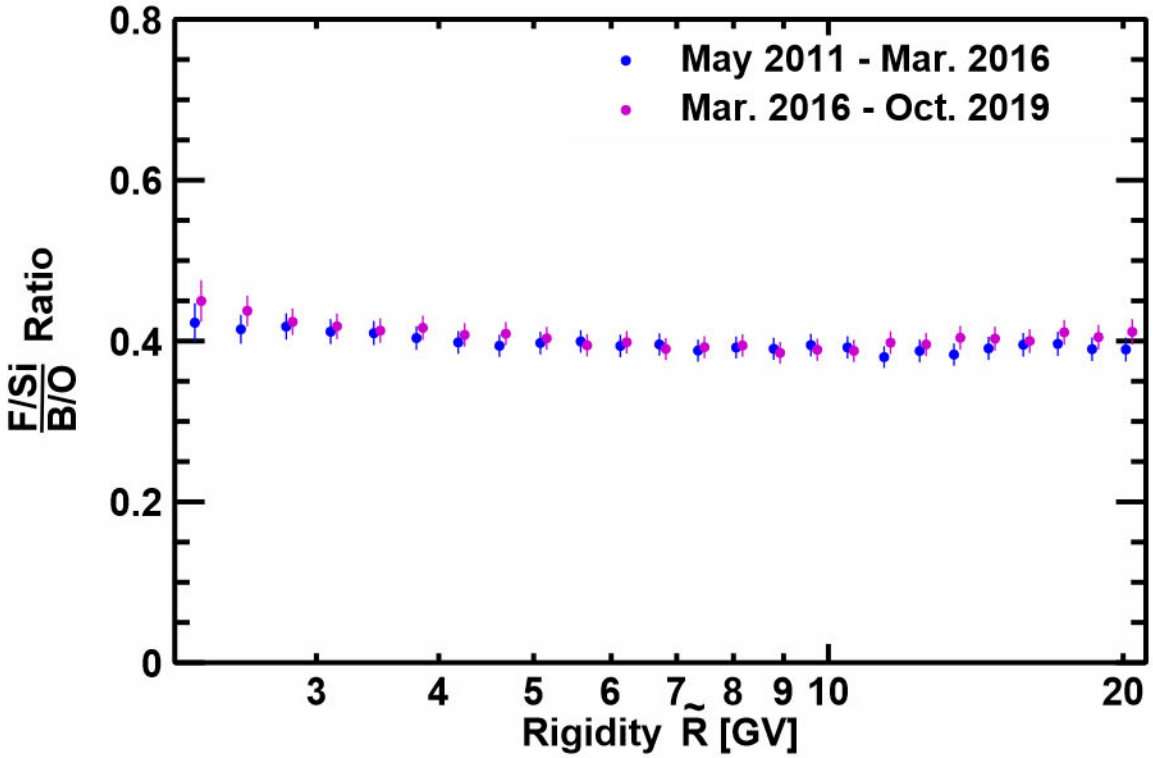

Figure 4-8: The AMS [(F/Si)/(B/O)] ratio below 20 GV for two different time periods, May 19, 2011 to March B/O 3, 2016 (blue dots) and March 3, 2016 to October 30, 2019 (magenta dots). For clarity, the data points are displaced horizontally.

4.2 The Sodium and Aluminum Fluxes

In the previous chapter, the measurements of events collected by AMS (N_i), the exposure time (T), the trigger efficiency (ε_i) and the effective acceptance (A_i), together with their relative uncertainties, have been evaluated for sodium Na and aluminum Al. The fluxes are measured in 49 bins from 2.15 GV to 3.0 TV. By means of Eq. (3.1), they have been used to calculate the fluxes of sodium and aluminum.

Figure 4-9 a) shows the Na flux as a function of rigidity $\tilde{R}$ with the total errors, the sum in quadrature of statistical and systematic errors, together with the AMS nitrogen N flux [60]. Figure 4-9 b) shows the Al flux as a function of rigidity $\tilde{R}$ with the total errors, the sum in quadrature of statistical and systematic errors, together with the AMS N flux [60].

To examine the rigidity dependence of the Na and Al fluxes, the variation of the flux spectral index γ with rigidity was obtained in a model-independent way from Eq. (4.1) over non-overlapping rigidity intervals bounded by 7.09, 12.0, 16.6, 28.8, 45.1, 80.5, 211.0, and 3000.0 GV. The results are presented in Figure 4-10 a) and b) in comparison with the N spectral index [60]. As seen from Figure 4-9 and Figure 4-10, below $\sim$ 100 GV, the Na flux and spectral index follow the N flux and spectral index and, above $\sim$ 100 GV, the Al flux and spectral index follow the N flux and spectral index.

Figure 4-11 shows the AMS Na and Al fluxes as a function of kinetic energy per nucleon E_k together with earlier measurements [42, 50, 54–57]. The Na and Al fluxes are expressed as a function of kinetic energy per nucleon E_k using Eq. (4.3). The rigidity is converted to E_k assuming that the sample is entirely ^{23}Na and ^{27}Al respectively. Also shown in the figure are the predictions of the latest GALPROP-HELMOD cosmic ray propagation model [23], which are based on published AMS data on the two primary cosmic ray classes, He-C-O and Ne-Mg-Si and other AMS data. The GALPROP-HELMOD model prediction of the Al flux agrees well with the AMS Al data above 3 GeV/n.

To obtain the primary $\Phi^{\rm P}_{\rm Na}$ and secondary $\Phi^{\rm S}_{\rm Na}$ components in the Na flux

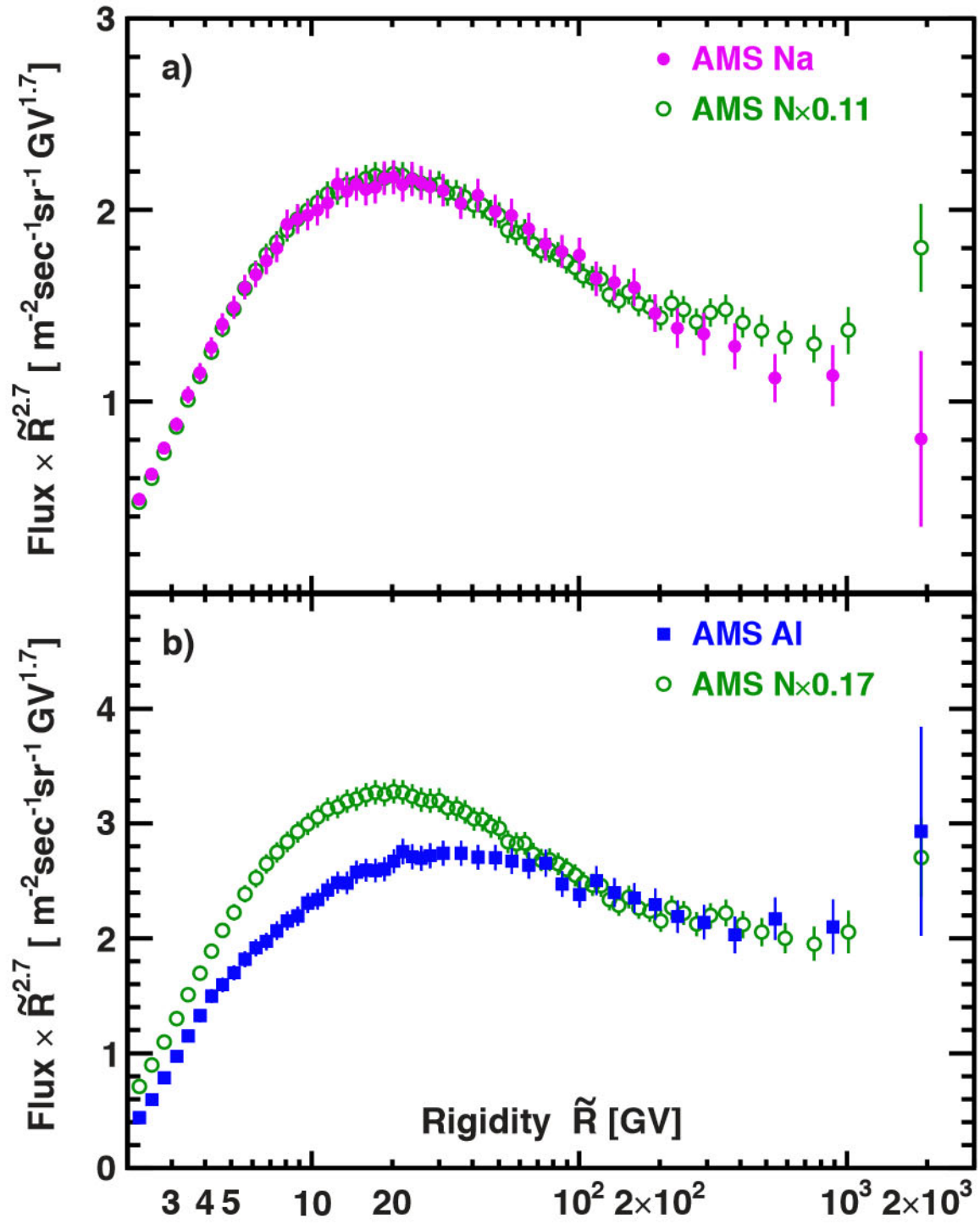

Figure 4-9: The AMS a) Na (magenta points) and b) Al (blue points) fluxes together with the rescaled AMS N (green points) flux [60] multiplied by $\tilde{R}^{2.7}$ with total errors as functions of rigidity.

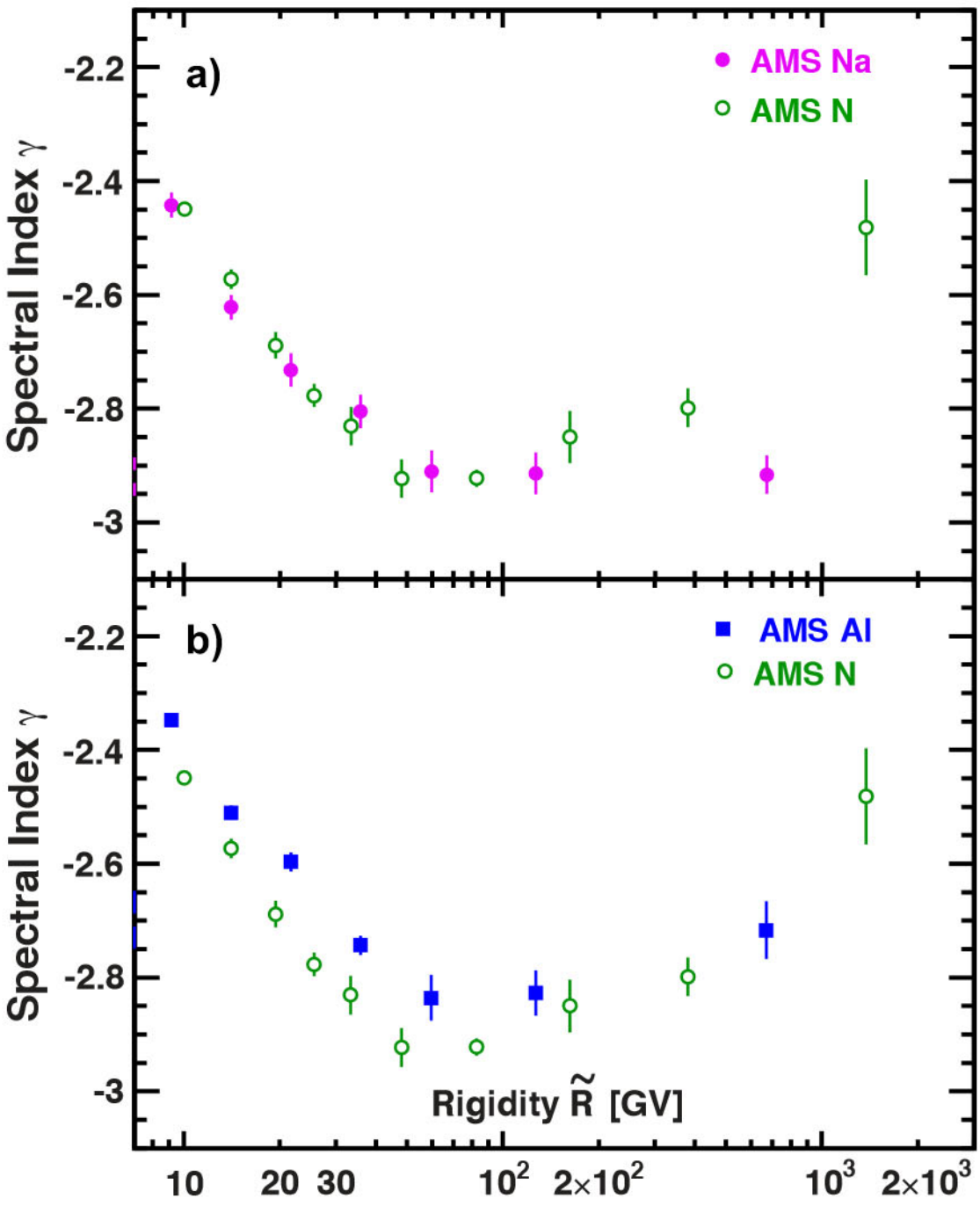

Figure 4-10: The AMS a) Na (magenta points) and b) Al (blue points) flux spectral indices together with N (green points) flux spectral index [60] as functions of rigidity.

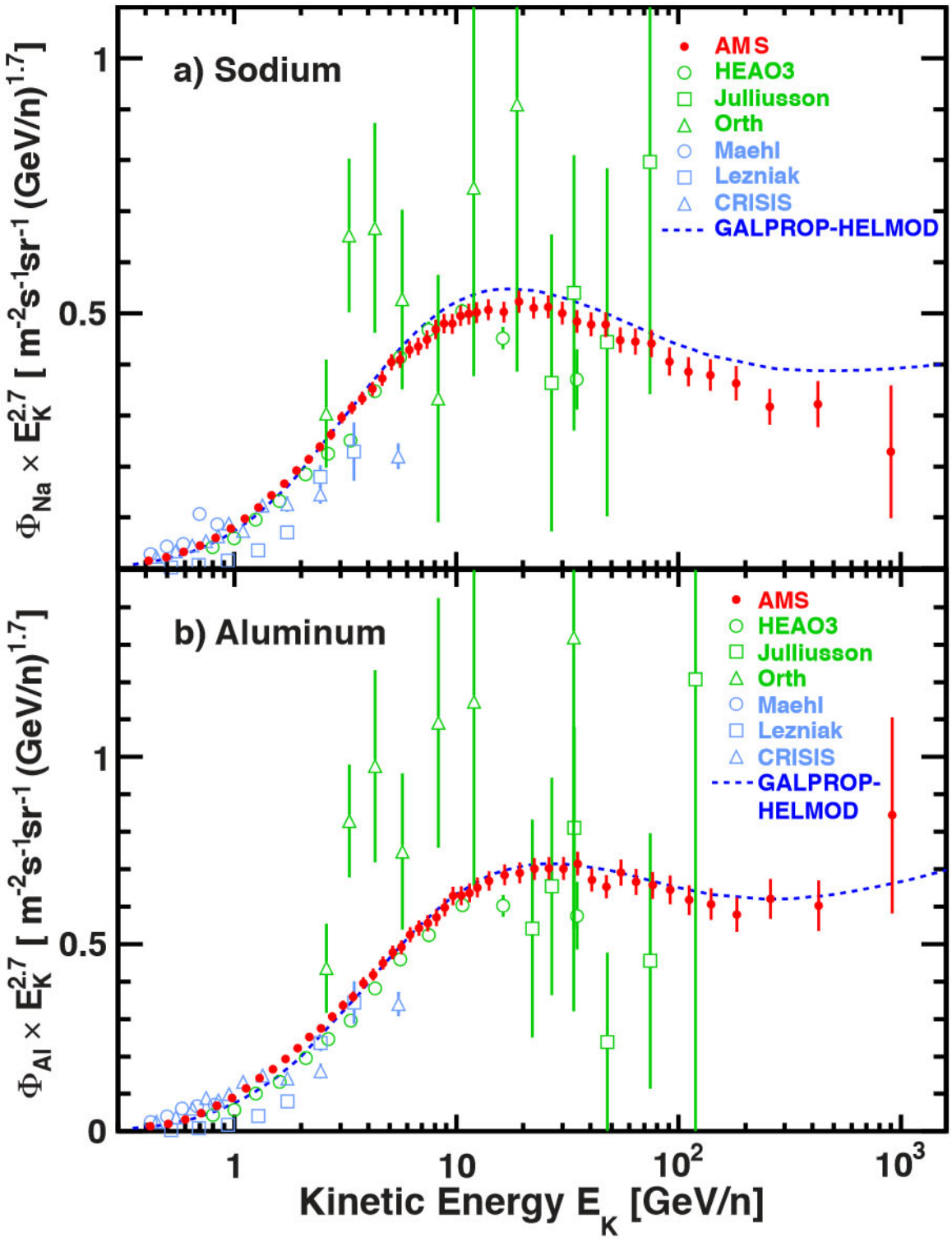

Figure 4-11: The AMS a) Na flux and b) Al flux as functions of kinetic energy per nucleon E_K multiplied by $E_K^{2.7}$ together with earlier measurements [42,50,54–57]. The dashed blue lines show predictions of the latest GALPROP-HELMOD model [23].

$\Phi_{Na} = \Phi^{P}_{Na} + \Phi^{S}_{Na}$, a fit of Φ_{Na} to the weighted sum of a heavy primary cosmic ray flux, namely silicon Φ_{Si} [63], and of a heavy secondary cosmic ray flux, namely fluorine Φ_{F}, was performed above 6 GV. The fit yields $\Phi^{P}_{Na} = (0.036 \pm 0.003) \times \Phi_{Si}$ and $\Phi^{S}_{Na} = (1.36 \pm 0.04) \times \Phi_{F}$ with a χ^2/d.o.f. = 19/36. The fit results are shown in Figure 4-12 a).

Similarly, to obtain the primary Φ^{P}_{Al} and secondary Φ^{S}_{Al} components in the Al flux $\Phi_{Al} = \Phi^{P}_{Al} + \Phi^{S}_{Al}$, a fit of Φ_{Al} to the weighted sum of the silicon flux and the fluorine flux was performed above 6 GV. The fit yields $\Phi^{P}_{Al} = (0.103 \pm 0.004) \times \Phi_{Si}$ and $\Phi^{S}_{Al} = (1.04 \pm 0.03) \times \Phi_{F}$ with χ^2/d.o.f=24/36. The fit results are shown in Figure 4-12 b).

As seen from Figure 4-12, the contributions of the secondary components in both the sodium flux and the aluminum flux decrease with rigidity, and the contributions of the primary components increase with rigidity. The same dependence was also observed for the N flux [60], see also Figure 4-13. Table 4.1 details the primary Φ^{P}_{N}, Φ^{P}_{Na}, and Φ^{P}_{Al} and secondary Φ^{S}_{N}, Φ^{S}_{Na}, and Φ^{S}_{Al} components and also the primary fractions Φ^{P}_{N}/Φ_{N}, Φ^{P}_{Na}/Φ_{Na}, and Φ^{P}_{Al}/Φ_{Al} at different rigidities.

Flux	Primary	Secondary	Primary Fraction,%		
			6 GV	100 GV	2 TV
Φ_{N}	$(0.092 \pm 0.002) \times \Phi_{O}$	$(0.61 \pm 0.02) \times \Phi_{B}$	31±1	56±1	77±3
Φ_{Na}	$(0.036 \pm 0.003) \times \Phi_{Si}$	$(1.36 \pm 0.04) \times \Phi_{F}$	17±2	35±2	62±12
Φ_{Al}	$(0.103 \pm 0.004) \times \Phi_{Si}$	$(1.04 \pm 0.03) \times \Phi_{F}$	43±1	67±1	78±8

Table 4.1: The N [60], Na, and Al cosmic ray nuclei primary Φ^{P}_{N}, Φ^{P}_{Na}, and Φ^{P}_{Al} and secondary Φ^{S}_{N}, Φ^{S}_{Na}, and Φ^{S}_{Al} flux components, and their corresponding primary fractions Φ^{P}_{N}/Φ_{N}, Φ^{P}_{Na}/Φ_{Na}, and Φ^{P}_{Al}/Φ_{Al} at 6 GV, 100 GV, and 2 TV.

The observation that, similar to N [60, 105], both the Na and Al fluxes can be fit over a wide rigidity range as the linear combinations of primary and secondary fluxes is a new and important result, which permits the direct determination of the Na/Si and Al/Si abundance at the source, 0.036 ± 0.003 for Na/Si, and 0.103 ± 0.004 for Al/Si, without the need to consider the Galactic propagation of cosmic rays.

To study the effect of cosmic ray propagation on the Na/Si and Al/Si abundance ratio measurements at the source, the "slab" model (Section 1.1.4.1) studied in Ref.

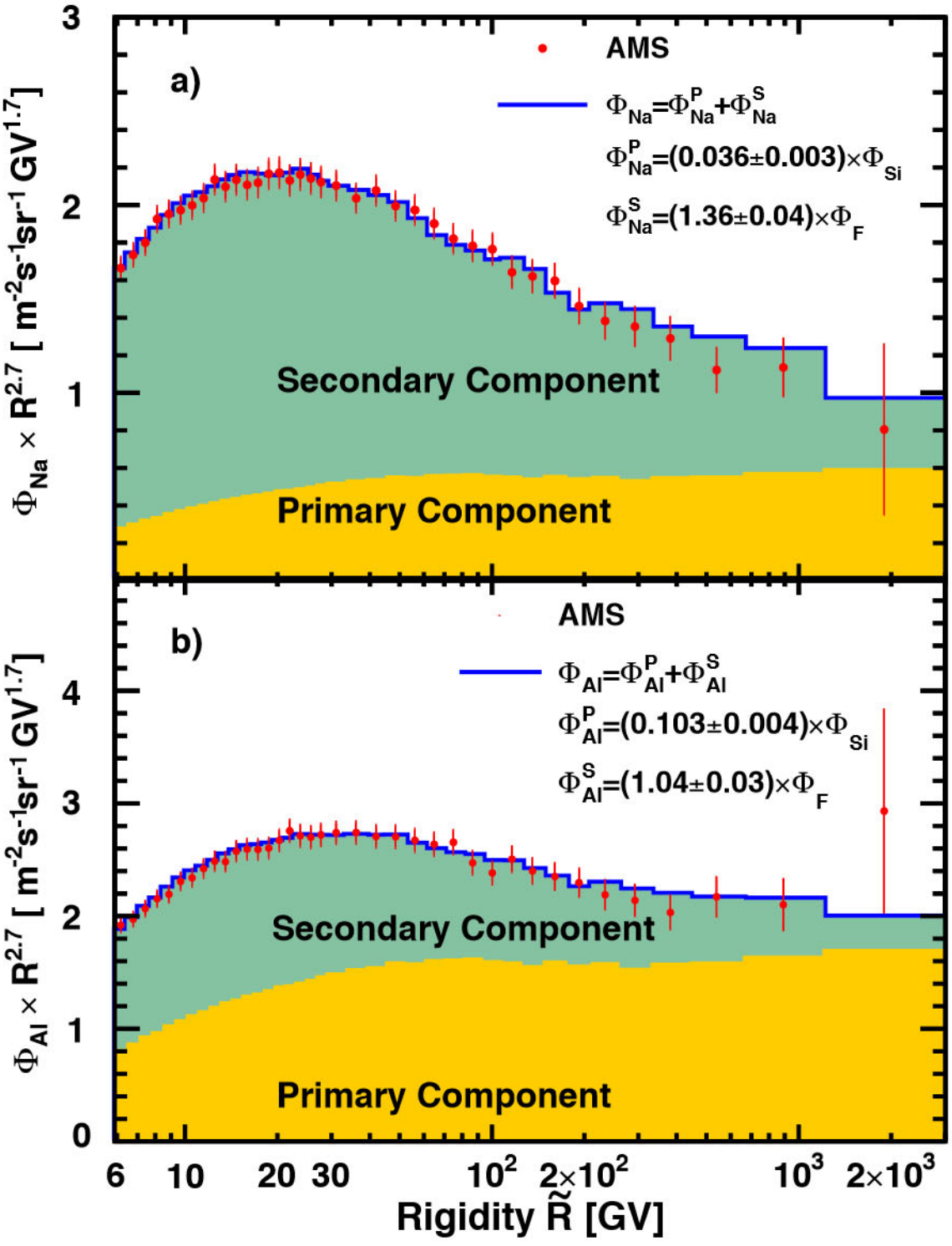

Figure 4-12: a) The AMS Na flux Φ_{Na} fit to the weighted sum of the Si flux Φ_{Si} and the F flux Φ_F above 6 GV. b) The AMS Al flux Φ_{Al} fit to the weighted sum of the Si flux Φ_{Si} and the F flux Φ_F above 6 GV, i.e. $\Phi_{Al} = \Phi^P_{Al} + \Phi^S_{Al}$. In both a) and b), the contributions of the primary and secondary components are indicated by the shading (yellow and green, respectively).

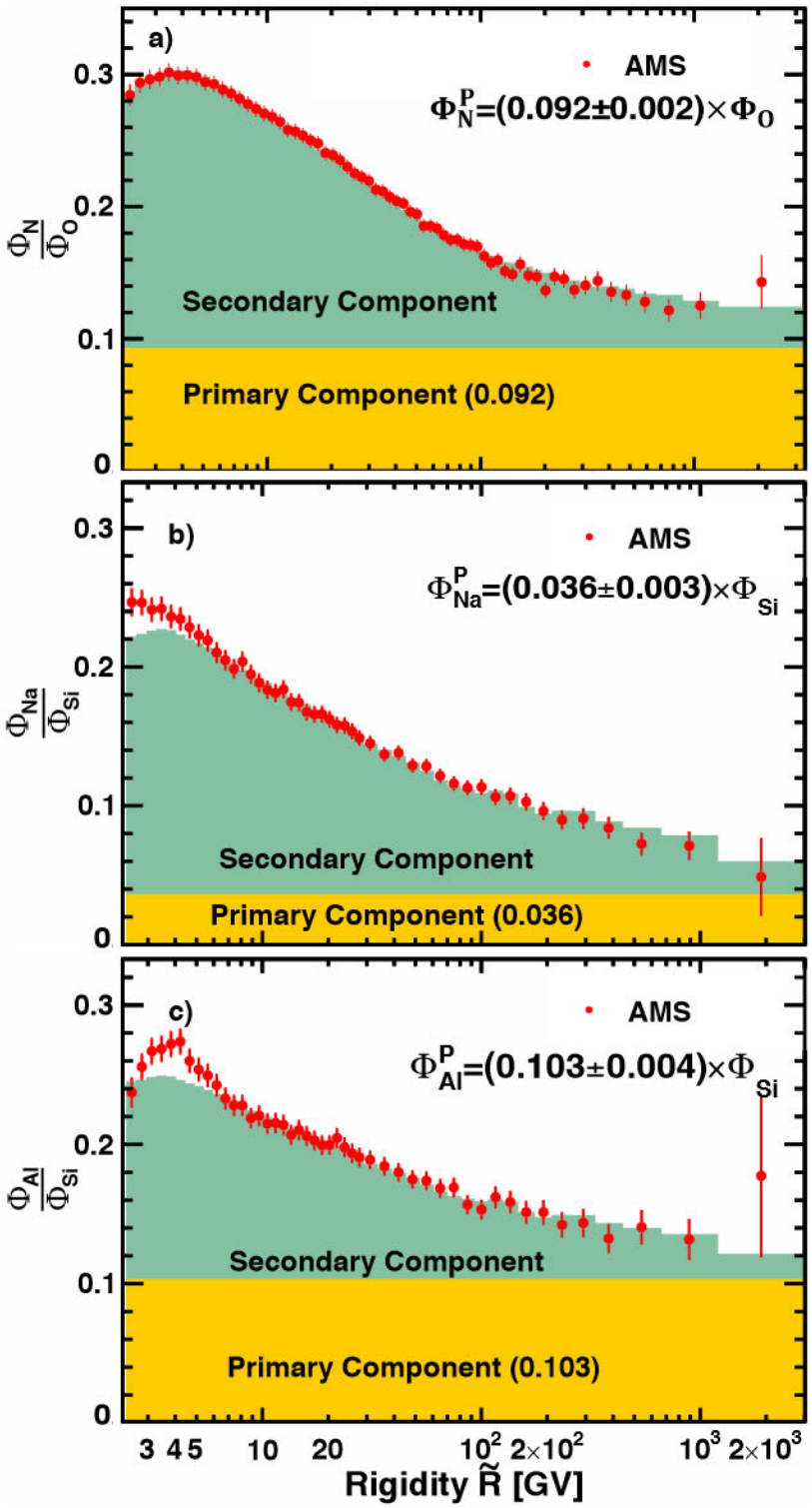

Figure 4-13: a) Φ_N/Φ_O and b) Φ_{Na}/Φ_{Si} and c) Φ_{Al}/Φ_{Si} as functions of rigidity. The contributions of the primary and secondary components are indicated by the shading (yellow and green, respectively). As seen, the contribution of the secondary component in all three fluxes decreases, and the contribution of the primary component correspondingly increases with rigidity. Note that for nitrogen, the fit starts from 2.15 GV and for Na and Al from 6 GV.

[98] is used as an example.

A fit of the $\Phi_{\rm Na} = \Phi^{\rm P}_{\rm Na} + \Phi^{\rm S}_{\rm Na}$, with $\Phi^{\rm P}_{\rm Na} = k \left(\frac{R}{192\ {\rm GV}}\right)^{\Delta} e^{-\lambda_S(\tilde{\sigma}_{\rm Na}-\tilde{\sigma}_{\rm Si})} \times \Phi_{\rm Si}$, where $e^{-\lambda_S(\tilde{\sigma}_{\rm Na}-\tilde{\sigma}_{\rm Si})}$ describes the propagation of primary nuclei through the interstellar medium [14] together with a source term $k \left(\frac{R}{192\ {\rm GV}}\right)^{\Delta}$; and $\Phi^{\rm S}_{\rm Na} = \kappa_{\rm Na} \times \Phi_{\rm F}$ was performed above 6 GV. By assuming the same rigidity dependence of Na and Si fluxes at the source, the parameter Δ was set to zero and the primary component becomes $\Phi^{\rm P}_{\rm Na} = k_{\rm Na} \cdot e^{-\lambda_S(\tilde{\sigma}_{\rm Na}-\tilde{\sigma}_{\rm Si})} \times \Phi_{\rm Si}$, where $k_{\rm Na}$ is the Na/Si abundance ratio at the source,

$$\lambda_S = \begin{cases} \lambda\,(R/192\ {\rm GV})^{-0.38\pm0.02} & R \leq 192\ {\rm GV} \\ \lambda\,(R/192\ {\rm GV})^{-0.24\pm0.03} & R > 192\ {\rm GV} \end{cases} \tag{4.7}$$

is a mean material grammage (g cm^{-2}) with rigidity dependence from Refs. [60,61,106] and λ is the grammage at $R = 192$ GV,

$$\tilde{\sigma}_A = \frac{1-f}{m_p}\,\sigma^{A+p} + \frac{f}{m_{He}}\,\sigma^{A+He} \tag{4.8}$$

is the mass averaged cross section of a nucleus A, $f = 0.28 \pm 0.02$ is the helium mass fraction in the interstellar medium [14], m_p and m_{He} are the proton and ^{4}He masses, and σ^{A+p} and σ^{A+He} are the corresponding nuclei inelastic cross sections with protons and helium in the interstellar medium, respectively, evaluated using measurements from Refs. [107, 108] and Eq. (3.9). From Table SA of Ref. [98], the λ parameter values are consistent with 1 g/cm^2 between all AMS primary-to-primary flux ratios, so the λ parameter value was fixed to 1 g/cm^2. The fit parameters are $k_{\rm Na}$ and $\kappa_{\rm Na}$. The fit yields $k_{\rm Na} = 0.037 \pm 0.003$ and $\kappa_{\rm Na} = 1.32 \pm 0.04$ with a χ^2/d.o.f. $= 18/36$. Similarly, a fit of the $\Phi_{\rm Al} = \Phi^{\rm P}_{\rm Al} + \Phi^{\rm S}_{\rm Al}$, with $\Phi^{\rm P}_{\rm Al} = k_{\rm Al} \cdot e^{-\lambda_S(\tilde{\sigma}_{\rm Al}-\tilde{\sigma}_{\rm Si})} \times \Phi_{\rm Si}$ and $\Phi^{\rm S}_{\rm Al} = \kappa_{\rm Al} \times \Phi_{\rm F}$ was performed above 6 GV assuming the same rigidity dependence of Al and Si fluxes at the source. The fit yields $k_{\rm Al} = 0.104 \pm 0.004$ and $\kappa_{\rm Al} = 1.00 \pm 0.04$ with a χ^2/d.o.f. $= 24/36$. The fit results are shown in Figure 4-14.

Similar fits were done with the "leaky-box" model (Section 1.1.4.2) studied in Ref. [98]. A fit of the $\Phi_{\rm Na} = \Phi^{\rm P}_{\rm Na} + \Phi^{\rm S}_{\rm Na}$, with $\Phi^{\rm P}_{\rm Na} = k \left(\frac{R}{192\ {\rm GV}}\right)^{\Delta} \frac{1+\lambda_S\,\tilde{\sigma}_{Si}}{1+\lambda_S\,\tilde{\sigma}_{Na}} \times \Phi_{\rm Si}$, where $\frac{1+\lambda_S\,\tilde{\sigma}_{Si}}{1+\lambda_S\,\tilde{\sigma}_{Na}}$ describes the propagation of primary nuclei through the interstellar

medium [14] together with a source term $k\left(\frac{R}{192\ \mathrm{GV}}\right)^{\Delta}$; and $\Phi^{\mathrm{S}}_{\mathrm{Na}} = \kappa_{\mathrm{Na}} \times \Phi_{\mathrm{F}}$ was performed above 6 GV. By assuming the same rigidity dependence of Na and Si fluxes at the source, the parameter Δ was set to zero and the primary component becomes $\Phi^{\mathrm{P}}_{\mathrm{Na}} = k_{\mathrm{Na}} \cdot \frac{1+\lambda_S\tilde{\sigma}_{\mathrm{Si}}}{1+\lambda_S\tilde{\sigma}_{\mathrm{Na}}} \times \Phi_{\mathrm{Si}}$, where k_{Na} is the Na/Si abundance ratio at the source, and the other parameters are identical to that used in the "slab" model. The fit yields $k_{\mathrm{Na}} = 0.036 \pm 0.003$ and $\kappa_{\mathrm{Na}} = 1.34 \pm 0.04$ with a χ^2/d.o.f. $= 19/36$. Similarly, a fit of the $\Phi_{\mathrm{Al}} = \Phi^{\mathrm{P}}_{\mathrm{Al}} + \Phi^{\mathrm{S}}_{\mathrm{Al}}$, with $\Phi^{\mathrm{P}}_{\mathrm{Al}} = k_{\mathrm{Al}} \cdot \frac{1+\lambda_S\tilde{\sigma}_{\mathrm{Si}}}{1+\lambda_S\tilde{\sigma}_{\mathrm{Al}}} \times \Phi_{\mathrm{Si}}$ and $\Phi^{\mathrm{S}}_{\mathrm{Al}} = \kappa_{\mathrm{Al}} \times \Phi_{\mathrm{F}}$ was performed above 6 GV assuming the same rigidity dependence of Al and Si fluxes at the source. The fit yields $k_{\mathrm{Al}} = 0.103 \pm 0.004$ and $\kappa_{\mathrm{Al}} = 1.02 \pm 0.04$ with a χ^2/d.o.f. $= 24/36$.

This shows that the propagation effects on the Na/Si and Al/Si abundance ratio measurements at the source are negligible. The σ^{Na}, σ^{Al}, and σ^{Si} are similar as seen in Refs. [107, 108] and Figure 3-13. The similarity of $\tilde{\sigma}_{\mathrm{Na}}$, $\tilde{\sigma}_{\mathrm{Al}}$, and $\tilde{\sigma}_{\mathrm{Si}}$ ensures other propagation models are expected to yield the same results.

Finally, in Figure 4-15, cosmic nuclei fluxes measured by AMS as a function of rigidity from $Z = 2$ to $Z = 14$ are presented. It shows that there are two classes of primary cosmic rays, He-C-O and Ne-Mg-Si, and two classes of secondary cosmic rays, Li-Be-B and F. N, Na, and Al belong to a distinct group and are the combinations of primary and secondary cosmic rays.

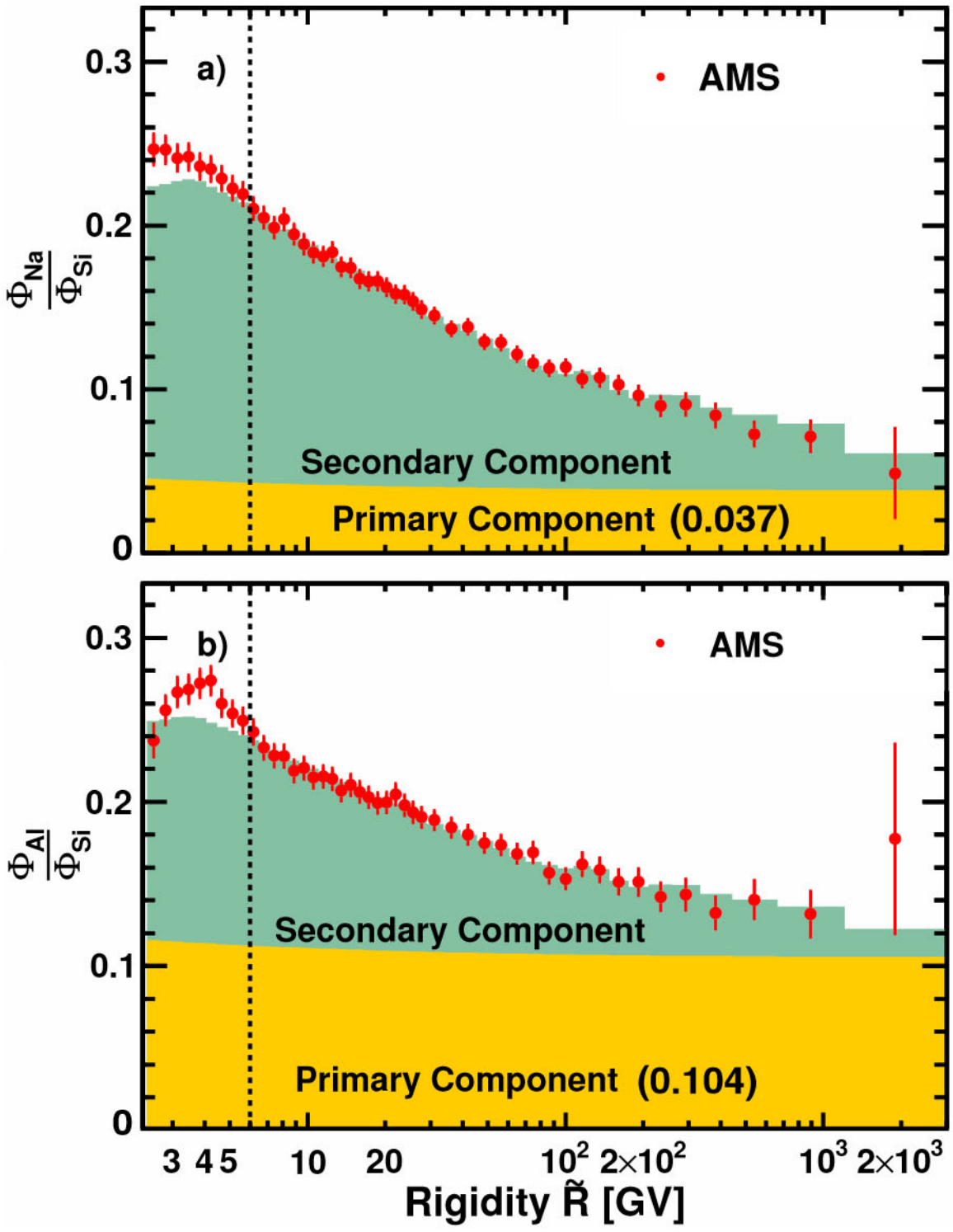

Figure 4-14: a) Φ_{Na}/Φ_{Si} and b) Φ_{Al}/Φ_{Si} as functions of rigidity. The contributions of the primary and secondary components obtained by fits with the slab model are indicated by the shading (yellow and green, respectively). The dashed vertical lines at 6 GV show the lower boundary of the fit range.

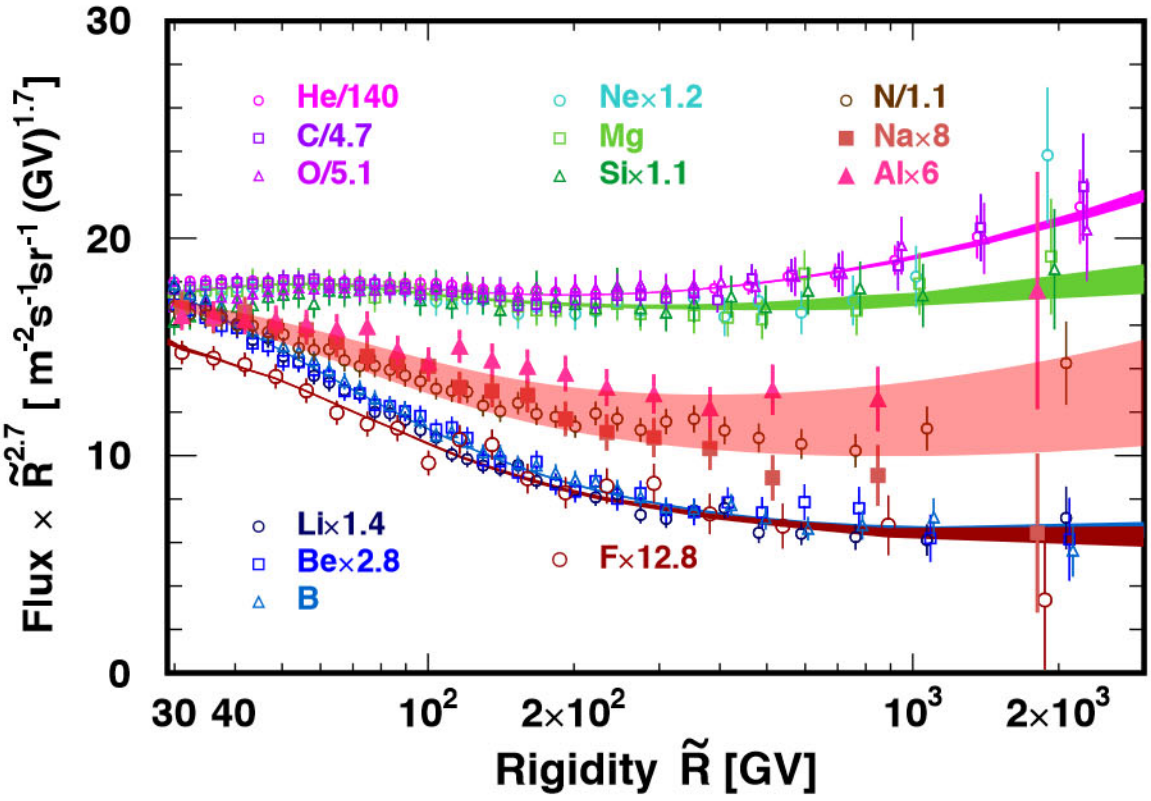

Figure 4-15: The fluxes of cosmic nuclei measured by AMS as a function of rigidity from $Z = 2$ to $Z = 14$ above 30 GV [60,61,63,109]. For clarity, data points above 400 GV are displaced horizontally. Fluxes are rescaled as indicated for display purposes. The shaded bands are to guide the eye.

Chapter 5

Conclusion

The detailed analysis of cosmic ray fluorine, sodium, and aluminum fluxes measured by the AMS experiment during its first 8.5 years of operation has been presented.

The precise measurement of fluorine flux as a function of rigidity from 2.15 GV to 2.9 TV has been performed based on 0.29 million fluorine events. The fluorine spectrum deviates from a single power law above 200 GV. Cosmic ray propagation parameter properties, such as diffusion coefficient rigidity dependence, are derived from the secondary-to-primary flux ratios. The heavier secondary-to-primary F/Si flux ratio rigidity dependence is found to be distinctly different from the lighter B/O (or B/C) rigidity dependence. In particular, above 10 GV, the [(F/Si)/(B/O)] ratio can be described by a power law R^{δ} with $\delta = 0.052 \pm 0.007$, revealing that the propagation properties of heavy cosmic rays, from F to Si, are different from those of light cosmic rays, from He to O. These are new and unexpected properties of cosmic rays. Traditionally, the parameters derived from the light secondary-to-primary flux ratio B/O (or B/C) are used to describe all cosmic ray species including the heaviest ones [19, 20, 59]. The measurement on the heavy secondary-to-primary F/Si flux ratio reveals that the propagation properties of the heavy cosmic rays are different from the lighter ones.

Previously, AMS measurements of He, C, and O fluxes show that above 60 GV, these three spectra have identical rigidity dependence [60, 109]. AMS measured Ne, Mg, and Si spectra have identical rigidity dependence above 86.5 GV [60, 109]. Above

86.5 GV, the rigidity dependence of primary cosmic rays Ne, Mg, and Si spectra is different from the rigidity dependence of primary cosmic rays He, C, and O [60, 109]. This shows that the Ne, Mg, and Si and He, C, and O are two different classes of primary cosmic rays. AMS measurements of Li, Be, and B show that above 30 GV, these three spectra have identical rigidity dependence [60, 61]. The measurement of fluorine flux shows that the rigidity dependence of secondary cosmic rays F flux is different from the rigidity dependence of secondary cosmic rays Li, Be, and B spectra. This shows that the secondary cosmic rays also have two classes but that the rigidity dependence of the two secondary classes is distinctly different from the rigidity dependence of the two primary classes.

The sodium and aluminum fluxes have been measured as functions of rigidity from 2.15 GV to 3.0 TV based on 0.46 million sodium and 0.51 million aluminum events. The measurements of sodium and aluminum fluxes show that sodium and aluminum, together with nitrogen, belong to a distinct cosmic ray group and are the combinations of primary and secondary cosmic rays.

Similar to the nitrogen flux, which is well described by the sum of a primary cosmic ray component (proportional to the oxygen flux) and a secondary cosmic ray component (proportional to the boron flux), both the sodium and aluminum fluxes are well described by the sums of a primary cosmic ray component (proportional to the silicon flux) and a secondary cosmic ray component (proportional to the fluorine flux). The fraction of the primary component increases with rigidity for the nitrogen, sodium, and aluminum fluxes and becomes dominant at the highest rigidities. The observation that the sodium and aluminum fluxes can be fit over a wide rigidity range as the linear combinations of primary silicon and secondary fluorine fluxes is a new and important result, which permits the direct determination of the Na/Si and Al/Si abundance ratios at the source, 0.036 ± 0.003 for Na/Si and 0.103 ± 0.004 for Al/Si, without the need to consider the Galactic propagation of cosmic rays.

As compared with previous measurements, the measurements presented in this thesis greatly improve the state of knowledge of fluorine, sodium, and aluminum spectra up to the TV rigidity region with unprecedented accuracy, providing unique

input to the understanding of cosmic ray production and propagation.

AMS will continue collecting data through the lifetime of the ISS. There are many more physics topics to be explored to improve the understanding of cosmic ray origin, acceleration, and propagation. Some of the physics topics are discussed briefly in the following paragraph.

As the study of the fluorine flux shows that the propagation properties of heavy cosmic rays, from F to Si, are different from those of light cosmic rays, from He to O. To understand the cosmic ray propagation comprehensively, it is essential to measure the heavier secondary-to-primary ratios, such as Sc/Fe, Ti/Fe, and V/Fe. By simultaneously studying all nuclei fluxes as a function of rigidity, AMS will provide unique inputs to the propagation models. Measurements of the isotopic composition in cosmic rays would also be great interest. Cosmic ray residence time is estimated to be of the order of Myr [14]. Some of the secondary cosmic ray isotopes created by the collisions of primary cosmic rays with the interstellar medium are radioactive. The so-called cosmic ray clocks, ^{10}Be, ^{26}Al, ^{36}Cl, and ^{54}Mn, have half-lives of the same order of magnitude as the cosmic ray residence time [14]. Therefore, measurements of ^{10}Be, ^{26}Al, ^{36}Cl, and ^{54}Mn will precisely establish the cosmic ray residence time. The nucleosynthesis mechanism changes from stellar fusion to neutron capture for elements with $Z > 28$. Abundances and spectra of ultra-heavy nuclei with $Z > 28$ provide information on their origin and physical processes responsible for their acceleration.

Over the years, many theoretical models of cosmic rays are developed using AMS results as input ([23, 59, 62, 65, 106], ..), but so far there is not one that completely describes all AMS data. New measurements from AMS will continuously provide valuable input to the understanding of cosmic ray origin, acceleration, and propagation.

Bibliography

[1] T. Gaisser, R. Engel, and E. Resconi, *Cosmic Rays and Particle Physics*. Cambridge University Press, 2016.

[2] V. F. Hess, "Über Beobachtungen der durchdringenden Strahlung bei sieben Freiballonfahrten," *Phys. Z*, vol. 13, pp. 1084–1091, 1912.

[3] C. D. Anderson, "The positive electron," *Phys. Rev.*, vol. 43, p. 491, 1933.

[4] S. H. Neddermeyer and C. D. Anderson, "Note on the Nature of Cosmic-Rays Particles," *Phys. Rev.*, vol. 51, pp. 884–886, 1937.

[5] C. Lattes *et al.*, "Processes Involving Charged Mesons," *Nature*, vol. 159, pp. 694–697, 1947.

[6] M. Tanabashi *et al.*, "Review of Particle Physics," *Phys. Rev. D*, vol. 98, 2018.

[7] J. R. Hoerandel, "Cosmic-ray composition and its relation to shock acceleration by supernova remnants," *Advances in Space Research*, vol. 41, pp. 442–463, 2008.

[8] D. J. Bird *et al.*, "The Cosmic-Ray Energy Spectrum Observed by the Fly's Eye," *Astrophys. J.*, vol. 424, p. 491, 1994.

[9] G. Zatsepin and V. Kuz'min, "Upper Limit of the Spectrum of Cosmic Rays," *Soviet Journal of Experimental and Theoretical Physics Letters*, vol. 4, 1966.

[10] T. Gaisser and T. Stanev, "High-energy cosmic rays," *Nuclear Physics A*, vol. 777, pp. 98–110, 2006.

[11] N. E. Yanasak *et al.*, "Measurement of the Secondary Radionuclides Be, Al, Cl, Mn, and C and Implications for the Galactic Cosmic-Ray Age," *Astrophys. J.*, vol. 563, p. 768, 2001.

[12] W. Li *et al.*, "Nearby supernova rates from the Lick Observatory Supernova Search – III. The rate–size relation, and the rates as a function of galaxy Hubble type and colour," *Monthly Notices of the Royal Astronomical Society*, vol. 412, pp. 1473–1507, 2011.

[13] E. Fermi, "On the Origin of the Cosmic Radiation," *Phys. Rev.*, vol. 75, 1949.

[14] M. Longair, *The acceleration of high energy particles.* Cambridge University Press, 2011.

[15] A. Strong, I. Moskalenko, and V. Ptuskin, "Cosmic-Ray Propagation and Interactions in the Galaxy," *Annual Review of Nuclear and Particle Science*, vol. 57, pp. 285–327, 2007.

[16] M. Kruskal *et al.*, "Secondary Production as the Origin of the Cosmic-ray Positron Excess," *Astrophys. J.*, vol. 818, p. 70, 2016.

[17] A. N. Kolmogorov, "The local structure of turbulence in incompressible viscous fluid for very large Reynolds numbers," *Proc. R. Soc.A*, vol. 434, p. 9, 1991.

[18] R. Kraichnan, "Inertial-Range Spectrum of Hydromagnetic Turbulence," *Phys. Fluids*, vol. 8, p. 1385, 1965.

[19] A. Strong and I. Moskalenko, "Propagation of cosmic-ray nucleons in the galaxy," *Astrophys. J.*, vol. 509, pp. 212–228, 1998.

[20] R. Trotta *et al.*, "Constraints on cosmic-ray propagation models from a global Bayesian analysis," *Astrophys. J.*, vol. 729, p. 106, 2011.

[21] C. Evoli *et al.*, "Cosmic-ray propagation with DRAGON2: I. numerical solver and astrophysical ingredients," *Journal of Cosmology and Astroparticle Physics*, no. 2, p. 15, 2017.

[22] A. Strong, I. Moskalenko, *et al.*, "GALPROP: Code for Cosmic-Ray Transport and Diffuse Emission Production," *Astrophysics Source Code Library*, 2010.

[23] M. J. Boschini *et al.*, "Inference of the Local Interstellar Spectra of Cosmic-Ray Nuclei Z less than 28 with the GalProp–HelMod Framework," *Astrophys. J. Suppl. Ser.*, vol. 250, p. 27, 2020.

[24] D. Heck and T. Pierog, "Extensive Air Shower Simulations with CORSIKA: A User's Guide," 2021.

[25] R. Ulrich, R. Engel, and M. Unger, "Hadronic multiparticle production at ultrahigh energies and extensive air showers," *Phys. Rev. D*, vol. 83, p. 054026, 2011.

[26] M. Amenomori *et al.*, "The All-Particle Spectrum of Primary Cosmic Rays in the Wide Energy Range from 10^{14} to 10^{17} eV Observed with the Tibet-III Air-Shower Array," *Astrophys. J.*, vol. 678, p. 1165, 2008.

[27] R. Alfaro *et al.*, "All-particle cosmic ray energy spectrum measured by the HAWC experiment from 10 to 500 TeV," *Phys. Rev. D*, vol. 96, p. 122001, 2017.

[28] F. Varsi, "Energy spectrum and composition measurements of cosmic rays from GRAPES-3 experiment," *ICRC 2019 proceedings*, 2019.

[29] M. Bertaina, "KASCADE-Grande energy spectrum of cosmic rays interpreted with post-LHC hadronic interaction models," *ICRC 2019 proceedings*, 2019.

[30] D. Kostunin, "Seven years of Tunka-Rex operation," *ICRC 2019 proceedings*, 2019.

[31] R. Koirala, "Low Energy Cosmic Ray Spectrum from 250 TeV to 10 PeV using IceTop," *ICRC 2019 proceedings*, 2019.

[32] A. P. Garyaka *et al.*, "An all-particle primary energy spectrum in the 3–200 PeV energy range," *Journal of Physics G: Nuclear and Particle Physics*, vol. 35, p. 115201, 2008.

[33] T. Abu-Zayyad *et al.*, "The Cosmic Ray Energy Spectrum Observed with the Surface Detector of the Telescope Array Experiment," *Astrophys. J. Lett.*, vol. 768, p. L1, 2013.

[34] A. Aab *et al.*, "Measurement of the cosmic-ray energy spectrum above 2.5 $\times 10^{18}$ eV using the Pierre Auger Observatory," *Phys. Rev. D*, vol. 102, p. 062005, 2020.

[35] V. Verzi, "Measurement of the energy spectrum of ultra-high energy cosmic rays using the Pierre Auger Observatory," *ICRC 2019 proceedings*, 2019.

[36] D. Ivanov, "Energy Spectrum Measured by the Telescope Array," *ICRC 2019 proceedings*, 2019.

[37] F. G. Schroder, "News from Cosmic Ray Air Showers," *ICRC 2019 proceedings*, 2019.

[38] Y. Takahashi, "Elemental abundance of high energy cosmic rays," *Nuclear Physics B (Proc. Suppl.)*, vol. 60, pp. 83–92, 1998.

[39] M. Hareyama *et al.*, "Final Results of RUNJOB and Related Topics," *J. Phys.: Conf. Ser.*, vol. 47, p. 13, 2006.

[40] J. Chang *et al.*, "An excess of cosmic ray electrons at energies of 300-800 GeV," *Nature*, vol. 456, pp. 362–365, 2008.

[41] H. S. Ahn *et al.*, "Energy Spectra of Cosmic-ray Nuclei at High Energies," *Astrophys. J.*, vol. 707, p. 593, 2009.

[42] J. S. Young *et al.*, "The elemental and isotopic composition of cosmic rays - Silicon to nickel," *Astrophys. J.*, vol. 246, pp. 1014–1030, 1981.

[43] J. T. Link *et al.*, "Measurements of the Ultra-Heavy Galactic Cosmic-Ray Abundances between Z=30 and Z=40 with the TIGER Instrument," *ICRC 2003 proceedings*, 2003.

[44] P. J. Boyle *et al.*, "Cosmic ray composition at high energies: The TRACER project," *Advances in Space Research*, p. 409, 2008.

[45] A. Yamamoto *et al.*, "The BESS Program," *Nuclear Physics B - Proceedings Supplements*, vol. 166, p. 62, 2007.

[46] M. BOEZIO *et al.*, "The Cosmic-Ray Proton and Helium Spectra between 0.4 and 200 GV," *Astrophys. J.*, vol. 518, pp. 457–472, 1999.

[47] M. Garcia-Munoz *et al.*, "The cosmic-ray age deduced from the Be-10 abundance," *Astrophys. J.*, vol. 201, p. 141, 1975.

[48] E. C. Stoner *et al.*, "Cosmic Ray Investigation for the Voyager Missions; Energetic Particle Studies in the Outer Atmosphere - and Beyond," *Space Science Reviews*, vol. 21, p. 355, 1977.

[49] E. C. Stone *et al.*, "The Cosmic Ray Isotope Spectrometer for the Ad- vanced Composition Explorer.," *Space Science Reviews*, vol. 86, pp. 1–4, 1998.

[50] J. Engelmann *et al.*, "Charge composition and energy spectra of cosmic-ray nuclei for elements from Be to Ni - Results from HEAO-3-C2," *Astronomy and Astrophysics*, vol. 233, pp. 96–111, 1990.

[51] D. Muller *et al.*, "Energy Spectra and Composition of Primary Cosmic Rays," *Astrophys. J.*, vol. 374, pp. 356–367, 1991.

[52] M. A. Duvernois and M. R. Thayer, "The Elemental Composition of the Galactic Cosmic-Ray Source: ULYSSES High-Energy Telescope Results," *Astrophys. J.*, vol. 465, p. 982, 1996.

[53] W. Menn *et al.*, "The PAMELA space experiment," *Advances in Space Research*, vol. 51, p. 209, 2013.

[54] E. Juliusson, "Charge Composition and Energy Spectra of Cosmic-Ray Nuclei at Energies above 20 GeV Per Nucleon," *Astrophys. J.*, vol. 191, pp. 331–348, 1974.

[55] C. Orth *et al.*, "Abundances and spectra for cosmic-ray nuclei from lithium to iron for 2 to 150 GeV per nucleon," *Astrophys. J.*, vol. 226, pp. 1147–1161, 1978.

[56] R. C. Maehl, J. F. Ormes, A. J. Fisher, and F. A. Hagen, "Energy spectra of cosmic ray nuclei: 4 Z 26 and 0.3 E 2 GeV," *Astrophysics and Space Science*, vol. 47, pp. 163–184, 1977.

[57] J. A. Lezniak and W. R. Webber, "The charge composition and energy spectra of cosmic-ray nuclei from 3000 MeV per nucleon to 50 GeV per nucleon," *Astrophys. J.*, vol. 223, pp. 676–696, 1978.

[58] D. Maurin, F. Melot, and R. Taillet, "A database of charged cosmic rays," *Astronomy and Astrophysics*, vol. 569, 2014.

[59] C. Evoli, R. Aloisio, and P. Blasi, "Galactic cosmic rays after the AMS-02 observations," *Phys. Rev. D*, vol. 99, p. 103023, 2019.

[60] M. Aguilar *et al.*, "The Alpha Magnetic Spectrometer (AMS) on the international space station: Part II — Results from the first seven years," *Physics Reports*, vol. 894, pp. 1–116, 2021.

[61] M. Aguilar *et al.*, "Observation of New Properties of Secondary Cosmic Rays Lithium, Beryllium, and Boron by the Alpha Magnetic Spectrometer on the International Space Station," *Phys. Rev. Lett.*, vol. 120, p. 021101, 2018.

[62] M. J. Boschini *et al.*, "Deciphering the Local Interstellar Spectra of Secondary Nuclei with the Galprop/Helmod Framework and a Hint for Primary Lithium in Cosmic Rays," *Astrophys. J.*, vol. 889, p. 167, 2020.

[63] M. Aguilar *et al.*, "Properties of Neon, Magnesium, and Silicon Primary Cosmic Rays Results from the Alpha Magnetic Spectrometer," *Phys. Rev. Lett.*, vol. 124, p. 211102, 2020.

[64] B. Cartwright, "The Origin of Fluorine, Sodium, and Aluminum in the Galactic Cosmic Radiation," *Astrophys. J.*, vol. 169, pp. 299–310, 1971.

[65] P. Mertsch, A. Vittino, and S. Sarkar, "Explaining cosmic ray antimatter with secondaries from old supernova remnants," *arXiv e-prints*, 2020.

[66] K. Lübelsmeyer *et al.*, "Upgrade of the Alpha Magnetic Spectrometer (AMS-02) for long term operation on the International Space Station (ISS)," *Nucl. Instrum. Methods Phys. Res., Sect. A*, vol. 654, pp. 639–648, 2011.

[67] M. Aguilar *et al.*, "First Result from the Alpha Magnetic Spectrometer on the International Space Station: Precision Measurement of the Positron Fraction in Primary Cosmic Rays of 0.5-350 GeV," *Phys. Rev. Lett.*, vol. 110, p. 141102, 2013.

[68] K. Andeen, M. Heil, and F. Spada, "Operations and Alignment of the AMS-02 Transition Radiation Detector," *ICRC 2013 proceedings*, 2013.

[69] V. Bindi *et al.*, "Calibration and performance of the AMS-02 time of flight detector in space," *Nucl. Instrum. Methods Phys. Res., Sect. A*, vol. 743, pp. 22–29, 2014.

[70] L. Amati *et al.*, "The TOF counters of the AMS-02 experiment: space qualification tests and beam test results," *Nuclear Physics B (Proc. Suppl.)*, vol. 150, pp. 276–280, 2006.

[71] V. Bindi *et al.*, "The TOF-ACC flight electronics for the fast trigger and time of flight of the AMS-02 cosmic ray spectrometer," *Nucl. Instrum. Methods Phys. Res., Sect. A*, vol. 707, pp. 99–113, 2013.

[72] A. Oliva, "Performance, Operational Aspects and Impact on Physics Results of the AMS Tracker," *Vertex 2013 proceedings*, 2013.

[73] J. Alcaraz *et al.*, "The alpha magnetic spectrometer silicon tracker: Performance results with protons and helium nuclei," *Nucl. Instrum. Methods Phys. Res., Sect. A*, vol. 593, pp. 376–398, 2008.

[74] B. Alpat *et al.*, "The internal alignment and position resolution of the AMS-02 silicon tracker determined with cosmic-ray muons," *Nucl. Instrum. Methods Phys. Res., Sect. A*, vol. 613, pp. 207–217, 2010.

[75] G. Ambrosi *et al.*, "Alignment of the ams-02 silicon tracker," *ICRC 2013 proceedings*, 2013.

[76] Q. Yan *et al.*, "Determination of the rigidity scale of the Alpha Magnetic Spectrometer," *Nucl. Instrum. Methods Phys. Res., Sect. A*, vol. 849, pp. 10–14, 2017.

[77] Y. Jia *et al.*, "Nuclei charge measurement by the Alpha Magnetic Spectrometer silicon tracker," *Nucl. Instrum. Methods Phys. Res., Sect. A*, vol. 972, pp. 164–169, 2020.

[78] M. Graziani, *Time dependence of electron and positron fluxes measured with the AMS-02 spectrometer.* PhD thesis, Universita degli Studi di Perugia, 2015.

[79] T. Bruch and W. Wallra, "The Anti-Coincidence Counter shield of the AMS tracker," *Nucl. Instrum. Methods Phys. Res., Sect. A*, vol. 572, pp. 505–507, 2007.

[80] S. Rosier-Lees, "Performance of the AMS02 Electromagnetic Calorimeter in space," *Journal of Physics: Conference Series*, vol. 404, p. 012034, 2012.

[81] B. P. Roe *et al.*, "Boosted decision trees as an alternative to artificial neutral networks for particle identification," *Nucl. Instrum. Methods Phys. Res., Sect. A*, vol. 543, pp. 577–584, 2005.

[82] F. Cadoux *et al.*, "The Electromagnetic Calorimeter Trigger System for the AMS-02 Experiment," *IEEE Trans. Nucl. Sci.*, vol. 55, p. 817, 2008.

[83] J. Allison *et al.*, "Recent developments in Geant4," *Nucl. Instrum. Methods Phys. Res., Sect. A*, vol. 835, pp. 186–225, 2016.

[84] Q. Yan *et al.*, "Measurements of nuclear interaction cross sections on carbon target with the Alpha Magnetic Spectrometer on the International Space Station," *Nuclear Inst. and Methods in Physics Research A*, vol. 996, p. 121712, 2020.

[85] J. Alcaraz *et al.*, "Leptons in near earth orbit," *Physics Letters B*, vol. 484, pp. 10–22, 2000.

[86] E. Thébault *et al.*, "International Geomagnetic Reference Field: the 12th generation," *Earth, Planets and Space*, vol. 67, p. 79, 2015.

[87] Geomagnetic Field Modeling Working Group, "IGRF-13 Model," 2019.

[88] Y. Li, *Measurement of the Carbon and Oxygen Fluxes and their Ratio in Cosmic Rays with the AMS Experiment on the International Space Station.* PhD thesis, University of Geneva, 2017.

[89] V. M. Grichine, "A simple model for integral hadron-nucleus and nucleus-nucleus cross-sections," *Nucl. Instrum. Methods Phys. Res., Sect. B*, vol. 267, pp. 2460–2462, 2009.

[90] P. Kaitaniemi *et al.*, "INCL Intra-Nuclear Cascade and ABLA De-Excitation Models in Geant4," *Progress in NUCLEAR SCIENCE and TECHNOLOGY*, vol. 2, pp. 788–793, 2011.

[91] J. Ranft, "Dual parton model at cosmic ray energies," *Phys. Rev. D*, vol. 51, p. 64, 1995.

[92] S. Roesler *et al.*, "The Event Generator DPMJET-III at Cosmic Ray Energies," tech. rep., SLAC National Accelerator Lab., Menlo Park, CA (United States), Apr 2005.

[93] I. Tanihata *et al.*, "Measurements of interaction cross sections and radii of He isotopes," *Physics Letters B*, vol. 160, pp. 380–384, 1985.

[94] V. G. Ableev *et al.*, "Alpha-nuclear differential cross sections at 4.45 GeV/c/nucleon," *ACTA Physica Polonica B*, vol. 16, pp. 913–929, 1985.

[95] J. Jaros *et al.*, "Nucleus-nucleus total cross sections for light nuclei at 1.55 and 2.89 GeV/c per nucleon," *Phys. Rev. C*, vol. 18, p. 2273, 1978.

[96] A. Ozawa *et al.*, "Nuclear size and related topics ," *Nuclear Physics A*, vol. 693, pp. 32–62, 2001.

[97] I. Angelia and K. Marinova, "Table of experimental nuclear ground state charge radii: An update," *Atomic Data and Nuclear Data Tables*, vol. 99, pp. 69–95, 2013.

[98] M. Aguilar *et al.*, "Properties of Iron Primary Cosmic Rays: Results from the Alpha Magnetic Spectrometer," *Phys. Rev. Lett.*, vol. 126, p. 041104, 2021.

[99] G. Ambrosi *et al.*, "Nuclei Charge measurement with the AMS-02 Silicon Tracker," *ICRC 2015 proceedings*, 2015.

[100] M. Moll, "Charged Particle Tracking in High Energy Physics," *EIROforum School on Instrumentation*, 2011.

[101] J. Albert *et al.*, "Unfolding of differential energy spectra in the MAGIC experiment," *Nucl. Instrum. Methods Phys. Res., Sect. A*, vol. 583, p. 494, 2007.

[102] M. Aguilar *et al.*, "Precision Measurement of the Proton Flux in Primary Cosmic Rays from Rigidity 1 GV to 1.8 TV with the Alpha Magnetic Spectrometer on the International Space Station," *Phys. Rev. Lett.*, vol. 114, p. 171103, 2015.

[103] G. Lafferty and T. Wyatt, "Where to stick your data points: The treatment of measurements within wide bins," *Nucl. Instrum. Methods Phys. Res., Sect. A*, vol. 355, pp. 541–547, 1995.

[104] A. E. Vladimirov *et al.*, "GALPROP WebRun: An internet-based service for calculating galactic cosmic ray propagation and associated photon emissions," *Computer Physics Communications*, vol. 185, pp. 1156–1161, 2011.

[105] M. Aguilar *et al.*, "Precision measurement of cosmic-ray nitrogen and its primary and secondary components with the alpha magnetic spectrometer on the international space station," *Phys. Rev. Lett.*, vol. 121, p. 051103, 2018.

[106] G. Jóhannesson *et al.*, "Bayesian analysis of cosmic-ray propagation: evidence against homogeneous diffusion," *Astrophys. J.*, vol. 824, p. 16, 2016.

[107] W. R. Webber, J. C. Kish, and D. A. Schrier, "Total charge and mass changing cross sections of relativistic nuclei in hydrogen, helium, and carbon targets," *Phys. Rev. C*, vol. 41, p. 520, 1990.

[108] V. Glagolev *et al.*, "Cross sections of the interactions of He nuclei with protons," *Z. Phys. C - Particles and Fields*, vol. 60, pp. 421–425, 1993.

[109] M. Aguilar *et al.*, "Observation of the Identical Rigidity Dependence of He, C, and O Cosmic Rays at High Rigidities by the Alpha Magnetic Spectrometer on the International Space Station," *Phys. Rev. Lett.*, vol. 119, p. 251101, 2017.